Comparison of ocean vertical mixing schemes in the Max Planck Institute Earth System Model (MPI-ESM1.2)

Oliver Gutjahr[1], Nils Brüggemann[1,2], Helmuth Haak[1], Johann H. Jungclaus[1], Dian A. Putrasahan[1], Katja Lohmann[1], and Jin-Song von Storch[1,3]

[1]Max Planck Institute for Meteorology, Hamburg, Germany
[2]University of Hamburg, Hamburg, Germany
[3]Center for Earth System Research and Sustainability (CEN), University of Hamburg, Germany

Correspondence: O. Gutjahr (oliver.gutjahr@mpimet.mpg.de)

Abstract. We compare the effects of four different ocean vertical mixing schemes on the [..[1]]mean state of the ocean and atmosphere in the Max Planck Institute Earth System Model (MPI-ESM1.2)[..[2]]. Besides the default Pacanowski and Philander (1981) (PP) scheme, we use the K-profile parameterisation (KPP) from the Community Vertical Mixing (CVMix) library [..[3]]and have implemented a scheme based on turbulent kinetic energy (TKE) and a recently developed prognostic
5 scheme for internal wave energy and its dissipation (IDEMIX) to replace the often assumed constant background diffusivity in the ocean interior. We analyse in particular the effects of IDEMIX on the ocean mean state, when combined with TKE (TKE+IDEMIX).

[..[4]]

[..[5]]We find warmer sea surface temperatures (SSTs) in the North Atlantic and Nordic Seas using KPP or TKE(+IDEMIX),
10 which is related to 10 % higher overflows that cause a stronger and deeper upper cell of the Atlantic meridional overturning circulation (AMOC) and thereby an enhanced northward heat transport and higher inflow of warm and saline water from the Indian Ocean into the South Atlantic. A saltier subpolar North Atlantic and Nordic Seas leads to increased deep convection and thus to the increased overflows. Due to the warmer SSTs, the extratropics of the northern hemisphere become warmer with TKE(+IDEMIX), weakening the meridional gradient and thus the jet stream. With KPP, the tropics
15 and the southern hemisphere also become warmer without weakening the jet stream. Using an energetically more consistent scheme (TKE+IDEMIX) produces a more heterogeneous and realistic pattern of vertical [..[6]]eddy diffusivity, with

---

[1]removed: ocean mean state simulated by

[2]removed: in the framework of

[3]removed: . Besides the PP and KPP scheme, we implemented the TKE scheme

[4]removed: In general, we find little sensitivity of the ocean surface , but considerable effects for the interior ocean. Overall, we cannot classify any scheme as superior to the others, as these schemes modify biases that vary with region or variable but produce a similar global-scale bias pattern.

[5]removed: However, using a more realistic and energetically

[6]removed: diffusion

lower [..[7]]diffusivities in deep and flat-bottom basins and elevated turbulence over rough topography. [..[8]]IDEMIX improves in particular the diffusivity in the Arctic Ocean and reduces the warm bias [..[9]]in the Atlantic water [..[10]] layer. We conclude that although shortcomings due to model resolution determine the global-scale bias pattern, the choice

20   of the vertical mixing scheme may play an important role for regional biases.

Copyright statement. TEXT

1 Introduction

Vertical mixing in the ocean is a complex phenomena and its magnitude depends on processes acting over a large range of vertical and horizontal scales, from about 1 km to several meters down to centimetres (Fox-Kemper et al., 2019). Vertical

25   mixing affects key elements in the ocean that are of climatic importance, such as ocean stratification, the distribution of temperature, salinity [..[11]]and passive tracers, the ocean uptake of heat and carbon, and the global meridional overturning circulation (MOC; e.g. Gent, 2018).

In ocean models, the processes that lead to mixing are subgrid-scale and therefore not resolved, so they have to be parameterised. [..[12]]The complexity of these parameterisations [..[13]]varies in dependence of our understanding, application,

30   and available resources (e.g. Large et al., 1994; Fox-Kemper et al., 2019). In fact, the parameterisation of vertical mixing constitutes one of the current shortcomings of ocean models (Robertson and Dong, 2019; Fox-Kemper et al., 2019).

[..[14]]We compare four ocean vertical mixing schemes in coupled simulations with [..[15]]the Max Planck Institute Earth System Model (MPI-ESM1.2). Such a comparison provides a better understanding of the model behaviour at the process level, especially when the same model is used. It is therefore very helpful to have libraries that provide different choices for

35   parameterisations, such as the Community Vertical Mixing (CVMix) library (Griffies et al., 2015; Van Roekel et al., 2018)[..[16]]. We have coupled CVMix to MPI-ESM1.2 and [..[17]]used its infrastructure to extend the library by the turbulent kinetic energy (TKE) scheme (Gaspar et al., 1990) and a prognostic scheme for internal wave energy in the ocean, called Internal Wave Dissipation, Energy and Mixing (IDEMIX; Olbers and Eden, 2013), which are not yet an official part of CVMix (see section 2 and appendix A3).

---

[7]removed: diffusivity

[8]removed: In addition, TKE+IDEMIX improves the circulation in the Nordic Seas and Fram Strait, thus reducing

[9]removed: of

[10]removed: (AW) layerin the Arctic Ocean to a similar extent as has been demonstrated with eddy-resolving ocean models.

[11]removed: , and other

[12]removed: Depending on our understanding, the

[13]removed: for turbulent and convective mixing varies

[14]removed: Here, we aim to compare four different

[15]removed: MPI-ESM1.2

[16]removed: , which we have coupled

[17]removed: extended by two additional schemes

40   Frequently used ocean vertical mixing schemes date back to the 1980s and 1990s. Often a modelling centre or a group decides to implement only one of these schemes and, for practical reasons such as tuning effort, not to deviate from it afterwards. However, as these schemes are based on different principles, deviations in the results are to be expected. We further note that even the same scheme may produce different results due to the numerical implementation (e.g. Li et al., 2019) and small modifications (e.g. Danabasoglu et al., 2006).

45   In the ocean surface boundary layer, schemes [..[18]]diagnose vertical profiles of scalar mixing diffusivity and viscosity from surface forcing and background fields, such as in the PP scheme (Pacanowski and Philander, 1981) or in the K-profile parameterisation (KPP; Large et al., 1994)[..[19]]. Second order schemes (Mellor and Yamada, 1982), such as [..[20]]the TKE scheme (Gaspar et al., 1990), contain in addition to the mean quantities also prediction equations for higher order moments, i.e. for variance and covariance terms of heat and momentum. These two most [..[21]]common approaches represent processes that

50   result in vertical shear of the velocity and in changes of the buoyancy, e.g. due to convection. These schemes can become more complex by adding [..[22]]further sub-grid scale processes (Fox-Kemper et al., 2019), such as mixing by Langmuir turbulence (e.g. McWilliams et al., 1997; Li and Fox-Kemper, 2017; Li et al., 2019) or internal tides (Garrett, 2003).

      [..[23]]

      [..[24]]

55   [..[25]]

      [..[26]]

---

[18]removed: provide either direct

[19]removed: , or fluxes and covariances in the case of second-order

[20]removed: in the turbulent kinetic energy (TKE) scheme (Gaspar et al., 1990)

[21]removed: commonly used

[22]removed: important

[23]removed: The default scheme in MPI-ESM1.2 is a modified version of the formulation of Pacanowski and Philander (1981) (PP). However, recent experiments with ECHAM6.3 at T255 resolution for the atmosphere, resulted in unstable AMOC states and in a freezing of the Labrador Sea (Putrasahan et al., 2019). Replacing the PP scheme with the K-profile parameterisation (KPP; Large et al., 1994) resolved this issue, maintaining a stable AMOC (Gutjahr et al., 2019). We perform additional sensitivity experiments in which we replace the PP scheme by a scheme based on turbulent kinetic energy (Gaspar et al., 1990), to which we refer as the TKE scheme with two alternatives for the background diffusivity. See an overview of the used vertical mixing schemes in appendix A.

[24]removed: The background diffusivity, which quantifies the mixing due to internal wave breaking, is either parameterised as a constant value (PP, KPP) or it depends on the buoyancy frequency and an artificial minimum value for the turbulent kinetic energy (TKE scheme). In the second case, we combine the TKE scheme with IDEMIX (Internal Wave Dissipation, Energy and Mixing), which describes the energy transfer from internal wave sources to wave sinks using the radiative transfer equation of weakly interacting internal waves (Olbers and Eden, 2013; Eden et al., 2014). Energy that is dissipated by internal waves is treated as an energy source of turbulent kinetic energy, leading to an energetically more consistent solution (Eden et al., 2014).

[25]removed: Furthermore, IDEMIX solves the propagation of low-mode waves away from their generation site (Fox-Kemper et al., 2019) (see appendix section A3 and Fig. A1), along with the energy loss the waves experience as they encounter different ocean regions and continental shelves. Compared to empirical tidal mixing schemes, e.g. Simmons et al. (2004), IDEMIX not only represents internal waves generated by barotropic tides interacting with rough topography, but also internal waves excited at the base of the mixed layer due to high-frequency wind fluctuations.

[26]removed: IDEMIX has been developed recently and its performance was studied in both stand-alone ocean models(Eden et al., 2014; Pollmann et al., 2017; Nielsen et al., 2018) and coupled simulations (Nielsen et al., 2018, 2019). Based on ocean-only simulations, the TKE dissipation calculated with a combined TKE and IDEMIX scheme agrees well with Argo float-derived dissipation rates (Pollmann et al., 2017). Using IDEMIX in coupled simulations

[..][27]]Although KPP is probably the most widely used scheme in ocean models, TKE is also a frequent choice and is part of state-of-the-art ocean models, and for which also extensions such as Langmuir turbulence (Axell, 2002) or surface waves (Breivik et al., 2015) were developed.

60   The remainder of the manuscript is organized as follows. [..][28]]We first give a brief overview of the model configuration in section 2[..][29]], with more details about the vertical mixing schemes and the experiments we conducted. In section 3, we present the results of the comparison for the global ocean and in section [..][30]]4 for the regional ocean. Section 5 presents effects of the mixing scheme in the atmosphere. Finally, we conclude in section 6.

2 Model [..][31]]configuration

65   For our analysis we used the Max Planck Institute Earth System Model in version 1.2.01 (MPI-ESM1.2; Mauritsen et al., 2019) that was also used for the Coupled Model Intercomparison Project Phase 6 (CMIP6). The model consists of the atmospheric submodel ECHAM6.3 (Stevens et al., 2013), including the land-surface submodel JSBACH3.2, and of the ice-ocean submodel MPIOM1.6.3 (Jungclaus et al., 2013; Notz et al., 2013). The submodels are coupled via the Ocean-Atmosphere-Sea-Ice coupler version 3 (OASIS3-mct; Valcke, 2013) with a coupling frequency of 1 h.

70   The horizontal resolution of the atmosphere is T127 (about $103\,\mathrm{km}$) with 95 vertical levels. The ocean is discretised on a tripolar grid with a horizontal resolution of $0.4°$ (TP04; about $44\,\mathrm{km}$) and 40 vertical levels, of which the first 20 levels are distributed in the top $750\,\mathrm{m}$. A partial grid cell formulation (Adcroft et al., 1997; Wolff et al., 1997) was used to better represent the bottom topography. River runoff [..][32]]ist calculated by a horizontal discharge model (Hagemann and Gates, 2003). Tracer advection by unresolved mesoscale eddies is parameterised following Gent et al. (1995) (GM) with a constant eddy thickness

75   diffusivity of $250\,\mathrm{m^2\,s^{-1}}$ for a $400\,\mathrm{km}$ wide grid cell, which reduces linearly with increasing resolution (about $25\,\mathrm{m^2\,s^{-1}}$ for a resolution of $40\,\mathrm{km}$). The lateral eddy diffusivity is parameterised by an isopycnal formulation (Redi, 1982) with a constant value of $1000\,\mathrm{m^2\,s^{-1}}$ for a $400\,\mathrm{km}$ wide grid cell, which again reduces linearly with increasing resolution (about $100\,\mathrm{m^2\,s^{-1}}$ for a resolution of $40\,\mathrm{km}$).

The default parameterisation of ocean vertical mixing is a modified version [..][33]]PP scheme that was extended with a

80   wind-induced mixing term (Marsland et al., 2003)[..][34]]. This model configuration is referred to as "high resolution" (HR) and was described and tested in more detail by Mauritsen et al. (2019), Müller et al. (2018), and Gutjahr et al. (2019).

by Nielsen et al. (2018) revealed only a minor effect on the climate state. However, they demonstrate reduced thermocline diffusivities with IDEMIX, which leads to a sharper and shallower thermocline, because less heat is mixed downwards.

[27]removed: Despite the latter but because of the promising results with respect to observations from Pollmann et al. (2017) and the results from Eden et al. (2014), we compare the effect of IDEMIX with the other mixing schemes of MPI-ESM1.2 and analyse regions that are most sensitive to IDEMIX on the typical time scale of 100 years for climate simulations

[28]removed: In

[29]removed: we briefly describe the model and experiments,

[30]removed: 3 and 4 , and

[31]removed: description

[32]removed: was

[33]removed: of the Pacanowski and Philander (1981) or PP scheme ,

[34]removed: (see Appendix A for details). The PP scheme was also used to tune MPI-ESM1.2-HR (Mauritsen et al., 2012)

To analyse the effect of different ocean vertical mixing schemes on the [..[35]]mean state, we coupled the [..[36]]CVMix library (Griffies et al., 2015; Van Roekel et al., 2018) to MPI-ESM1.2. [..[37]]KPP, as described in [..[38]]Large et al. (1994), is already included in CVMix and has been used with MPI-ESM1.2 by Gutjahr et al. (2019). In addition, we have added the [..[39]]TKE scheme (Gaspar et al., 1990; Eden et al., 2014) and IDEMIX (Olbers and Eden, 2013) to CVMix, which is however not yet officially available. Although it is principally possible to couple IDEMIX to other mixing schemes, such as KPP, we only combined it with TKE [..[40]]because TKE and IDEMIX both rely on energy budgets, which results in a more consistent mixing scheme. In the following, we describe the ocean vertical mixing schemes in more detail. A complete description is given in appendix A.

2.1 Ocean vertical mixing schemes in MPI-ESM1.2

The default vertical mixing scheme in MPI-ESM1.2 is a modified version of the PP scheme that was extended with an additional wind-induced mixing term (Marsland et al., 2003). The modified PP scheme was used to tune MPI-ESM1.2 (Mauritsen et al., 2012), which is why we did not use the version that comes with CVMix. Recent experiments with a higher-resolution (T255 or ∼50 km) version of ECHAM6.3, the atmospheric model developed at MPI-M, resulted in a collapse of the Atlantic meridional overturning circulation (AMOC) and icing of the Labrador Sea (Putrasahan et al., 2019). By replacing PP with KPP, however, Gutjahr et al. (2019) showed that a stable AMOC is maintained. Complementing to the MPI-ESM1.2-HR simulations performed by Gutjahr et al. (2019) with PP and KPP, we perform two additional sensitivity experiments in which we replace the PP scheme by TKE (Gaspar et al., 1990), which has two alternatives for parameterising the background diffusivity.

The background diffusivity, which quantifies the mixing due to internal wave breaking, is either parameterised as a constant value (PP or KPP), or it depends on the buoyancy frequency and an artificial minimum value for the TKE scheme. We have implemented the TKE scheme with two alternatives for the background diffusivity. In the first case, we use a minimum value for TKE that is modified by the buoyancy frequency to represent the breaking of internal waves. In the second case, we do not assume an artificial minimum value for TKE, but combine the TKE scheme with IDEMIX, which describes the energy transfer from internal wave sources to wave sinks prognostically via a radiative transfer equation of weakly interacting internal waves (Olbers and Eden, 2013). Energy dissipated by internal waves (wave breaking) is treated as an energy source for TKE, resulting in a more energetically consistent solution. (Eden et al., 2014).

Furthermore, IDEMIX solves the propagation of low-mode waves away from their generation site (Fox-Kemper et al., 2019), in the vertical and horizontal (see appendix section A3 and Fig. A1), along with the energy loss the waves experience as they encounter different ocean regions and continental shelves. As the internal waves propagate, wave-wave

---

[35]removed: ocean

[36]removed: Community Vertical Mixing (CVMix)

[37]removed: The K-profile parameterisation (KPP)

[38]removed: (Large et al., 1994)

[39]removed: (TKE; Gaspar et al., 1990; Eden et al., 2014)

[40]removed: , because both schemes

interaction is accounted for that might dampen the waves (Olbers and Eden, 2013). Compared to empirical tidal mixing schemes, e.g. Simmons et al. (2004), IDEMIX represents not only internal waves generated by barotropic tides that interact with rough submarine topography, but also internal waves excited at the base of the mixed layer due to high-frequency wind fluctuations. Furthermore, in contrast to the tidal mixing scheme of Simmons et al. (2004), internal wave energy also propagates horizontally and might thus affect mixing at considerable distance from its generation site.

IDEMIX has been developed recently and its performance was studied in both stand-alone ocean models (Eden et al., 2014; Pollmann et al., 2017; Nielsen et al., 2018) and coupled simulations (Nielsen et al., 2018, 2019). Based on ocean-only simulations, the TKE dissipation calculated with a combined TKE and IDEMIX scheme agrees well with Argo float-derived dissipation rates (Pollmann et al., 2017). Using IDEMIX in coupled simulations, Nielsen et al. (2018) report only a minor effect on the sea surface temperature. However, they demonstrate reduced thermocline diffusivities with IDEMIX, which leads to a sharper and shallower thermocline, because less heat is mixed downwards. Although IDEMIX produces colder temperature within the first 1000 m of their simulations, at mid-depth the temperatures are in better agreement with observations.

Due to these promising results, we compare the effect of IDEMIX with the other mixing schemes of MPI-ESM1.2 and analyse regions that are most sensitive to IDEMIX on the typical time scale of 100 years for climate simulations.

2.2 Experiments

We performed four 100-year long [..[41]]simulations with MPI-ESM1.2-HR using four different ocean vertical mixing schemes. See Tab. 1 for an overview of the experiments and Appendix A for details of the mixing schemes.

The reference simulation (HR$_{pp}$) uses the PP scheme and exactly the configuration used by Müller et al. (2018) and Gutjahr et al. (2019). In the second simulation we used the KPP scheme and refer to it as HR$_{kpp}$. The configuration of this experiment is exactly as in Gutjahr et al. (2019). These two simulations were also compared with higher resolution versions (atmosphere and ocean) by Gutjahr et al. (2019), as part of the High-Resolution Model Intercomparison Project (HighResMIP; Haarsma et al., 2016).

The third experiment (HR$_{tke}$) used the TKE scheme with a background diffusivity [..[42]]that depends on the buoyancy frequency and on a minimum value for [..[43]]TKE (see Appendix A3), but without any contribution from IDEMIX. In the last experiment (HR$_{ide}$), we used the TKE scheme together with IDEMIX (TKE+IDEMIX) and replaced the artificial background diffusivity with one diagnosed from [..[44]]TKE that is fueled by the internal wave dissipation (see section A3 for more details). If not explicitly mentioned, we used default values for the parameters of the mixing schemes, as listed in the respective original description (see also Appendix A), without analysing the effect of changed parameters.

The initial state was derived from a MPI-ESM1.2-HR simulation (with the PP scheme) that was nudged to the averaged temperature and salinity state of 1950 to 1954 of the Met Office Hadley Centre EN4 observational data set (version 4.2.0;

---

[41]removed: control

[42]removed: depending

[43]removed: turbulent kinetic energy

[44]removed: turbulent kinetic energy

Good et al. (2013)), as described in Gutjahr et al. (2019). All simulations were forced by constant 1950s conditions according to the HighResMIP protocol (Haarsma et al., 2016). As recommended in [..[45]]this protocol, the model was not [..[46]]retuned to obtain isolated effects from changing the ocean vertical mixing scheme. If not stated otherwise, we analysed averages over the last 20 model years (model years 81 to 100). [..[47]]Although our focus is on the ocean, we briefly present results for the atmosphere as well.

3 [..[48]]Effects on the global ocean

In the following, we present how the choice of the ocean vertical mixing scheme affects the ocean mean state in control simulations with MPI-ESM1.2-HR. We first present results for the global ocean, before discussing specific regional aspects [..[49]]in section 4[..[50]].

3.1 Spatial distribution of [..[51]]vertical diffusivity

[..[52]]Away from boundary currents, deep convection areas and the surface mixed layer, the vertical diffusivity K is [..[53]]approximately homogeneously distributed to leading order in the simulations with PP and KPP, which both use the simple constant background diffusivity of $K = 1.05 \cdot 10^{-5}\,\mathrm{m^2\,s^{-2}}$ for parameterising internal wave breaking, as demonstrated exemplary for a model layer at intermediate depth of 1020 m (Fig. 1)[..[54]]. Because of the relationship $K = \sqrt{2}E_{\mathrm{min}}/N$ for the background diffusivity in the TKE scheme (see Appendix A3), HR$_{\mathrm{tke}}$ simulates a small K in the tropical and subtropical ocean, where N is [..[55]]positive and a large K in the high-latitude ocean, where N is [..[56]]negative. Even more heterogeneous is the distribution of K in HR$_{\mathrm{ide}}$, which simulates stronger mixing above rough topography and mixing coefficients of about two orders of magnitude lower above the abyssal plains and in the Arctic Ocean. [..[57]]Hotspots of strong vertical mixing are simulated for all four cases particularly in the subpolar North Atlantic (SPNA), in the Nordic Seas, and in the Weddell and Ross Sea of the Southern Ocean. Excessive deep convection in the Weddell Sea is a known issue in ocean models (e.g. Sallée et al., 2013; Kjellsson et al., 2015; Heuzé et al., 2015; Naughten et al., 2018) and not unique to MPI-ESM1.2-HR. The unrealistic

---

[45]removed: that

[46]removed: re-tuned to obtain unbiased effects from the change of

[47]removed: Furthermore, we restrict the comparisons to the oceanmean state, being aware that there possibly are different responses and feedbacks with the atmosphere

[48]removed: Global comparison

[49]removed: (

[50]removed:)

[51]removed: the

[52]removed: For large parts of the ocean

[53]removed: homogeneously distributed in the first order

[54]removed: ; taking on the background value $K = 1.05 \cdot 10^{-5}\,\mathrm{m^2\,s^{-2}}$ in the case of HR$_{\mathrm{pp}}$ and HR$_{\mathrm{kpp}}$

[55]removed: large

[56]removed: small

[57]removed: Hot spots

convection is related to anomalously frequent open-ocean Weddell Sea polynyas (Gordon, 1978; Carsey, 1980; Gordon, 2014). HR$_{ide}$ [..[58]]reduces the occurrence of this spurious deep convection, which we will discuss in section 4.4.

165   A closer look at Fig. 1 reveals more regional differences in the above-mentioned areas[..[59]]. We will [..[60]]relate them to biases in temperature and salinity [..[61]](section 3.2 and 3.4) and discuss them in more detail for the [..[62]]SPNA and Nordic Seas (section 4.1), the Fram Strait (section 4.2), [..[63]]the Arctic Ocean (section [..[64]]4.3), and the Southern Ocean (section 4.4).

3.2   Sea surface temperature and salinity bias

170   The sea surface temperature (SST) is a key quantity for the atmosphere-ocean coupling. [..[65]]Reducing biases of SST in model simulations is thus of crucial importance. However, the causes of [..[66]]SST biases are often complex [..[67]]and result, among others, from insufficient horizontal and vertical resolution and from the need to parameterise subgrid-scale processes[..[68]], which has the largest influence on the biases (Fox-Kemper et al., 2019)[..[69]]. Vertical mixing is thereby only one of these parameterisations.

175   Overall, the [..[70]]SSTs are mostly colder in [..[71]]the MPI-ESM1.2-HR simulations compared with EN4 (Fig. 2)[..[72]]. Although vertical mixing has [..[73]]little effect on the SST bias in large parts of the ocean, some areas [..[74]]are more sensitive. One such area is the North Atlantic with its subpolar gyre, as well as the Nordic Seas. The largest cold bias occurs in the North Atlantic and amounts to -7°C in HR$_{pp}$. This cold bias is a common phenomena in ocean models (e.g. Randall et al., 2007) and is mainly caused by a too zonal pathway of the Gulf Stream (Dengg et al., 1996) in relation to insufficient horizontal resolution

180   and northward heat transport (Wang et al., 2014). [..[75]]By using a vertical mixing scheme [..[76]]other than PP, we find that the SST cold bias in the North Atlantic is reduced (Fig. 2b-d). [..[77]]This reduction of the cold bias can be explained by

---

[58]removed: reduce

[59]removed: , which we will discuss in the following

[60]removed: further relate these differences to the

[61]removed: bias

[62]removed: Arctic Ocean

[63]removed: SPNA and Nordic Seas

[64]removed: 4.1

[65]removed: However, ocean-only and coupled climate models generate biases

[66]removed: which

[67]removed: . Among others, the resolution , discretisation, and parameterisation of

[68]removed: have the largest effect

[69]removed: , with vertical mixing being just one complex process

[70]removed: SST is

[71]removed: our

[72]removed: , with some exceptions such as in upwelling regions, in the North Atlantic subpolar gyre, and along the Labrador Current

[73]removed: minor influence on

[74]removed: react more sensitively

[75]removed: The North Atlantic SST is sensitive to the exchange of the

[76]removed: in that the cold bias is attenuated

[77]removed: However, this cold bias reduction comes at the expense of an even warmer bias in the subpolar gyre and Nordic Seasthan in HR$_{pp}$. Although the sea ice edge is in better agreement with observations (not shown), it is probably caused by the wrong reason. We will discuss these changes in more detail in section 4.1

a generally warmer North Atlantic. A stronger Atlantic meridional overturning circulation (AMOC) in the simulations with KPP and TKE (see section 3.1.1) transports more heat northwards that leads to warmer temperatures in the SPNA, especially in the Labrador and Irminger Seas, and in the Nordic Seas.

Strong warm biases occur also in the tropical upwelling regions off the west coasts of Africa and South America, which is related to insufficiently resolved coastal winds that force the upwelling of colder water (Milinski et al., 2016).

The sea surface salinity is mostly unaffected by the chosen vertical mixing scheme, except in the Arctic Ocean (Fig. 3). [..[78]]By using the TKE or TKE+IDEMIX [..[79]]scheme, the salinity bias is considerably reduced, especially in the Canada Basin (Fig. 3c-d)[..[80]]. The cause for these fresher surface waters is not yet well understood. Most likely it is linked to reduced sea ice formation that we discuss in the next section.

3.3 Sea ice

The extent and thickness of sea ice in March in the Arctic Ocean and the Nordic Seas is shown in Fig. 4. We compare the sea ice thickness to average thickness (1979–2005) of the Pan-Arctic Ice-Ocean Modeling and Assimilation System (PIOMAS) reanalysis (Zhang and Rothrock, 2003; Schweiger et al., 2011). We define the ice edge as the 15 % ice concentration and compare it with the EUMETSAT OSI SAF (OSI-409-a; v1.2) product (1979–2005) (EUMETSAT Ocean and Sea Ice Satellite Application, 2015).

The ice extent is largest in the reference simulation with the PP scheme (Fig. 4a). The ice edge extends further south everywhere than in PIOMAS, especially in the Nordic Seas and the Labrador Sea. The ice edge in the Labrador Sea and the Nordic Seas lies further north in all simulations with KPP and TKE, especially in HR_{ide}. In the North Pacific, the ice edge is less affected and lies only further north in the Sea of Okhotsk in HR_{ide}. The more northerly location of the ice edge in the KPP and TKE simulations results from warmer water temperatures in the Nordic Seas and Labrador Sea, which causes the sea ice to retreat.

Ice thickness is lower in all simulations than in PIOMAS, especially in the central Arctic and north of Greenland, and lowest in HR_{ide}. What causes thinner ice in the simulations with KPP and TKE is unclear and remains for further investigation. It could be related to lower ice production in the marginal seas, especially in the Laptev Sea, and could require further tuning of the lead-close parameterisation.

In the southern hemisphere there is also thinner ice simulated with the TKE and TKE+IDEMIX scheme for the time-averaged September (Fig. 5), especially along the coast of Antarctica. However, we note a closed sea ice cover in the Weddell Sea in HR_{ide} that reduces spurious convection within the Weddell Sea polynya (see more details in section 4.4.1). The sea ice extent is larger than in OSI SAF, but differs only slightly between the simulations.

---

[78]removed: This bias is considerably reduced by using
[79]removed: , as the surface waters become fresher
[80]removed: , probably due to increased inflow from the McKenzie River

3.4 Ocean interior

3.4.1 Horizontal maps of hydrographic biases

At intermediate depth, all simulations are too warm [..[81]]compared to EN4, as shown [..[82]]by the temperature bias for the model layer at 740 m depth (Fig. [..[83]]6). Exceptions are the Southern Ocean and parts of the North Atlantic, where the ocean

215   is colder at upper to intermediate depth. In the Atlantic Ocean, the warm biases are mainly linked to the representation of the Agulhas Current [..[84]]system and Mediterranean Overflow water (MOW), as well as to the pathway of the Gulf Stream. Previous studies with MPI-ESM1.2 have shown that these warm biases diminish with increasing spatial resolution (Gutjahr et al., 2019; Putrasahan et al., 2019). Advection of these warmer (and more saline) water masses causes subsequent warm biases in the SPNA, Nordic Seas and Arctic Ocean. Even though an eddy-resolving resolution $(0.1°)$ reduces most of these

220   biases, as shown by Gutjahr et al. (2019) with MPI-ESM1.2-ER[..[85]], the choice of the vertical mixing scheme also affects the hydrographic biases, for instance the warm bias is reduced in the Arctic Ocean [..[86]]but enhanced for the MOW [..[87]](Fig. [..[88]]6).

    [..[89]]Salinity shows a similar bias pattern at intermediate depth (Fig. [..[90]]8). The Atlantic is too saline, which is again due to the poor representation of the MOW and the Agulhas Current [..[91]]system. Consequently, northward advection by the Gulf

225   Stream and the boundary currents along the European shelf distribute these saline waters into the [..[92]]SPNA and Nordic Seas, where they affect to local water masses (Reid, 1979; McCartney and Mauritzen, 2001; Lozier and Sindlinger, 2008). At a resolution of $0.4°$, [..[93]]MPI-ESM1.2-HR is unable to capture the Agulhas Retroflection. Although all simulations show a similar salinity bias in the Agulhas region, we note a larger bias for HR_{kpp}, HR_{tke}, and HR_{ide}[..[94]]. This larger bias indicates a stronger inflow of [..[95]]warm and salty water from the Indian Ocean. In fact, the inflow is about 10 Sv stronger with TKE

230   and about 15 Sv with KPP than the 40 to 50 Sv in HR_{pp} (Fig. 7).

    The largest difference in salinity bias is linked to the representation of MOW. Although all models produce warmer and more saline MOW, the bias is decreased only in HR_{tke}. The bias even becomes considerably larger when [..[96]]TKE is used with

---

[81]removed: with respect
[82]removed: in
[83]removed: 4
[84]removed: System
[85]removed: (0.1 °)
[86]removed: and
[87]removed: warm bias
[88]removed: 4
[89]removed: The salinity
[90]removed: 5
[91]removed: System
[92]removed: subpolar North Atlantic
[93]removed: our model
[94]removed: , which
[95]removed: saline
[96]removed: IDEMIX is used in the TKE scheme

IDEMIX instead of an artificial background diffusivity (Fig. [..[97]]8d). [..[98]]Although the use of IDEMIX increases vertical eddy diffusivity at the overflow sill [..[99]]of the Strait of Gibraltar and [..[100]]in the Gulf of Cádiz (not shown), downstream vertical mixing over the abyssal plains of the Atlantic is very low, probably due to the low internal wave activity, so that the diffusivity becomes very low ($O(10^{-6}\,\mathrm{m}^2\,\mathrm{s}^{-2})$). We speculate that this lower diffusivity reduces mixing with the [..[101]]overlying, less saline North Atlantic Central Water, so that the warm, highly saline core of the MOW is less diluted than in the other simulations. However, it remains a subject of further investigation whether warmer and especially saltier MOW with IDEMIX is related to other influencing factors, such as the variability of the near-surface wind field or the net evaporation over the Mediterranean Sea (Aldama-Campino and Döös, 2020).

We further note a slight freshwater bias in the Arctic Ocean in HR_{ide} that we will describe in relation to the Atlantic water layer in section 4.2.

3.4.2 Vertical [..[102]]sections through the Atlantic and Arctic Ocean

A vertical section of the [..[103]]zonally averaged potential temperature bias through the Atlantic and Arctic [..[104]]Oceans (Fig. [..[105]]

[..[106]]9) shows predominantly too cold near-surface water, especially in the North Atlantic, where the cold bias extends to a depth of about $1000\,\mathrm{m}$ [..[107]]

4 [..[108]]

---

[97]removed: 5

[98]removed: Probably, using IDEMIX reduces the vertical mixing in the Mediterranean Sea and especially near

[99]removed: in

[100]removed: downstream thereof. This

[101]removed: ambient less saline water

[102]removed: section

[103]removed: zonal

[104]removed: Ocean

[105]removed: 6) , shows again warm biases related to the above named currents and water masses. Salinity shows a similar bias pattern (not shown) with too saline waters where there is a warm bias.

[106]removed: The simulations show pronounced warm biases in the Atlantic water(AW) layer in the Arctic Ocean, in the Nordic Seas, for the overflow waters at roughly $60\,^{\circ}\mathrm{N}$, for the MOW at $30\,^{\circ}\mathrm{N}$ at about 800 to

[107]removed: depth, and at roughly $40\,^{\circ}\mathrm{S}$ in relation with Agulhas leakage and hence too much inflow from the Indian Ocean. HR_{kpp} shows almost no difference to the reference simulation, except for slightly warmer overflow waters and a slightly warmer Arctic Ocean. A similar result is found for HR_{tke}, except for a lower MOW bias. In contrast, the warm bias of the AW layer in the Arctic Ocean is reduced in HR_{ide}, so that biases north of Svalbard are smallest in HR_{ide}, and the warm bias related to the MOW and Agulhas leakage become stronger.

[108]removed: Regional comparison

[..[109]]due to errors in heat convergence resulting from a misrepresented Gulf Stream and North Atlantic Current. The intermediate water masses are too warm compared with EN4 and there appears almost no bias in the deeper ocean, since the simulation length is too short to affect the abyssal ocean. This general bias pattern establishes in all simulations, but we note some differences.

3.1 [..[110]]

3.0.1 [..[111]]

[..[112]]All simulations simulate a too warm ([..[113]]

[..[114]]and [..[115]][..[116]][..[117]][..[118]]

[..[119]][..[120]][..[121]]

[..[122]]saline) inflow of from the Indian Ocean to [..[123]]

---

[109]removed: In the next sections we will discuss in more detail some of the above mentioned areas where IDEMIX influences the model bias both positively and negatively. We already note here that the insufficient model resolution determines the large-scale bias pattern, as shown by Gutjahr et al. (2019). However, the choice of the vertical mixing scheme plays an important role on the regional scale. In particular the Arctic Ocean, the subpolar North Atlantic and the Southern Ocean are sensitive to the chosen mixing scheme.

[110]removed: Atlantic water layer in the Arctic Ocean and the circulation at Fram Strait

[111]removed: Fram Strait

[112]removed: A well-known error of many state-of-the-art ocean models is an anomalously thick and deep AW layer (e.g. Holloway et al., 2007; Shu et al., 2019). This error is thought to be related to model resolution and to vertical mixing schemes, in particular to the choice of the fixed background mixing value (Zhang and Steele, 2007; Liang and Losch, 2018). In terms of model resolution, it was recently shown that a high-resolution ocean

[113]removed: $1/10°$ or better) reduces this bias (Wang et al., 2018; Gutjahr et al., 2019). Here, however, we demonstrate that the bias is also reduced by using an improved vertical mixing scheme (i.e. TKE+IDEMIX), which produces a stronger southward recirculation at Fram Strait and stronger heat loss due to enhanced mixing.

[114]removed: Warm and saline AW is the main contributor of salt and oceanic heat into the Arctic Ocean. The AW flows northward first as the Norwegian Current in the Nordic Seas until it splits into two branches south of Svalbard (Fig. 7). A small branch enters the Barents Sea via the Barents Sea Opening (Barents Sea Water Branch) and flows into the Arctic Ocean at the St. Anna Trough in the northern Kara Sea. The main branch continues northward as the West Spitsbergen Current (WSC). About half of the AW transported in the WSC recirculates between 76

[115]removed: 81°N, thereby becoming part of the southward flowing East Greenland Current (EGC). Observations suggest the strongest recirculation at about 79°N

[116]removed: 'southern' recirculation;

[117]removed: (Marnela et al., 2013)

[118]removed: .

[119]removed: A 'northern' recirculation was observed from moorings at about 81°N in association with the cyclonic gyre around the Molloy Hole (

[120]removed: N;

[121]removed: E) and mesoscale eddies (Marnela et al., 2013; Hattermann et al., 2016). Because of the small local Rossby radius of about 3 to 6 km in the WSC (von Appen et al., 2016) and about 6 km in the EGC (Zhao et al., 2014), most ocean models do not resolve eddies and thus simulate no 'northern' recirculation but a recirculation that is too far south compared to observations (Fieg et al., 2010). However, several studies with eddy-permitting/resolving ocean models (e.g. Wang et al., 2018; Fieg et al., 2010; Kawasaki and Hasumi, 2016) showed a 'northern' recirculation and eddy-activity in the Fram Strait.

[122]removed: The other, non-recirculating half of the AW flows through Fram Strait into the Arctic Ocean (Fram Strait Branch Water), supplying the AW layer at 200

[123]removed: 700 m (Rudels et al., 1994), with its core at a depth at about 400 m.

[..[124]]

260   [..[125]]the [..[126]]South Atlantic, roughly at $30\,^\circ$S. The model resolution is too coarse to correctly capture the Agulhas Current system; in particular, the retroflection and Agulhas rings are not well represented. Instead, warm and saline water flows more or less constantly from the Indian Ocean into the South Atlantic. From all simulations, this misrepresentation is strongest in HR_{ide}. The reason for this behaviour remains a subject for future studies.

[..[127]]A second source of too warm water is related to the MOW, as described above. The core of the MOW reaches a
265   neutral buoyancy surface slightly above 1000 [..[128]]

[..[129]]m depth at roughly $30\,^\circ$N. The MOW is warmest in $HR_{[..^{130}]ide}$ [..[131]]but colder in HR_{tke} compared to the reference simulation.

These already too warm waters are transported north throughout the whole Atlantic and eventually reach the SPNA and Nordic Seas. Part of it continuous further into the Arctic [..[132]]

---

[124]removed: The first indication why the AW layer warm bias in HR_{ide} is smaller (Fig. 8) relates to a stronger recirculation in the Fram Strait, which splits only in HR_{ide} into a 'southern' (south of $79\,^\circ$N) and a 'northern' recirculation (north of $79\,^\circ$N) . A stronger recirculation means less inflow of AW and thus less heat transport into the Arctic Ocean . This stronger return circulation seems to be related to enhanced deep convection in the Nordic Seas (Fig. 11), which in turn accelerates the geostrophic flow around the convection centre due to steeper isopycnal gradients. In fact, the Greenland Sea gyre is up to 5 Sv stronger in HR_{ide} (Fig. 12d). Furthermore, the 'northern' recirculation transfers volume and heat from the WSC to the EGC, which thus does not enter the Arctic Ocean. A similar circulation structure develops in the eddy-resolving MPI-ESM1.2-ER model (Gutjahr et al., 2019, not shown), but with sharper defined currents. In general, eddy-resolving models were found to improve the water mass properties and the separation of the WSC into a recirculating branch (e.g. Hattermann et al., 2016; Wekerle et al., 2017). Note, however, that the HR model does not resolve eddies in the Fram Strait due to the small Rossby radius at this high latitude.

[125]removed: The final passage of the WSC into the Arctic Ocean is at the Yermak Plateau (YP), a bathymetric feature north of Svalbard known as a hot spot for internal wave activity and mixing (e.g. Fer et al., 2010; Crews et al., 2019). Here the diverging isobaths split the WSC into three branches: 1) the Svalbard branch that flows along the upper inward continental slope of Svalbard (above 500 m depth) 2) the Yermak branch (Crews et al., 2019), which is

[126]removed: lower boundary current along the margin of the YP, roughly along the 1000 m-isobath, and 3) the recirculating branch between 78 and $80\,^\circ$N (Marnela et al., 2013) that flows southward as part of the EGC. However, recent studies indicate a third pathway of the WSC, the Yermak Pass Branch, by which a significant portion of the AW traverses the YP along the 700 m isobath and enters the Arctic Ocean (Koenig et al., 2017).

[127]removed: At the surface, the WSC looses heat directly to the relatively cold atmosphere, while at depth the heat loss is due to turbulent mixing induced by currents and internal waves, and to eddy activity (Fer et al., 2010). Based on measurements, the cooling strength depends on whether the WSC flows around or over the YP, resulting in different mixing rates (Fer et al., 2010). Downstream the YP, the Svalbard and Yermak branches flow along the shelf break to the east, where they encounter the Barents Sea Water Branch at the outlet of the St. Anna Trough (Dmitrenko et al., 2015). The St. Anna Trough is about 300 to 500 m deep in its southern part, reaching

[128]removed: m at the entrance to the Arctic Ocean (Lien and Trofimov, 2013). Both water masses continue thereafter as part of the cyclonic Arctic Circumpolar Boundary Current (Rudels et al., 1999; Aksenov et al., 2011), although most of Fram Strait branch seems to recirculate already in the Nansen Basin (Rudels et al., 2015).

[129]removed: In HR

[131]removed: , HR_{kpp}, and HR_{tke} the warm bias of the AW layer is about $+2$ to $+3\,^\circ$C at YP and approximately $+1$ to $+2\,^\circ$C further downstream along the shelf break of the Eurasian Basin (Fig. 8). Some of the AW also crosses the Lomonosov Ridge and spreads into the Markarov and Canada basins. In HR_{ide} the AW is still too warm at the YP, but not further downstream

[132]removed: .

270 [..[133]]Ocean at a depth of 500 m to more than 1000 m[..[134]], where it becomes the Atlantic water (AW) layer, which is roughly $1\,^\circ$C warmer than in EN4. Due to stronger recirculation in Fram Strait (see section 4.2), less AW enters the Arctic Ocean in HR_{ide}, [..[135]]reducing the warm bias.

 [..[136]]

3.0.1 [..[137]]

275 [..[138]]

 [..[139]]

 [..[140]]The Nordic Seas, but also the Labrador Sea, is thus already to warm when overflow water is generated, leading to too warm overflows across the Greenland-Scotland Ridge at and south of $60\,^\circ$N, reaching depths of about 3000 m. Warmer temperatures in the Nordic Seas compensate at least partly for the increased salinity, so that the increase in

280 density is less. Since the Nordic Seas are warmest in HR[..[141]]$_{kpp}$, the overflows are also warmest in this simulation.

---

[133]removed: A comparison of K at 450

[134]removed: depth at the Fram Strait and in the Arctic Ocean (Fig. 9) reveals two important differences in HR_{ide}. First, the mixing near YP is slightly stronger in HR_{ide} (Fig. 9d) . This increased mixing at YP causes a stronger heat release into the atmosphere, which cools the AW more effectively than in the other simulations. In fact, the sensible heat flux is about 20 to $40\,\mathrm{W\,m^{-2}}$ larger in HR_{ide} than in HR_{pp} (not shown). For comparison, the sensible heat flux is only about 10 to $20\,\mathrm{W\,m^{-2}}$ stronger in HR_{kpp} and HR_{tke}. However, the heat loss, especially the sensible heat flux, is already stronger in the Greenland Sea, further densifying the water for deep convection, and the temperature of the AW is already about $1\,^\circ$C colder at the Fram Strait in HR_{ide}. This stronger heat loss explains why the temperature of the AW at the Fram Strait is less

[135]removed: even though the Greenland Sea Gyre is stronger and thus warmer AW could be expected (Chatterjee et al., 2018; Muilwijk et al., 2019)

[136]removed: Along the shelf-break of the Nansen Basin, all simulations show a sharp band of high mixing coefficients aligned to bathymetry, where polar and shelf waters entrain into the cyclonically spreading AW. A local maximum of vertical mixing is further simulated at the outlet of the St. Anna Trough in the northern Kara Sea, where the Barents SeaWater Branch spills into the Nansen Basin and encounters the Fram Strait Branch Water.

[137]removed: Arctic Ocean

[138]removed: Turbulence in the quiescent interior Arctic Ocean is close to the limits of measurement (Rainville and Winsor, 2008), which are very rare and therefore mixing rates are largely unknown (Fer, 2009). The Arctic Ocean is isolated from the atmosphere by sea ice, such that wind stress is a minor source for mixing in all simulations. In the models, the wind stress thus reduces quadratically with the sea ice concentration (see Appendix A). In addition, brine rejection is less effective as a mixing mechanism because of the strong vertical salinity gradients in the cold halocline layer. Therefore, apart from enhanced mixing by episodic shear events, storms during ice-free conditions (Rainville and Woodgate, 2009), mesoscale eddies, or lateral intrusion along the boundaries, vertical diffusive mixing dominates over turbulent mixing (Fer, 2009).

[139]removed: Internal wave activity is almost absent, except above rough topographic features. In fact, internal waves are trapped at the place of their origin and do not propagate far into the Arctic Ocean. This trapping occurs because the Arctic Ocean is north of the critical latitude, which is $74.5\,^\circ$N for the M_2 tide, beyond which the Earth's rotation prohibits freely propagating internal waves. As a result, they dissipate at or very close to their source region with properties similar to lee waves (Rippeth et al., 2015, 2017).

[140]removed: For this reason, there is little or no contribution to small-scale turbulence in the inner Arctic Ocean in HR_{ide}, especially in the deep and flat-bottomed Canada basin. The mixing coefficient K is up to two orders of magnitude smaller ($O(10^{-6}$ to $10^{-7}\,\mathrm{m^2\,s^{-1}})$) in

[141]removed: $_{ide}$ compared to the other simulations, where K is mostly at the constant background value ($1.05 \cdot 10^{-5}\,\mathrm{m^2\,s^{-1}}$). Representing this trapping of internal waves is crucial to simulate mixing rates that are more consistent with microstructure measurements, which show low turbulent diffusivity in deep, flat-bottomed basins, but elevated mixing rates above deep topography (Rainville and Winsor, 2008). The low diffusivities in deep basins agree well with observations from the Barneo ice camp drift, where $O(10^{-6}\,\mathrm{m^2\,s^{-1}})$ was measured below the mixed layer in the Amundsen Basin (Fer, 2009). A contrasting example of higher mixing rates in the inner Arctic Ocean is a distinct band of strong mixing along and above the Lomonosov Ridge (Fig. 9d). Here, internal waves dissipate immediately after their formation, elevating turbulence locally, what was also measured directly by Rainville and Winsor (2008)

[..[142]]

[..[143]]Salinity shows a similar bias pattern (not shown) with too saline waters where there is a warm bias.

3.1 [..[144]]AMOC and [..[145]]transports

3.1.1 [..[146]]

285 [..[147]] The SPNA and the Nordic [..[148]]Seas are important regions for the global climate, where the vertical connection between the upper warm and the lower cold branch of the [..[149]]AMOC is established. The northward flowing warm AW is cooled by extensive heat loss to the atmosphere until it becomes dense enough to sink into deeper layers. Together with the dense overflow water from the Nordic Seas, it leaves the SPNA as North Atlantic Deep Water (NADW) with the southward-flowing Deep Western Boundary Current (DWBC).

290 The [..[150]]simulations with KPP and TKE produce a stronger and deeper reaching upper branch of the AMOC of $> 18 \, \text{Sv}$ at $26.5°\text{N}$ (Fig. 10) compared with about $15 \, \text{Sv}$ in HR_{pp}. A stronger upper cell may imply a stronger northward heat transport, whereas a deeper upper cell indicates a stronger southward transport of NADW (see section 4.1.2). To compare the enhanced overturning in the Nordic Seas, the water in the Atlantic has to be replaced by stronger inflow from the Indian Ocean that establishes in the simulations with KPP and TKE.

295 We note, however, that the bottom cell is weaker in all sensitivity simulations, which is probably due to a stronger mixing of NADW with Antarctic Bottom Water (AABW), causing the latter to vanish further south. The simulation length of 100 years is too short to see pronounced effects in the deep ocean, but it could be expected that over longer periods (several centuries) the additional mixing from internal waves might affect the diapycnal diffusion of the upwelling deep water, e.g. in the Pacific.

300 ## 4 Effects on the regional ocean

---

[142]removed: Assuming a constant background diffusivity in the Arctic Ocean thus largely overestimates the vertical mixing in the Arctic Ocean. Although the background diffusivity can be artificially reduced in the Arctic Ocean to mimic this low internal wave activity (e.g. Kim et al., 2015; Sein et al., 2018), the very heterogeneous pattern described above is not captured. Coupling IDEMIX to TKE, however, is able to reproduce the spatial pattern and correct magnitudes. It further provides an energetically consistent solution.

[143]removed: Much lower vertical diffusivity under the sea ice in the Arctic Ocean might further cause denser water to enter the Nordic Seas (Kim et al., 2015), pushing up the isopycnals and producing denser deep water, which then increased the overflow volume above the Greenland-Iceland-Scotland Ridge

[144]removed: Subpolar North Atlantic

[145]removed: the Nordic Seas

[146]removed: Convection and mixed layer depths

[147]removed: The subpolar North Atlantic (SPNA)

[148]removed: Sea

[149]removed: Atlantic meridional overturning circulation (AMOC)

[150]removed: sinking of these dense water masses

In this section, we discuss some regional areas in more detail, in particular the Atlantic Ocean, the Nordic Seas and Fram Strait, the Arctic Ocean, and the Southern Ocean. We already note here that the insufficient model resolution determines the large-scale bias pattern, as shown by Gutjahr et al. (2019).

4.1 Subpolar North Atlantic and the Nordic Seas

4.1.1 Convection and mixed layer depths

The sinking of buoyant Atlantic water is thought to [..[151]]be established by downwelling of dense water along the boundary [..[152]]currents with complex interplay of deep convection and the mesoscale eddy field (e.g. Katsman et al., 2018; Brüggemann and Katsman, 2019; Sayol et al., 2019; Georgiou et al., 2019). The [..[153]]water mass transformation of Atlantic water occurs, however, in areas of deep convection and lateral exchange with the boundary current by eddies. Convection, or vertical instability, is parameterised differently in the vertical mixing schemes in MPI-ESM1.2 (see Appendix A), which is why we expect differences in vertical diffusion and mixed layer depths (MLDs). Eddies are only partially resolved in MPI-ESM1.2-HR, so we do not expect the exchange of deep water with the boundary currents to be realistic.

[..[154]]The largest diffusivities (K) are simulated in the Labrador Sea and the Nordic Seas (Fig. [..[155]]11), with markedly greater values in the simulations with KPP and TKE. In particular, we note [..[156]]increased vertical diffusivities in the Irminger Sea, [..[157]]where open-ocean deep convection [..[158]]occurs and contributes to the formation of Labrador Sea [..[159]]water (e.g. Pickart et al., 2003; Våge et al., 2011).

In [..[160]]the PP scheme, the vertical instability is parameterised by enhancing the diffusivity to $K = 0.1\,\mathrm{m^2\,s^{-1}}$. The convection parameterisation in KPP is more complex[..[161]], where non-local transport terms (see section A2) redistribute the surface fluxes throughout the ocean surface boundary layer. These non-local transport terms depend on the net heat and freshwater fluxes at the ocean surface, on K, and on a dimensionless vertical shape function (Large et al., 1994; Griffies et al., 2015). [..[162]]

In the TKE scheme, the buoyancy term (third term on the r.h.s. of Eq. A15), which usually is an energy transfer from TKE to mean potential energy, acts in this case ($N^2 < 0$) in [..[163]]the opposite direction and enhances TKE. However, besides differences in the parameterisations, remotely changed water mass properties, and hence density changes, also affect

---

[151]removed: result from downwelling

[152]removed: current

[153]removed: SPNA and the Nordic Seas are one of the few places where deep convection of the open ocean occurs

[154]removed: All simulations generate the largest values of

[155]removed: 10). In the sensitivity simulations (Fig. 10b-d)the diffusivity is markedly greater than in the reference simulation

[156]removed: an increased vertical diffusivity

[157]removed: which has been recognized as an area

[158]removed: takes place, contributing

[159]removed: Water

[160]removed: HR$_{\mathrm{pp}}$

[161]removed: in HR$_{\mathrm{kpp}}$

[162]removed: In HR$_{\mathrm{tke}}$ and in HR$_{\mathrm{ide}}$

[163]removed: opposite direction, thus enhancing

325   convection and the MLD in the SPNA. Therefore, it is not straightforward to diagnose what is a cause and what is a consequence for changes in the MLDs.

    The average MLDs in March are shown in Fig. [..[164]]12. A direct comparison with MLDs derived from Argo floats are not optimal, because our simulations are control simulations with 1950s greenhouse gas forcing[..[165]]. Keeping this in mind, we find profound differences to Argo float-derived MLDs and across the simulations. As with vertical diffusivity, all simulations

330   show the deepest mixed layers in the Labrador Sea and a second maximum in the GIN Seas. In general, [..[166]]KPP and TKE tend to simulate deeper mixed layers[..[167]]. In the Labrador Sea, the [..[168]]convection area extends too far north in all simulations due to the lack of mesoscale eddies [..[169]]that would impede convection [..[170]]by restratification of the water column (e.g. Eden and Böning, 2002; Brüggemann and Katsman, 2019; Gutjahr et al., 2019).

    HR_{ide} simulates deeper mixed layers in the [..[171]]centre of the Greenland Sea gyre and particular around Jan Mayen,

335   which might be caused by internal wave activity, especially along the Kolbeinsey and Mohn Ridge and along the Jan Mayen Fracture Zone. [..[172]]

    [..[173]]Due to stronger updoming of the isopycnals in the Labrador, Irminger and Greenland Sea in the simulations with KPP and TKE, the strength of the gyres are stronger than in HR[..[174]]pp [..[175]]

    [..[176]](Fig. 13)[..[177]]. This enhanced updoming is caused by a combination of a more saline SPNA and Nordic Seas,

340   e.g. [..[178]]

---

[164]removed: 11

[165]removed: and we apply a different density threshold

[166]removed: the sensitivity simulations all

[167]removed: in the SPNA compared with HR_{pp}

[168]removed: deep mixed layers extend

[169]removed: , which

[170]removed: and restratify

[171]removed: Greenland Sea, in

[172]removed: The boundary current in the GIN Seas is about $0.5\,°C$ colder in HR_{ide} (not shown) and the anticyclonic Lofoten Basin Eddy (Yu et al., 2017), the area of the strongest heat release, is about $1\,°C$ colder than in HR_{pp}, which constitutes a bias of about $-2\,°C$ compared with EN4. In addition, salinity is roughly about 0.2 psu higher in the GIN Seas in HR_{ide} (also in HR_{tke} and HR_{kpp}). These slightly colder but more saline water masses provide more favourable conditions for deep convection in the GIN Seas.

[173]removed: All three sensitivity simulations further show enhanced flow in the western part of the subpolar gyre, especially in the Labrador Sea (Fig. 12b-d), where they also simulate deeper mixed layers. The flow weakens, however, in the eastern part of the subpolar gyre, most pronounced in HR

[175]removed: .

[176]removed: The sensitivity simulations produce a stronger and deeper reaching upper branch of the AMOC of about $> 18\,Sv$ at $26.5\,°N$

[177]removed: compared with about $> 15\,Sv$ in HR_{pp}. A stronger upper cell may imply a stronger northward heat transport, whereas a deeper upper cell indicates a stronger southward transport of NADW. We note, however, that the bottom cell is weaker in all sensitivity simulations, which is probably due to a stronger vertical mixing with NADW, causing the Antarctic Bottom Water (AABW) to vanish. Possibly, simulation length of 100 years are too short to see pronounced effects in the deep ocean. Over longer simulation periods (several centuries), however, the additional mixing from internal waves might affect the diapycnal diffusion of the upwelling deep water

[178]removed: in the Pacific.

[..[179]]about $+0.2$ [..[180]]psu in the Greenland Sea, and enhanced heat loss in the gyre centres. The steeper isopycnal gradients accelerate the geostrophic flow around the convection centres leading to a roughly 10 Sv stronger boundary current in the Labrador Sea and a Greenland gyre that is about 5 Sv stronger.

4.1.2 Overflows from the Nordic Seas

345 A substantial contribution to the NADW constitutes the Denmark Strait overflow water (DSOW; $\sigma > 1027.8\,\mathrm{kg\,m^{-3}}$), which accounts for about half of the observed overflows from the Nordic Seas (Hansen et al., 2004), being its densest water mass. The other major overflow pathway across the Greenland-Iceland-Scotland Ridge is [..[181]]through the Faroe Shetland Channel (FSC; $\sigma > 1027.75\,\mathrm{kg\,m^{-3}}$) and through the Faroe Bank Channel (FBC; $\sigma > 1027.75\,\mathrm{kg\,m^{-3}}$). [..[182]]
The increased MLDs in the [..[183]]simulations with KPP and TKE due to stronger deep convection in the Nordic Seas
350 [..[184]]suggest higher overflow volumes. We applied Welch's two-sided t-tests with $\alpha = 0.05$ ($n = 20$) to test for significant differences in the simulated overflows. See Tab. A1 for all test results.

First we note that all simulations underestimate the observed DSOW volume transport [..[185]]of about 3.2 to 3.4 Sv [..[186]]by roughly 1 Sv (see Tab. 2). Compared with $\mathrm{HR_{pp}}$, however, we find about 10 to 20 % higher DSOW transports in $\mathrm{HR_{kpp}}$[..[187]], $\mathrm{HR_{ide}}$[..[188]]and especially in $\mathrm{HR_{tke}}$ (all with $p < 0.01$). The transports in the [..[189]]KPP and TKE simulations themselves,
355 however, differ not significantly (p-values of 0.13 to 0.52). The higher amount of DSOW [..[190]]might thus explain at least partly the stronger upper cell of the AMOC, and in particular the AMOC strength around $60\,°\mathrm{N}$.

[..[191]]Although overestimated compared to the observations, the FSC overflows [..[192]]in the simulations are of similar magnitude (3.2 to [..[193]]3,3 Sv), with the exception of $\mathrm{HR_{tke}}$, which produces [..[194]]an approximately 10 % higher ([..[195]]3,5 Sv) overflow transport ($p < 0.01$). The FBC overflows are about 15 to 20 % lower in the models (1.7 to 1.9 Sv) than the
360 observed 2.2 Sv by Hansen et al. (2016). The deviations between the models are of the order of 10 %, with a higher mean transport in $\mathrm{HR_{tke}}$ ($p < 0.01$) and a lower transport in $\mathrm{HR_{ide}}$ ($p < 0.01$).

[179]removed: Although IDEMIX affects the water mass properties and deep convection in the SPNA, there is hardly any difference to $\mathrm{HR_{tke}}$ and $\mathrm{HR_{kpp}}$. This result challenges the relationship described by Kim et al. (2015), who link reduced vertical diffusivity under sea ice in the Arctic Ocean to a doming of the isopycnals in the Nordic Seas, thus leading to higher overflow volumes and a 14

[180]removed: % strongerupper cell of the AMOC

[181]removed: the

[182]removed: The enhanced

[183]removed: Nordic Seas suggests

[184]removed: in $\mathrm{HR_{kpp}}$, $\mathrm{HR_{tke}}$, and $\mathrm{HR_{ide}}$ and hence

[185]removed: (

[186]removed:) by about

[187]removed: ($p < 0.01$)

[188]removed: ($p < 0.01$)

[189]removed: sensitivity

[190]removed: in the sensitivity simulations

[191]removed: Despite being

[192]removed: are of about similar magnitude in the simulations

[193]removed: 3.3 Sv), except for

[194]removed: about

[195]removed: 3.5 Sv

Overall, these results suggest about 10 % higher overflow transports across the Greenland-Iceland-Scotland ridge [..[196]]with KPP and TKE, which contribute to a stronger upper cell of the AMOC.

4.2 Fram Strait and Atlantic water layer

365 Atlantic water (AW) is the main supplier of salt and oceanic heat to the Arctic Ocean. From the Nordic Seas it flows northwards into Fram Strait, where about half of the AW recirculates southwards between $76°$ and $81°$N and becomes part of the East Greenland Current. A smaller fraction continues northward as the West Spitsbergen Current (WSC). Due to the successive cooling in its path, the subsiding AW water flows into the Arctic Ocean at mid-depth with its core at about 400 m depth, sealed off from the atmosphere by overlying cold polar surface water.

370 A common error of many state-of-the-art ocean models is an anomalously thick and deep AW layer (e.g. Holloway et al., 2007; Shu et al., 2019). This error is thought to be related to model resolution and to vertical mixing parameterisations, in particular to the choice of the background diffusivity (Zhang and Steele, 2007; Liang and Losch, 2018). In terms of model resolution, it was recently shown that a high-resolution ocean ($0.1°$ or better) reduces biases of the AW layer (Wang et al., 2018; Gutjahr et al., 2019), because eddies are (partly) resolved that also improve the circulation (Wekerle et al., 2017).

375 MPI-ESM-HR at eddy-permitting resolution produces a too warm AW layer, as shown by Gutjahr et al. (2019). Here, we demonstrate that this warm bias is reduced by using TKE+IDEMIX, which is due to a combination of remote (already colder inflowing AW into Fram Strait) and local effects (stronger southward recirculation at Fram Strait and stronger heat loss due to enhanced mixing).

In HR$_{pp}$, HR$_{kpp}$, and HR$_{tke}$ the warm bias of the AW layer is about $+2°$C at the Yermak Plateau (YP), a bathymetric

380 feature northwest of the Svalbard archipelago known as a hotspot for internal wave activity (see also Fig A2b) and mixing (e.g. Fer et al., 2010; Crews et al., 2019), and less further downstream along the shelf break of the Eurasian Basin (Fig. 14). It seems that a part of the AW also crosses the Lomonosov Ridge, except in HR$_{ide}$, and spreads into the Markarov and Canada basins, which is not realistic. The AW is colder in HR$_{ide}$ and better agrees with EN4 in the Eurasian basin, although the central Arctic Ocean becomes about $0.5°$C too cold.

385 Due to stronger heat loss in the Greenland Sea (not shown) the Atlantic water is already about $1°$C colder in HR$_{ide}$ compared with the other simulations when it reaches Fram Strait, although warmer AW could be expected due to the stronger Greenland Sea gyre (Chatterjee et al., 2018; Muilwijk et al., 2019). This contradiction can be explained by a stronger recirculation of AW in HR$_{ide}$ in Fram Strait, which means that less AW flows in the Arctic Ocean and thus less heat.

390 Beside this remote effect, there are local effects related to enhanced mixing at the YP. A comparison of K of the model layer at 450 m depth (Fig. 15) shows that the mixing near YP in HR$_{ide}$ is slightly stronger (Fig. 15d). Internal waves break near the YP and thus transfer energy to small-scale turbulence. This effect is larger in the prognostic IDEMIX than from the assumed constant background diffusivity. The increased mixing in the ocean causes more heat loss, as more warm AW is exposed to the cold atmosphere, and thus cools more efficiently than in the other simulations. In fact, the sensible

---

[196]removed: in the sensitivity simulations , which contribute to a

395   heat flux is about 20 to $40\,\mathrm{W\,m^{-2}}$ larger in HR$_\mathrm{ide}$ than in HR$_\mathrm{pp}$ (not shown). For comparison, the sensible heat flux is only about 10 to $20\,\mathrm{W\,m^{-2}}$ stronger in HR$_\mathrm{kpp}$ and HR$_\mathrm{tke}$.

4.3   Arctic Ocean

Although largely unknown, sparse observations indicate that turbulence in the Arctic Ocean is typically weak (Rainville and Winsor, 2008; Fer, 2009). The wind stress cannot act on the sea surface because of the insulating sea ice cover,
400   which is why the effect of the wind stress on vertical mixing decreases quadratically with the sea ice concentration in the simulations with PP and KPP (see Appendix A). In addition, brine rejection is less effective as a mixing mechanism because of the strong vertical salinity gradients in the cold halocline layer. Therefore, apart from enhanced mixing by episodic shear events, storms during ice-free conditions (Rainville and Woodgate, 2009), mesoscale eddies, or lateral intrusion along the boundaries, vertical diffusive mixing dominates over turbulent mixing (Fer, 2009).
405   Internal wave activity is almost absent, except above rough topographic features. In fact, internal waves are trapped at the place of their origin and do not propagate far into the Arctic Ocean. This trapping occurs because the Arctic Ocean is north of the critical latitude, which is $74.5\,°\mathrm{N}$ for the M$_2$ tide, beyond which the Earth's rotation prohibits freely propagating internal waves. As a result, they dissipate at or very close to their source region with properties similar to lee waves (Rippeth et al., 2015, 2017).
410   For this reason, there is little or no contribution to small-scale turbulence in the inner Arctic Ocean in HR$_\mathrm{ide}$, especially in the deep and flat-bottomed Canada basin. The eddy diffusivity K is up to two orders of magnitude smaller ($O(10^{-6}\,\mathrm{to}\,10^{-7}\,\mathrm{m^2\,s^{-1}})$) in HR$_\mathrm{ide}$ compared to the other simulations (Fig. 15), in which K is mostly at the constant background value ($1.05 \cdot 10^{-5}\,\mathrm{m^2\,s^{-1}}$).

Representing this trapping of internal waves is crucial to simulate eddy diffusivities that are more consistent with
415   microstructure measurements, which show low eddy diffusivities in deep, flat-bottomed basins, but elevated diffusivities above deep topography (Rainville and Winsor, 2008). The low diffusivities in deep basins agree well with observations from the Barneo ice camp drift, where $O(10^{-6}\,\mathrm{m^2\,s^{-1}})$ was measured below the mixed layer in the Amundsen Basin (Fer, 2009).

Lower vertical diffusivity under sea ice in the Arctic Ocean might cause denser water to enter the Nordic Seas (Kim
420   et al., 2015), which could then lead to denser overflows across the Greenland-Iceland-Scotland Ridge and a $14\,\%$ stronger upper cell of the AMOC. Indeed, HR$_\mathrm{ide}$ generates higher overflow volumes and a $10\,\%$ stronger AMOC, but these are probably caused more by denser water masses in the Greenland Sea. However, we cannot rule out the effect of denser water from the Arctic Ocean.

A contrasting example of higher diffusivities in the inner Arctic Ocean is a distinct band of strong mixing along and
425   above the Lomonosov Ridge (Fig. 15d). Here, internal waves break immediately after their formation and thus locally increase the small-scale turbulence, a process that was also directly measured by Rainville and Winsor (2008).

Assuming a constant background diffusivity thus largely overestimates the vertical mixing in the Arctic Ocean. Although the background diffusivity can be artificially reduced to mimic this low internal wave activity (e.g. Kim et al., 2015; Sein

20

et al., 2018), the very heterogeneous pattern described above would not be captured. The combination of TKE with IDEMIX is able to reproduce the spatial pattern and the correct magnitudes. It further provides an energetically more consistent solution that should be preferred.

4.4 Southern Ocean and Weddell Sea

4.4.1 Open-ocean convection in the Weddell Sea [..197]polynya

A well-known problem in ocean modelling is a too frequent semi-permanent Weddell Sea polynya caused by [..198]false deep convection bringing warm Circumpolar Deep Water (CDW) close to the surface (Sallée et al., 2013; Kjellsson et al., 2015; Heuzé et al., 2015; Stössel et al., 2015; Naughten et al., 2018). Possible explanations are insufficient freshwater supply (Kjellsson et al., 2015), mainly due to a lack of glacier melt water (Stössel et al., 2015), and insufficient wind mixing in summer (Timmermann and Beckmann, 2004; Sallée et al., 2013; Kjellsson et al., 2015), which causes a high salinity bias in the mixed layer that erodes the stratification; see a more detailed discussion in Gutjahr et al. (2019). In contrast to this view, Dufour et al. (2017) argue that deep convection in the Weddell Sea does not necessarily lead to an open-ocean polynya, because strong vertical mixing in low-resolution models inhibits the built-up of a subsurface heat reservoir that would be necessary for intermittent Weddell Sea polynyas.

We do not expect a realistic representation of the Weddell Sea polynya in our MPI-ESM1.2-HR 1950s control simulations, because they should develop intermittently only under pre-industrial conditions and grow out from Maud Rise polynyas (de Lavergne et al., 2014; Gordon, 2014; Kurtakoti et al., 2018; Campbell et al., 2019; Cheon and Gordon, 2019; Jena et al., 2019), for which high resolution ($0.1°$ or better) is required (Stössel et al., 2015; Dufour et al., 2017).

Although all simulations produce these semi-permanent Weddell Sea polynyas and thus too deep mixed layers (Fig. [..199]16), the area of excessive [..200]deep convection is reduced in HR$_{ide}$ (Fig. [..201]16e). [..202]Similarly, too deep mixed layers are simulated in the Ross Sea, except [..203]in HR$_{tke}$[..204], which simulates shallower mixed layers without further reduction when using IDEMIX (HR$_{ide}$). The Weddell Gyre is also linked to the Antarctic Circumpolar Current (ACC; Orsi et al., 1993; Cheon et al., 2019), because it controls the inflow of relatively warm and saline [..205]CDW into the inner Weddell Sea, possibly eroding the weak stratification and triggering deep convection. The simulated ACC transports through Drake passage (Tab. 3) are close to the recently observed $173.31 \pm 10.7\,\mathrm{Sv}$ (Donohue et al., 2016), whereby HR$_{tke}$ achieves the best estimate with $174\,\mathrm{Sv}$. [..206]Simulations with lower convection in the Weddell Sea produce lower transports of about [..207]161 to $163\,\mathrm{Sv}$

---

[197]removed: A long lasting
[198]removed: a spurious
[199]removed: 14
[200]removed: deep-convection
[201]removed: 14
[202]removed: Likewise
[203]removed: shallower mixed layers
[204]removed: ;
[205]removed: Circumpolar Deep Water
[206]removed: Models
[207]removed: $161 - 163\,\mathrm{Sv}$

455 (HR$_{pp}$ and HR$_{ide}$)[..[208]], whereas HR$_{kpp}$ produces a much higher transport of 192 Sv because of steeper isopycnals due to enhanced convection in the Weddell Sea. Since eddies are not resolved and the GM coefficient is rather low, there is no or too little eddy compensation to flatten the isopycnals.

One possible explanation why HR$_{ide}$ simulates less convection in the Weddell Sea is that IDEMIX creates [..[209]]more mixing above the shelf, [..[210]]which spreads near-surface freshwater [..[211]]laterally into the centre of the Weddell Gyre much
460 more efficiently (not shown). [..[212]]Fresher conditions in the Weddell Gyre [..[213]]favours the formation of sea ice, which [..[214]]insulates the ocean from further heat loss and thus impedes convection. In HR$_{ide}$, the average sea ice concentration in September is about 50 to 70 % in the Weddell Gyre ([..[215]]not shown), whereas it is considerably lower in the other simulations with concentrations of 20 to 50 %. Furthermore, the ice is also thicker with IDEMIX compared with the other simulations (Fig. 5d). Although the sea ice concentration is still too low, [..[216]]the spurious deep convection in the Weddell Sea is
465 reduced with IDEMIX.

4.4.2 Deep Mixing Band in the Southern Ocean

Another challenge for current ocean models is the representation of the Deep Mixing Band (DMB; DuVivier et al., 2018), which extends from the western Indian Ocean to the eastern Pacific Ocean and reaches MLDs of more than 700 m [..[217]](Holte et al., 2017, Fig. 16a). The DMB builds up over the winter months and is deepest in September. Subantarctic Mode Water
470 (SAMW; McCartney, 1977) forms in the DMB near the Subantarctic Front, just north of the ACC. The SAMW acts as an important carbon sink (e.g. Sabine et al., 2004) and it ventilates the mid-deep ocean (e.g. Sloyan and Rintoul, 2001; Jones et al., 2016), replenishing oxygen and nutrients (e.g. Sarmiento et al., 2004). [..[218]]It was shown that high resolution (0.1°) leads to deeper and thus more realistic MLDs in the DMB (Li and Lee, 2017; DuVivier et al., 2018; Gutjahr et al., 2019), but it is thought that fundamental vertical physics are missing in ocean models (DuVivier et al., 2018).
475 Although HR$_{pp}$ reproduces the [..[219]]DMB in the Indian Ocean, the mixed layers are too shallow [..[220]]in almost the entire Pacific sector (Fig. [..[221]]16b). [..[222]]KPP and TKE improve the representation of the DMB in the Pacific Ocean and [..[223]

---

[208]removed: and the model with stronger convection (HR$_{kpp}$)

[209]removed: a stronger

[210]removed: whereby

[211]removed: spreads much more efficiently in the lateral direction towards

[212]removed: This higher amount of freshwater

[213]removed: increases

[214]removed: then isolates

[215]removed: Fig. 15

[216]removed: IDEMIX improves the near-surface freshwater supply

[217]removed: (Holte et al., 2017, Fig. 14a)

[218]removed: Although it

[219]removed: mixing band

[220]removed: almost entirely in the Pacific Ocean

[221]removed: 14

[222]removed: In contrast, the sensitivity simulations

[223]removed: particularly

]simulate deeper mixed layers, especially in the Indian Ocean. The MLDs are close to observations (Fig. [..[224]]16c-e), albeit with a too wide DMB, which is probably caused by insufficient model resolution, since it becomes much narrower when an eddy-resolving model is used (Gutjahr et al., 2019). The choice of a mixing scheme other than PP has little influence on the

480 MLDs, except south of Tasmania, where TKE appears to produce the deepest [..[225]]mixed layers.

Although not observed by Argo floats, but common to all simulations are deeper mixed layers north of $50°$S in the Pacific Ocean east of New Zealand and in the South Atlantic. However, it should be kept in mind that comparing model simulations with Argo float data is always difficult, because the floats do not measure continuously in time and space and, in addition, we compare them with control simulations.

485 ## 5   Effects on the atmosphere

From section 3 the question arises whether atmospheric variables are influenced by a changed vertical mixing scheme. We briefly compare key quantities of the atmosphere and use ERA-Interim (Dee et al., 2011) from the period 1979–2005 as reference. This period and data was used to tune the atmospheric component ECHAM6.3 of the MPI-ESM1.2. [..[226]]

5.1   Near-surface fields

490 The 2 m air temperature (SAT; Fig. 17) is closely related to the SST and we find distinct effects on the bias by changing the vertical mixing scheme, not only over the ocean but also over land (Fig. 17). In the reference simulation (HR$_{PP}$) the pattern widely agrees with the SST bias (see section 3.4) with a pronounced cold bias in the North Atlantic and in the Nordic Seas. These cold biases seem to affect most parts of Europe as well. The most pronounced warm bias in the northern hemisphere extends over large parts of Canada and over the Labrador Sea. The warm bias over the Labrador

495 Sea is related to an over-extended area of convection (Fig. 12) that prevents the sea ice from extending far enough south (Fig. 4), causing the air masses over the open ocean to become too warm. In the sensitivity simulations, we find a reduction of the cold bias in the North Atlantic and in particular in the Greenland, Barents and Kara Seas. However, as with the SST bias, the air temperature over the subpolar gyre becomes warmer; in particular over the Labrador Sea, where all sensitivity simulations produce a larger convection area and less sea ice cover.

500 In the Southern Ocean, the SAT is too cold along the ACC by about $1°C$ and colder to the west of the Antarctic peninsula. The air temperature above the Weddell Sea, is warmer than in ERA-Interim, especially when using TKE, because of the large sensible heat fluxes from the Weddell Sea polynya. However, even though IDEMIX reduces the area and intensity of this polynya, there is no effect on the SAT, which requires further investigation in a future study.

Other quantities, such as wind speed or precipitation are not affected by changing the vertical mixing scheme in the

505 ocean.

---

[224]removed: 14
[225]removed: mixing
[226]removed: And furthermore, a difference could arise due to the different time periods we compare

5.2 Zonal temperature and velocity

The zonally averaged global air temperature is mostly too cold (Fig. 18) in the entire troposphere and too warm in the stratosphere compared to ERA-Interim. Warmer SSTs in the northern hemisphere with KPP and TKE propagate to higher layers of the troposphere. While warmer temperatures remain limited to the extratropics of the northern hemisphere in
510 HR_{tke} in comparison to HR_{pp} (significant at the 5 %-level), also the tropics and the southern hemisphere become warmer with KPP, which produces also the warmest troposphere.

The warmer extratropics with TKE result in a weaker meridional gradient that reduces the thermal wind and leads to a weaker jet stream in the northern hemisphere (Fig. 19c-d). However, in HR_{kpp} (Fig. 19b), no weakening of the northern hemispheric jet stream is seen, most likely because meridional gradients are maintained when the entire hemisphere is
515 uniformly warmer.

6 Conclusions

We have compared the effect of four different ocean vertical mixing schemes (PP, KPP, TKE, TKE+IDEMIX) on the ocean mean state in MPI-ESM1.2-HR simulations. The ocean mixing library CVMix (Griffies et al., 2015), which we extended with the TKE and TKE+IDEMIX schemes, allowed for a side-by-side comparison of these schemes.
520 [..[227]]

[..[228]]From the results described above emerges a consistent picture. Using KPP or TKE increases the convection in the [..[229]]

[..[230]]SPNA and Nordic Seas, but also in the southern hemisphere. Due to enhanced convection, the overflows from the Nordic Seas increase by about 10 [..[231]]%. Stronger overflows and increased inflow from the Indian Ocean into the
525 South Atlantic result in a stronger and deeper upper cell of the AMOC. The roughly 3 Sv (or 20 %) stronger AMOC transports more heat and salt into the SPNA and its marginal seas. The higher salinity favours deep convection, maintaining a stronger AMOC, whereas the higher heat transport increases the SSTs. The warmer SSTs affect the atmosphere, resulting in warmer extratropics with TKE, weakening the meridional temperature gradient and thus the jet stream in the

---

[227]removed: Although we conclude that shortcomings with respect to model resolution determine the global bias pattern in the ocean in our coupled simulations, the choice of the ocean vertical mixing scheme plays an important role for regional biases. In general, we find little sensitivity of the ocean surface, but considerable effects for the interior ocean. Overall, we cannot classify any scheme as superior to the others, as these schemes modify biases that vary with region or variable but produce a similar global-scale bias pattern.

[228]removed: All simulations show strong temperature and salinity biases in the Atlantic that originate from insufficient representations of the Mediterranean overflow water (MOW) and Agulhas leakage. The biases of MOW can be traced from the Atlantic Ocean to the Arctic Ocean via the GIN Seas and

[229]removed: Nordic Seas. Based on a recent study with an eddy-resolving version of MPI-ESM1.2 (Gutjahr et al., 2019), we know that most of these biases diminish at such a resolution. However, eddy-resolving resolution is computationally demanding and therefore it is important to investigate whether improved parameterisation can improve some of the hydrographic errors.

[230]removed: The sensitivity simulations using KPP, TKE, and TKE+IDEMIX, produce deeper than observed MLDs in the subpolar North Atlantic and the Nordic Seas, causing about

[231]removed: % higher overflow volumes and thus a stronger upper cell of the AMOC. In the Southern Ocean, however, the MLDS in the Deep Mixing Band agree better with observations from Argo floats

northern hemisphere. With KPP, the tropics and the southern hemisphere also become warmer, but without weakening of the jet stream due to a more uniform warming. These results highlight the clear advantage of using coupled models in which the surface state can evolve interactively, rather than air temperature or salinity being dictated by restoring as in ocean-only configurations.

[..232]KPP, TKE and TKE+IDEMIX produce similar results, but differ in some aspects. Most pronounced [..233]is that IDEMIX produces a more heterogeneous spatial pattern of vertical diffusivity, with generally lower values in deep and flat basins and [..234]increased turbulence over rough topography. This spatial pattern is particularly evident [..235]in the Arctic Ocean [..236]and fits better with microstructure measurements without having to artificially lower the background diffusivity.

In addition, IDEMIX improves the circulation and mixing in the Nordic Seas and in the Fram Strait, which reduces the warm bias of the Atlantic water layer in the Arctic Ocean. [..237]In the Southern hemisphere, IDEMIX reduces the spurious deep convection in the Weddell Sea because of enhanced mixing above the shelf that seems to increase the lateral transport of freshwater into the inner Weddell Sea, thereby impeding deep convection. The main advantages of IDEMIX is its energetically [..238]more consistent formulation without assuming an artificial background diffusivity and its flexibility that allows additional energy inputs, e.g. from the mesoscale eddy field.

Code and data availability. Model codes developed at MPI-M are intellectual property of MPI-M. Permission to access the MPI-ESM source code can be requested after registering at the MPI user forum (https://www.mpimet.mpg.de/en/science/models/mpi-esm/users-forum/, last accessed August 2020) and may be granted after accepting the MPI-M Software License Agreement (https://www.mpimet.mpg.de/fileadmin/models/MPIESM/mpi-m_sla_201202.pdf).

After registration, the model source code is accessible from https://doi.org/10.35089/WDCC/PRIMAVERA_MPI_ESM_source_code using branch *mpiesm-1.2.01-cvmix_GMD* for the KPP, TKE, and TKE+IDEMIX simulations and *mpiesm-1.2.01-primavera_PP_GMD* for the PP simulation. Primary data and scripts used in the analysis, and other supplementary information that may be useful in reproducing the author's work can be obtained from MPI PuRe (http://hdl.handle.net/21.11116/0000-0006-DB1E-3). Initial fields and all forcing fields can be downloaded from DKRZ LTA DOCU (https://cera-www.dkrz.de/WDCC/ui/cerasearch/entry?acronym=DKRZ_LTA_944_ds00001). The model code used for the simulations in the paper and the primary data have been provided to the anonymous reviewer and the topical editor.

---

[232]removed: Although extending the TKE scheme with IDEMIX does not improve these biases on a global scale, we notice some regional improvements

[233]removed: ,

[234]removed: elevated turbulence above

[235]removed: for

[236]removed: , which is more consistent with micromeasurements, without lowering the background artificially. Furthermore

[237]removed: This reduction of biases is similar to what was recently shown with high-resolution, eddy-resolving ocean models (Wang et al., 2018; Gutjahr et al., 2019). However, the

[238]removed: consistent link to TKE

Appendix A: Ocean vertical mixing schemes in MPI-ESM1.2

555 In this section we give a brief summary of the ocean vertical schemes that we have implemented into MPI-ESM1.2. The vertical mixing schemes were implemented via the Community Vertical Mixing (CVMix) library (Griffies et al., 2015; Van Roekel et al., 2018), except for the PP scheme. The KPP schema was already part of the CVMix library, which we therefore extended with the TKE and IDEMIX scheme. This extension will become part of the official CVMix library.

The schemes below aim to parameterise the vertical turbulent fluxes following this general flux-gradient or K-profile ap-
560 proach:

$$\overline{w'\lambda'} = -K_\lambda \left(\frac{\partial \Lambda}{\partial z} \right) + \Gamma_\lambda, \tag{A1}$$

with w' the vertical turbulent velocity, λ' the turbulent fluctuation of a quantity, λ a grid-scale quantity and the turbulent exchange coefficient ($K_\lambda > 0$) or also termed eddy viscosity for momentum flux and eddy diffusivity for tracer fluxes, such as temperature or salinity. Γ_λ represents any flux not proportional to the local gradient $\partial_z \Lambda$ and is referred to as *nonlocal flux*. In
565 our comparison, Γ_λ is only accounted for in the KPP scheme (A2).

A1 Pacanowski and Philander (1981, PP) scheme

In our control simulation the vertical turbulent diffusion and viscosity are based on a modified version of the Richardson-number dependent formulation by Pacanowski and Philander (1981) (PP scheme). The modifications are that (1) the vertical diffusivity is not dependent on the vertical viscosity, and (2) that the turbulent mixing in the ocean mixed layer is assumed to
570 depend on the cube of the 10 m wind speed (Marsland et al., 2003). This dependency decays exponentially with depth and with potential density difference to the surface. Since the classical approach by Pacanowski and Philander (1981) underestimates the turbulent mixing close to the surface (Marsland et al., 2003), this additional wind induced mixing (κ_w) is added, and defined as:

$$K_w(1) = (1 - A)^2 w_t U_{10}^3 \tag{A2}$$

575 $$K_w(k) = K_w(k - 1) \frac{\frac{\lambda}{\Delta z}}{\frac{\lambda}{\Delta z} + \delta_z \rho} e^{\frac{\lambda}{z_0}} \tag{A3}$$

with $k = 2, 3, \ldots, n$ the vertical model level, Δz the layer thickness, A the fractional sea ice concentration, U_{10} the 10 m wind speed, $w_t = 0.5 \cdot 10^{-3}/6.0^3$, $\lambda = 0.03$, and $z_0 = 40.0$ (e-folding depth) are adjustable parameters, and $\delta_z \rho$ the local static stability.

The total equation for the eddy vertical diffusivity then reads:

580 $$K_d(z) = \frac{d_{v,0}}{(1 + c_d Ri(z)^2)} + K_w(z) + d_{v,b}, \tag{A4}$$

26

with $d_{v,0} = 0.2 \cdot 10^{-2}\,\mathrm{m^2\,s^{-1}}$, $c_d = 5.0$, and the background diffusivity $d_{v,b} = 5 \cdot 10^{-5}\,\mathrm{m^2\,s^{-1}}$. The eddy vertical viscosity is parameterised as:

$$K_v(z) = \frac{a_{v,0}}{(1 + c_a Ri(z)^3)} + K_w(z) + a_{v,b},$$ (A5)

with $a_{v,0} = 0.2 \cdot 10^{-2}\,\mathrm{m^2\,s^{-1}}$, $c_a = 5.0$, and $a_{v,b} = 1.05 \cdot 10^{-5}\,\mathrm{m^2\,s^{-1}}$ the background viscosity. The eddy coefficients K_d and K_v are partially relaxed to the value at the previous time step by use of a time filter to avoid $2\Delta t$ oscillations (Marsland et al., 2003). Convection is parameterised as enhanced diffusivity ($K_d = 0.1\,\mathrm{m^2\,s^{-1}}$) for the PP scheme.

A2 K-profile parameterisation (KPP) scheme

The second simulation uses the K-profile parameterisation (KPP scheme) from Large et al. (1994) for the mixed layer. In general, a turbulent flux ($\overline{w'\lambda'} = \overline{w\lambda}$) of a quantity Λ (momentum, scalar tracers) are parameterised as:

$$\overline{w\lambda} = -K_\lambda \left(\frac{\partial \Lambda}{\partial z}\right) + K_\lambda^{\text{non-local}} \gamma_\lambda,$$ (A6)

with K_λ the local diffusivity for tracers or viscosity for momentum, z the depth, $K_\lambda^{\text{non-local}}$ the non-local diffusivity/viscosity, and a non-local term γ_λ. While the local flux (first term on the right hand side) depends directly on the local gradient of a quantity, the non-local flux (second term on the right hand side) redistributes the surface fluxes throughout the whole surface boundary layer, for example due to convection (see below).

The local diffusivity (K_λ) is calculated as:

$$K_\lambda(\sigma) = h\,w_\lambda(\sigma)G(\sigma),$$ (A7)

with $\sigma = z/h$ the dimensionless vertical coordinate ($0 \le \sigma \le 1$), z the depth below the sea surface, h the ocean boundary layer depth, w_λ a vertical turbulent velocity scale (either for scalar tracers or momentum), and $G(\sigma) = \sigma(1-\sigma)^2$ a universal shape function. Oftentimes, and also in our implementation, it is assumed that $K_\lambda^{\text{non-local}} = K_\lambda$ (Griffies et al., 2015).

The ocean boundary layer depth h is determined at the depth z where the bulk Richardson-number Ri_b becomes larger than a critical Richardson-number [..[239]]$Ri_c = 0.3$. The bulk Richardson-number at depth z is defined as:

$$Ri_b(z) = \frac{(z - z_{sl})\left[B_{sl} - B(z)\right]}{|\mathbf{U}_{sl} - \mathbf{U}(z)|^2 + U_t(z)^2},$$ (A8)

with z_{sl} the depth at the centre of the surface layer (defined as $0 \le z \le \epsilon h$), where we assume that the surface layer is $10\,\%$ ($\epsilon = 0.1$) of the ocean boundary layer depth h, as in Large et al. (1994). Since the calculation of the ocean boundary layer depth h requires Ri_b, which itself requires h, we face a cyclic problem. To solve this problem, we follow the column sampling method recommended by Griffies et al. (2015) (see details in their description).

---

[239]removed: $Ri_c = 0.7$

B_{sl} is the surface layer averaged buoyancy flux, $B(z)$ the local buoyancy flux, U_{sl} the surface layer averaged velocity, $U(z)$ the local velocity and $U_t(z)$ a parameterisation for unresolved turbulent vertical velocity shear that reduces the bulk Richardson number (see e.g. Griffies et al. (2015) for the definition of the unresolved turbulent shear).

610   The vertical turbulent velocity scale w_λ is calculated as follows:

$$w_\lambda(\sigma) = \frac{\kappa u_*(1-A)^2}{\Phi_\Lambda(\zeta)},$$ (A9)

with $\kappa = 0.4$ the von-Kármán constant, u_* the surface friction velocity that reduces with increasing fractional sea ice (A), Φ_Λ a dimensionless similarity function (momentum or scalar tracer), depending on $\zeta = \sigma h/L$, with $L = \frac{u_*^3}{\kappa B_f}$ the Monin-Obukhov length scale. B_f is the buoyancy forcing in the ocean boundary layer. Under neutral forcing ($\zeta = 0 \rightarrow \Phi_\Lambda(0) = 1$), Eq. A9

615 reduces to $w_\lambda(\sigma) = \kappa u_*(1-A)^2$. We use the similarity functions of Large et al. (1994) (cf see Appendix B) for stable ($\zeta > 0$), unstable ($\zeta_m < \zeta < 0$ or $\zeta_s < \zeta < 0$), and very unstable conditions ($\zeta < 0$):

$$\Phi_m(\zeta) = \begin{cases} 1 + 5\zeta & \zeta > 0 \\ (1 - 16\zeta)^{-1/4} & \zeta_m < \zeta < 0 \\ (a_m - c_m\zeta)^{-1/3} & \zeta < -\zeta_m \end{cases}$$ (A10)

$$\Phi_s(\zeta) = \begin{cases} 1 + 5\zeta & \zeta > 0 \\ (1 - 16\zeta)^{-1/4} & \zeta_s < \zeta < 0 \\ (a_s - c_s\zeta)^{-1/3} & \zeta < \zeta_s \end{cases}$$ (A11)

with $\zeta_m = -0.2$, $\zeta_s = -1.0$, $a_m = 1.26$, $c_m = 8.38$, $a_s = -28.86$, and $c_s = 98.96$. We do not match the diffusivities at the

620 base of the mixed layer to avoid overshooting tracers, as recommended by Griffies et al. (2015).

     For the non-local flux term in Eq. A6, it is assumed that $K_\lambda = K_\lambda^{\text{non-local}}$, so that this term simplifies to: $K_\lambda \gamma_\lambda$. The non-local flux γ_λ is only non-zero if $B_f < 0$ (buoyancy gain at the surface) and only for scalar tracers such as temperature, θ, or salinity, s; for momentum it is set to zero. With the assumption $K_\lambda = K_\theta = K_s$ and a universal shape function ($G(\sigma)$), the non-local fluxes take the form:

625 $$\overline{w\theta}^{\text{non-local}} = K_\lambda \gamma_\theta = -G(\sigma)C_s \left(\frac{Q^{\text{heat}}}{\rho_0 C_P^0} \right)$$ (A12)

$$\overline{ws}^{\text{non-local}} = K_\lambda \gamma_s = -G(\sigma)C_s Q^s,$$ (A13)

with the non-local terms for temperature (γ_θ) and salinity (γ_s), a dimensionless coefficient $C_s = C_*\kappa(c_s\kappa\epsilon)^{1/3}$ with a dimensionless constant $C_* = 10$, $\rho_0 = 1025\,\text{kg}\,\text{m}^{-3}$ the reference sea water density, C_P^0 the seawater heat capacity at constant pressure ($\text{J}\,\text{kg}^{-1}\,{}^\circ\text{C}^{-1}$), Q_s the mass flux of salt ($\text{kg}\,\text{m}^{-2}\text{s}^{-1}$) and the heat flux Q^{heat} ($\text{W}\,\text{m}^{-2}$) that considers penetrative

630 shortwave radiation. See further details on the KPP scheme in Griffies et al. (2015) and Van Roekel et al. (2018).

     Below the mixed layer, we use the PP scheme with the enhanced diffusivity parameterisation for convection, as described in section A1.

A3 TKE and IDEMIX schemes

A schematic overview of the TKE and IDEMIX schemes are depicted in Fig. A1. IDEMIX parameterises the internal wave
energy (E_{iw}) in terms of a budget equation:

$$\frac{\partial E_{iw}}{\partial t} = \nabla_h \nu_0 \tau_h \nabla_h \nu_0 E_{iw} + \frac{\partial}{\partial z}\left(c_0 \tau_v \frac{\partial c_0 E_{iw}}{\partial z}\right) - \epsilon_{iw} \qquad (A14)$$

with ν_0 the lateral group velocity, τ_h a lateral time scale on which lateral anisotropies are eliminated by nonlinear wave-wave
interactions, c_0 the weighted average vertical group velocity, z the vertical coordinate, τ_ν a time scale of on the order of days,
and $\epsilon_{iw} = -\alpha E_{iw}^2$ the dissipation of internal wave energy, with α a structure function depending on the stratification (for details
see (Olbers and Eden, 2013)). The first and second term on the right-hand side (RHS) parameterise the horizontal and vertical
propagation of internal waves, respectively. Internal wave energy is dissipated by the last term on the [..[240]]RHS of Eq. A14.
This term acts as an energy transfer from internal wave energy to turbulent kinetic energy (see Eq. A15 below).

Internal waves are forced in IDEMIX by surface and bottom fluxes applied as boundary conditions in the second term on the
RHS of Eq. A14. Currently, we use time constant fields for the energy fluxes at the surface and at the bottom (see Fig. A2), as
in [..[241]]Eden et al. (2014). The energy flux that we use as [..[242]]surface boundary condition is 20 % of the wind input into
the inertial band of the mixed layer (Jochum et al., 2013), as determined by Rimac et al. (2013) (inertial pumping mechanism).
We neglect, however, other sources exciting internal waves near the surface, for instance buoyancy plumes that overshoot the
mixed layer base, vertical roll vortices of turbulent eddies, or Langmuir circulation that undulates internal waves (Czeschel
and Eden, 2019). At the bottom, barotropic tides interact with the bottom roughness and convert energy to internal waves. This
energy flux is prescribed from Jayne (2009), with the constraint that this energy source is not flow-aware.

In commonly used vertical mixing schemes, such as KPP (Large et al., 1994) or TKE (Gaspar et al., 1990), the breaking
of internal waves is usually parameterised by simply assuming a constant background diffusivity (either a scalar or profile)
or constant background TKE value. By using TKE with IDEMIX, the constant background diffusivity is replaced by one
that is diagnosed from the internal wave energy using the Osborn-Cox relation. We use the recommended parameter set from
Pollmann et al. (2017), who compared TKE coupled to IDEMIX with Argo float data in standalone ocean simulations.

The modified TKE equation (Eden et al., 2014) then reads:

$$\frac{d\bar{E}_{tke}}{dt} = -\partial_z(\text{fluxes}) + c_u K (\partial_z \bar{\mathbf{u}}^2) - c_b K N^2 - \epsilon_{tke} + \epsilon_{iw}, \qquad (A15)$$

with the dimensionless parameters c_u and c_b, which are related by $c_u = c_b R_i / R_f$. The first term on the RHS describes the
redistribution of TKE in the vertical. Surface fluxes enter as boundary conditions to this term. The second term describes the
vertical momentum fluxes acting on the shear of the mean flow, transferring energy from the mean flow to TKE. The third term
is the buoyancy term that transfers energy to the potential energy of the mean flow, thereby decreasing TKE. The dissipation

---

[240]removed: rhs

[241]removed: Olbers and Eden (2013). To this end, the energy flux which

[242]removed: upper

of TKE (fourth term) is parameterised as $\epsilon_{tke} = \bar{E}_{tke}^{2/3} L^{-1}$ with the mixing length $L = \sqrt{2\bar{E}_{tke}/N^2}$ (Blanke and Delecluse, 1993; Eden et al., 2014). The last term on the RHS is then the new contribution from IDEMIX, which is absent when using TKE without IDEMIX.

665   The diffusivity is parameterised as $K = \bar{E}_{tke}^{1/2} L$ by assuming the same mixing length as for the dissipation. If TKE is used alone without being combined with IDEMIX, then a background diffusivity is assumed to represent internal wave breaking (Eden et al., 2014). When TKE is used alone without being coupled to IDEMIX, the turbulent kinetic energy is set to a background value of $E_{\min} = 10^{-6}\,\mathrm{m^2 s^{-2}}$. The corresponding diffusivity in this case reads $K = \sqrt{2} c_b E_{min}/N$.

680   References

Adcroft, A. J., Hill, C., and Marshall, J.: Representation of Topography by Shaved Cells in a Height Coordinate Ocean Model, Mon. Weather Rev., 125, 2293–2315, https://doi.org/10.1175/1520-0493(1997)125<2293:ROTBSC>2.0.CO;2, 1997.

Aksenov, Y., Ivanov, V. V., Nurser, A. J. G., Bacon, S., Polyakov, I. V., Coward, A. C., Naveira-Garabato, A. C., and Beszczynska-Moeller, A.: The Arctic Circumpolar Boundary Current, J. Geophys. Res., 116, C09 017, https://doi.org/10.1029/2010JC006637, 2011.

685   Aldama-Campino, A. and Döös, K.: Mediterranean overflow water in the North Atlantic and its multidecadal variability, Tellus A: Dynamic Meteorology and Oceanography, 72:1, 1–10, https://doi.org/10.1080/16000870.2018.1565027, 2020.

Axell, L. B.: Wind-driven internal waves and Langmuir circulations in a numerical ocean moel of the southern Baltic Sea, J. Geophys. Res., 107(C11), 3204, https://doi.org/10.1029/2001JC000922., 2002.

Benjamini, Y. and Hochberg, Y.: Controlling the false discovery rate: a practical and powerful approach to multiple testing, Journal of the
690   Royal Statistical Society, 57, 289–300, https://doi.org/10.1111/j.2517-6161.1995.tb02031.x, 1995.

Berx, B., Hansen, B., Østerhus, S., Larsen, M. K., Sherwin, T., and Jochumsen, K.: Combining in situ measurements and altimetry to estimate volume, heat and salt transport variability through the Faroe-Shetland Channel, Ocean Sci., 2, 127–146, https://doi.org/10.5194/os-9-639-2013, 2013.

Blanke, B. and Delecluse, P.: Variability of the Tropical Atlantic Ocean Simulated by a General Circulation Model with Two Different Mixed-
695   Layer Physics, J. Phys. Oceanogr., 23, 1363–1388, https://doi.org/10.1175/1520-0485(1993)023<1363:VOTTAO>2.0.CO;2, 1993.

Breivik, ., Mogensen, K., Bidlot, J.-R., Balmaseda, M. A., and Janssen, P. A. E. M.: Surface wave effects in the NEMO ocean model: Forced and coupled experiments, J. Geophys. Res. Oceans, 120, 2973–2992, https://doi.org/10.1002/2014JC010565, 2015.

Brüggemann, N. and Katsman, C. A.: Dynamics of Downwelling in an Eddying Marginal Sea: Contrasting the Eulerian and the Isopycnal Perspective, J. Phys. Oceanogr., 49, 3017–3035, https://doi.org/10.1175/JPO-D-19-0090.1, 2019.

700   Campbell, E. C., Wilson, E. A., Moore, G. W. K., Riser, S. C., Brayton, C. E., Mazloff, M. R., and Talley, L. D.: Antarctic offshore polynyas linked to Southern Hemisphere climate anomalies, Nature, 570, 319–325, https://doi.org/10.1038/s41586-019-1294-0, 2019.

Carsey, F. D.: Microwave observation of the Weddell Polynya, Mon. Weath. Rev., 108, 2032–2044, https://doi.org/10.1175/1520-0493(1980)108<2032:MOOTWP>2.0.CO;2, 1980.

Chatterjee, S., Rai, R. P., Bertino, L., Skagseth, Ø., Ravichandran, M., and Johannessen, O. M.: Role of Greenland Sea Gyre Circulation on
705   Atlantic Water Temperature Variability in the Fram Strait, Geophys. Res. Lett., 45, 8399–8406, https://doi.org/10.1029/2018GL079174, 2018.

Cheon, W. G., Park, Y.-G., Toggweiler, J. R., and Lee, S.-K.: The Relationship of Weddell Polynya and Open-Ocean Deep Convection to the Southern Hemisphere Westerlies, J. Phys. Oceanogr., 44 (2), 694–713, https://doi.org/10.1175/JPO-D-13-0112.1, 2019.

Cheon, W. G. G. and Gordon, A. L.: Open-ocean polynyas and deep convection in the Southern Ocean, Sci. Rep., 9, 6935,
710   https://doi.org/10.1038/s41598-019-43466-2, 2019.

Childers, K. H., Flagg, C. N., and Rossy, T.: Direct velocity observations of volume flux between Iceland and the Shetland Islands, J. Geophys. Res. Oceans, 119, 5934–5944, https://doi.org/10.1002/2014JC009946, 2014.

Crews, L., Sundfjord, A., and Hattermann, T.: How the Yermak Pass Branch Regulates Atlantic Water inflow to the Arctic Ocean, J. Geophys. Res. Oceans, 124, 267–280, https://doi.org/10.1029/2018JC014476, 2019.

715   Czeschel, L. and Eden, C.: Internal Wave Radiation through Surface Mixed Layer Turbulence, J. Phys. Oceanogr., 49, 1827–1844, https://doi.org/10.1175/JPO-D-18-0214.1, 2019.

Danabasoglu, G., Large, W. G., Tribbia, J. T., Gent, P. R., Briegleb, B. P., and McWilliams, J. C.: Diurnal Coupling in the Tropical Oceans of CCSM3, J. Climate, 19 (11), 2347–2365, https://doi.org/10.1175/JCLI3739.1, 2006.

de Lavergne, C., Palter, J. B., Galbraith, E. D., Bernardello, R., and Marinov, I.: Cessation of deep convection in the open Southern Ocean under anthropogenic climate change, Climate Change, 4, 278–282, https://doi.org/10.1038/nclimate2132, 2014.

Dee, D. P., Uppala, S. M., Simmons, A. J., Berrisford, P., Poli, P., Kobayashi, S., Andrae, U., Balmaseda, M. A., Balsamo, G., Bauer, P., Bechtold, P., Beljaars, A. C. M., van de Berg, L., Bidlot, J., Bormann, N., Delsol, C., Dragani, R., Fuentes, M., Geer, A. J., Haimberger, L., Healy, S. B., Hersbach, H., Hólm, E. V., Isaksen, L., Kåberg, P., Köhler, M., Matricardi, M., McNally, A. P., Monge-Sanz, B. M., Morcrette, J.-J., Park, B.-K., Peubey, C., de Rosnay, P., Tavolato, C., Thépaut, J.-N., and Vitart, F.: The ERA-Interim reanalysis: configuration and performance of the data assimilation system, Q. J. R. Meteorol. Soc., 137, 553–597, https://doi.org/10.1002/qj.828, 2011.

Dengg, J. A., Beckmann, A., and Gerdes, R.: The Warmwatersphere of the North Atlantic Ocean, chap. The Gulf Stream separation problem, pp. 253–290, Gebr. Bornträger, Berlin, 1996.

Dmitrenko, I. A., Rudels, B., Kirilov, S. A., Aksenov, Y. O., Lien, V. S., Ivanov, V. V., Schauer, U., Polyakov, I. V., Coward, A., and Barber, D. G.: Atlantic water flow into the Arctic ocean through the St. Anna Trough in the northern Kara Sea, J. Geophys. Res. Oceans, 120, 5158–5178, https://doi.org/10.1002/2015JC01080, 2015.

Donohue, K. A., Tracey, K. L., Watts, D. R., Chidichimo, M. P., and Chereskin, T. K.: Mean Antarctic Circumpolar Current transport measured in Drake Passage, Geophys. Res. Lett., 43, 11 760–11 767, https://doi.org/10.1002/2016GL070319, 2016.

Dufour, C. O., Morrison, A. K., Griffies, S. M., Frenger, I., Zanowski, H., and Winton, M.: Preconditioning of the Weddell Sea Polynya by the Ocean Mesoscale and Dense Water Overflows, J. Climate, 30, 7719–7737, https://doi.org/10.1175/JCLI-D-16-0586.1, 2017.

DuVivier, A. K., Large, W. G., and Small, R. J.: Argo observations of the deep mixing band in the Southern Ocean: A salinity modeling challenge., J. Geophys. Res. Oceans, 123, 7599–7617, https://doi.org/10.1029/2018JC014275, 2018.

Eden, C. and Böning, C.: Sources of Eddy Kinetic Energy in the Labrador Sea, J. Phys. Oceanogr., 32, 3346–3363, https://doi.org/10.1175/1520-0485(2002)032<3346:SOEKEI>2.0.CO;2, 2002.

Eden, C., Czeschel, L., and Olbers, D.: Toward Energetically Consistent Ocean Models, J. Phys. Oceanogr., 44, 3160–3184, https://doi.org/10.1175/JPO-D-13-0260.1, 2014.

EUMETSAT Ocean and Sea Ice Satellite Application: Global sea ice concentration reprocessing dataset 1978-2015 (v1.2, 2015), [Online], http://osisaf.met.no, Norwegian and Danish Meteorological Institutes, 2015.

Fer, I.: Weak vertical diffusion allows maintenance of cold halocline in the central Arctic, Atmos. Ocean. Sci. Lett., 2(3), 148–152, https://doi.org/10.1080/16742834.2009.11446789, 2009.

Fer, I., Skogseth, R., and Geyer, F.: Internal Wave and Mixing in the Marginal Ice Zone near Yermak Plateau, J. Phys. Oceanogr., 40, 1613–1630, https://doi.org/10.1175/2010JPO4371.1, 2010.

Fieg, K., Gerdes, R., Fahrbach, E., Beszczynska-Möller, A., and Schauer, U.: Simulation of oceanic volume transports through Fram Strait 1995–2005, Ocean Dyn., 60, 491–502, https://doi.org/10.1007/s10236-010-0263-9, 2010.

Fox-Kemper, B., Adcroft, A., Böning, C. W., Chassignet, E. P., Curchitser, E., Danabasoglu, G., Eden, C., England, M. H., Gerdes, R., Greatbatch, R. J., Griffies, S. M., Hallberg, R. W., Hanert, E., Heimbach, P., Hewitt, H. T., Hill, C. N., Komuro, Y., Legg, S., Le Sommer, J., Masina, S., Marsland, S. J., Penny, S. G., Qiao, F., Ringler, T. D., Treguier, A. M., Tsujino, H., Uotila, P., and Yeager, S. G.: Challenges and Prospects in Ocean Circulation Models, Frontiers in Marine Science, 6, 65, https://doi.org/10.3389/fmars.2019.00065, 2019.

Garrett, C.: Internal tides and ocean mixing, Science, 301, 1858–1859, https://doi.org/10.1126/science.1090002, 2003.

Gaspar, P., Grégoris, Y., and Lefevre, J.-M.: A simple eddy kinetic energy model for simulations of the oceanic vertical mixing: Tests at station
755   Papa and long-term upper ocean study site, J. Geophys. Res. Oceans, 95, 16 179–16 193, https://doi.org/10.1029/JC095iC09p16179, 1990.

Gent, P. R.: A commentary on the Atlantic meridional overturning circulation stability in climate models, Ocean Model., 122, 57–66, https://doi.org/10.1016/j.ocemod.2017.12.006, 2018.

Gent, P. R., Willebrand, J., McDougall, T. J., and McWilliams, J. C.: Parameterizing Eddy-Induced Tracer Transports in Ocean Circulation Models, J. Phys. Oceanogr., 25, 463–474, https://doi.org/10.1175/1520-0485(1995)025<0463:PEITTI>2.0.CO;2, 1995.

760   Georgiou, S., van der Boog, C. G., N., B., Ypma, S. L., Pietrzak, J. D., and Katsman, C. A.: On the interplay between downwelling, deep convection and mesoscale eddies in the Labrador Sea, Ocean Modelling, 135, 56–70, https://doi.org/10.1016/j.ocemod.2019.02.004, 2019.

Good, S. A., Martin, M. J., and Rayner, N. A.: EN4: quality controlled ocean temperature and salinity profiles and monthly objective analyses with uncertainty estimates, J. Geophys. Res., 118, 6704–6716, https://doi.org/10.1002/2013JC009067, 2013.

Gordon, A. L.: Deep Antarctic Convection West of Maud Rise, J. Phys. Oceanogr., 8, 600–612, https://doi.org/10.1175/1520-
765   0485(1978)008<0600:DACWOM>2.0.CO;2, 1978.

Gordon, A. L.: Southern Ocean polynya, Nature Clim. Change, 4, 249–250, https://doi.org/10.1038/nclimate2179, 2014.

Griffies, S. M., Levy, M., Adcroft, A. J., Danabasoglu, R., Hallberg, R. W., Jacobsen, D., Large, W., and Ringler, T. D.: Theory and numerics of the Community Ocean Vertical Mixing (CVMix) Project, Tech. rep., NOAA/Geophysical Fluid Dynamics Laboratory, Princeton, NJ, https://github.com/CVMix/CVMix-description, 2015.

770   Gutjahr, O., Putrasahan, D., Lohmann, K., Jungclaus, J. H., von Storch, J.-S., Brüggemann, N., Haak, H., and Stössel, A.: Max Planck Institute Earth System Model (MPI-ESM1.2) for the High-Resolution Model Intercomparison Project (HighResMIP), Geosci. Model Dev., 12, 3241–3281, https://doi.org/10.5194/gmd-12-3241-2019, 2019.

Haarsma, R. J., Roberts, M. J., Vidale, P. L., Senior, C. A., Bellucci, A., Bao, Q., Chang, P., Corti, S., Fučkar, N. S., Guemas, V., von Harden-berg, J., Hazeleger, W., Kodama, C., Koenigk, T., Leung, L. R., Lu, J., Luo, J.-J., Mao, J., Mizielinski, M. S., Mizuta, R., Nobre, P., Satoh,
775   M., Scoccimarro, E., Semmler, T., Small, J., and von Storch, J.-S.: High Resolution Model Intercomparison Project (HighResMIP v1.0) for CMIP6, Geosci. Model Dev., 9, 4185–4208, https://doi.org/10.5194/gmd-9-4185-2016, 2016.

Hagemann, S. and Gates, L. D.: Improving a subgrid runoff parameterization scheme for climae models by the use of a high resolution data derived from satellite observations, Climate Dyn., 21, 349–359, https://doi.org/10.1007/s00382-003-0349-x, 2003.

Hansen, B., Østerhus, S., Quadfasel, D., and Turrell, W.: Already the day after tomorrow?, Science, 304, 953–954,
780   https://doi.org/10.1126/science.1100085, 2004.

Hansen, B., Larsen, K. M. H., Hátún, H., Kristiansen, R., Mortensen, E., and Østerhus, S.: Transport of volume, heat, and salt towards the Arctic in the Faroe Current 1993–2013, Ocean Sci., 11, 743–757, https://doi.org/10.5194/os-11-743-2015, 2015.

Hansen, B., Húsgarð, K. M., Hátún, H., and Østerhus, S.: A stable Faroe Bank Channel overflow 1995–2015, Ocean Sci., 12, 1205–1220, https://doi.org/10.5194/os-12-1205-2016, 2016.

785   Hansen, B., Poulsen, T., Larsen, K. M. H., Hátún, H., Østerhus, S., Darelius, E., Berx, B., Quadfasel, D., and Jochumsen, K.: Atlantic water flow through the Faroese Channel, Ocean Sci., 13, 873–888, https://doi.org/10.5194/os-13-873-2017, 2017.

Hattermann, T., Isachsen, P. E., von Appen, W.-J., Albretsen, J., and Sundfjord, A.: Eddy-driven recirculation of Atlantic Water in Fram Strait, Geophys. Res. Lett., 43, 3406–3414, https://doi.org/10.1002/2016GL068323, 2016.

Heuzé, C., Ridley, J. K., Calvert, D., Stevens, D. P., and Heywood, K. J.: Increasing vertical mixing to reduce Southern Ocean deep convection
790   in NEMO3.4, Geoscientific Model Development, 8, 3119–3130, https://doi.org/10.5194/gmd-8-3119-2015, 2015.

Holloway, G., Dupont, F., Golubeva, E., Haekkinen, S., Hunke, E., Jin, M., Karcher, M., Kauker, F., Maltrud, M., Maqueda, M. A. M., Maslowski, W., Platov, G., Stark, D., Steele, M., Suzuki, T., Wang, J., and Zhang, J.: Water properties and circulation in Arctic Ocean models, Geophys. Res. Oceans, 112, C04S03, https://doi.org/10.1029/2006JC003642, 2007.

Holte, J., Talley, L. D., Gilson, J., and Roemmich, D.: An Argo mixed layer climatology and database, Geophys. Res. Lett., 44, 5618–5626, https://doi.org/10.1002/2017GL073426, 2017.

Jayne, S. R.: The impact of abyssal mixing parameterizations in an ocean general circulation model, J. Phys. Oceanogr., 39, 1756–1775, https://doi.org/10.1175/2009JPO4085.1, 2009.

Jena, B., Ravichandran, M., and Turner, J.: Recent Reoccurrence of Large Open-Ocean Polynya on the Maud Rise Seamount, Geophys. Res. Lett., 46, 4320–4329, https://doi.org/10.1029/2018GL081482, 2019.

Jochum, M., Briegleb, B. P., Danabasoglu, G., Large, W. G., Norton, N. J., Jayne, S. R., Alford, M. H., and Bryan, F. O.: The impact of oceanic near-inertial waves on climate, J. Climate, 26, 2833–2844, https://doi.org/10.1175/JCLI-D-12-00181.1, 2013.

Jochumsen, K., Quadfasel, D., Valdimarsson, H., and Jónsson, S.: Variability of the Denmark Strait overflow: Moored time series from 1996–2011, J. Geophys. Res., 117, C12 003, https://doi.org/10.1029/2012JC008244, 2012.

Jochumsen, K., Moritz, M., Nunes, N., Quadfasel, D., Larsen, K. M. H., Hansen, B., Valdimarsson, H., and Jonsson, S.: Revised transport estimates of the Denmark Strait overflow, J. Geophys. Res., 122, 3434–3450, 2017.

Jones, D. C., Meijers, J. S., Shuckburgh, E., Sallée, J.-B., Haynes, P., McAufield, E. K., and Mazloff, M. R.: How does Subantarctic Mode Water vertilate the Southern Hemisphere subtropics?, J. Geophys. Res. Oceans, 121, 6558–6582, https://doi.org/10.1002/2016JC011680, 2016.

Jungclaus, J. H., Fischer, N., Haak, H., Lohmann, K., Marotzke, J., Matei, D., Mikolajewicz, U., Notz, D., and von Storch, J. S.: Characteristics of the ocean simulations in the Max Planck Institute Ocean Model (MPIOM), the ocean component of the MPI-Earth system model, J. Adv. Model. Earth Syst., 5, 422–446, https://doi.org/10.1002/jame.20023, 2013.

Katsman, C. A., Drijfhout, S. S., Dijkstra, H. A., and Spall, M. A.: Sinking of Dense North Atlantic Waters in a Global Ocean Model: Location and Controls, J. Geophys Res. Oceans, 123, 3563–3576, https://doi.org/10.1029/2017JC013329, 2018.

Kawasaki, T. and Hasumi, H.: The inflow of Atlantic water at the Fram Strait and its interannual variability, J. Geophys. Res. Oceans., 121, 502–519, https://doi.org/10.1002/2015JC011375, 2016.

Kim, S. Y., Lee, H. J., Park, J.-H., and Kim, Y. H.: Effects of Reduced Vertical Mixing Under Sea Ice on Atlantic Meridional Overturning Circulation (AMOC) in a Global Ice-Ocean Model, Ocean Sci. J., 50 (2), 155–161, https://doi.org/10.1007/s12601-015-0012-6, 2015.

Kjellsson, J., Holland, P. R., Marshall, G. J., Mathiot, P., Aksenov, Y., Coward, A. C., Bacon, S., Megann, A. P., and Ridley, J.: Model sensitivity of the Weddell and Ross seas, Antarctica, to vertical mixing and freshwater forcing, Ocean Modelling, 94, 141–152, https://doi.org/10.1016/j.ocemod.2015.08.003, 2015.

Koenig, Z., Provost, C., Sennéchael, N., Garric, G., and Gascard, J.-C.: The Yermak Pass Branch: A major pathway for Atlantic water north of Svalbard?, J. Geophys Res. Oceans, 122, 9332–9349, https://doi.org/10.1002/2017JC013271, 2017.

Kurtakoti, P., Veneziani, M., Stössel, A., and Weijer, W.: Preconditioning and Formation of Maud Rise Polynyas in a High-Resolution Earth System Model, J. Climate, 31, 9659–9678, https://doi.org/10.1175/JCLI-D-18-0392.1, 2018.

Large, W. G., McWilliams, J. C., and Doney, S. C.: Oceanic vertical mixing: A review and a model with a nonlocal boundary layer parameterization, Rev. Geophys., 21, 363–403, https://doi.org/10.1029/94RG01872, 1994.

Li, Q. and Fox-Kemper, B.: Assessing the effects of Langmuir turbulence on the entrainment buoyancy flux in the ocean surface boundary layer, J. Phys. Oceanogr., 47, 2863–2886, https://doi.org/10.1175/JPO-D-17-0085.1, 2017.

34

Li, Q. and Lee, S.: A mechanism of mixed-layer formation in the Indo-western Pacific Southern Ocean: Preconditioning by an eddydriven jet-scale overturning circulation, J. Phys. Oceanogr., 47, 2775–2772, https://doi.org/10.1175/JPO-D-17-0006.1, 2017.

Li, Q., Reichl, B. G., Fox-Kemper, B., Adcroft, A. J., Belcher, S. E., Danabasoglu, G., Grant, A. L. M., Griffies, S. M., Hallberg, R., Hara, T., Harcourt, R. R., Kukulka, T., Large, W. G., McWilliams, J. C., Pearson, B., Sullivan, P. P., Van Roekel, L., Wang, P., and Zheng, Z.: Comparing Ocean Surface Boundary Vertical Mixing Schemes Including Langmuir Turbulence, Journal of Advances in Modeling Earth Systems, 11, https://doi.org/10.1029/2019MS001810, 2019.

Liang, X. and Losch, M.: On the effects of increased vertical mixing on the Arctic Ocean and sea ice, J. Geophys. Res. Oceans, 26, 2833–2844, https://doi.org/10.1029/2018JC014303, 2018.

Lien, V. S. and Trofimov, A. G.: Formation of Barents Sea Branch Water in the north-eastern Barents Sea, Polar Research, 32 (1), 18 905, https://doi.org/10.3402/polar.v32i0.18905, 2013.

Lozier, M. S. and Sindlinger, L.: On the source of Mediterranean Overflow Water property changes, J. Phys. Oceanogr., 39, 1800–1817, https://doi.org/10.1175/2009JPO4109.1, 2008.

Marnela, M., Rudels, B., Houssais, M.-N., Beszczynska-Möller, A., and Eriksson, P.: Recirculation in the Fram Strait and transports of water in and north of the Fram Strait derived from CTD data, Ocean Sci., 9, 499–519, https://doi.org/10.5194/os-9-499-2013, 2013.

Marsland, S. J., Haak, H., Jungclaus, J. H., Latif, M., and Röske, F.: The Max Planck Institute global ocean/sea ice model with orthogonal curvilinear coordinates, Ocean Model., 5, 91–127, https://doi.org/10.1016/S1463-5003(02)00015-X, 2003.

Mauritsen, T., Stevens, B., Roeckner, E., Crueger, T., Esch, M., Giorgetta, M., Haak, H., Jungclaus, J. H., Klocke, D., Matei, D., Mikolajewicz, U., Notz, D., Pincus, R., Schmidt, H., and Tomassini, L.: Tuning the climate of a global model, J. Adv. Model. Earth Syst., 4(3), M00A01, https://doi.org/10.1029/2012MS000154, 2012.

Mauritsen, T., Bader, J., Becker, T., Behrens, J., Bittner, M., Brokopf, R., Brovkin, V., Claussen, M., Crueger, T., Esch, M., Fast, I., Fiedler, S., Fläschner, D., Gayler, V., Giorgetta, M., Haak, M., Hagemann, S., Hedemann, C., Hohenegger, C., Ilyina, T., Jahns, T., Jimenéz-de-la Cuesta, D., Jungclaus, J., Kleinen, T., Kloster, S., Kracher, D., Kinne, S., Kleberg, S., Lasslop, G., Kornblueh, L., Marotzke, J., Matei, D., Meraner, K., Mikilajewicz, U., Modali, K., Möbis, B., Müller, W. A., Nabel, J. E. M. S., Nam, C. C. W., Notz, D., Nyawira, S.-S., Paulsen, H., Peters, K., Pincus, R., Pohlmann, H., Pongratz, J., Popp, M., Raddatz, T. J., Rast, S., Redler, R., Reick, C. H., Rohrschneider, T., Schemann, V., Schmidt, H., Schnur, R., Schulzweida, Six, K. D., Stein, L., Stemmler, I., Stevens, B., von Storch, J.-S., Tian, F., Voigt, A., Vrese, P., Wieders, K.-H., Wilkenskjeld, S., Winkler, A., and Roeckner, E.: Developments in the MPI-M Earth System Model version 1.2 (MPI-ESM1.2) and Its Response to Increasing CO2, Journal of Advances in Modeling Earth Systems, 11, 998–1038, https://doi.org/10.1029/2018MS001400, 2019.

McCartney, M. S.: A Voyage of Discovery: George Deacon 70th Anniversary Volume, chap. Subantarctic Mode Water, pp. 103–119, Supplement to Deep-Sea Research, Pergamon Press, Oxford, 1977.

McCartney, M. S. and Mauritzen, C.: On the origin of the warm inflow to the Nordic Seas, Prog. Oceanogr., 51, 125–214, https://doi.org/10.1016/S0079-6611(01)00084-2, 2001.

McWilliams, J. C., Sullivan, P. P., and Moeng, C.-H.: Langmuir turbulence in the ocean, J. Fluid Mech., 334, 1–30, https://doi.org/10.1017/S0022112096004375, 1997.

Mellor, G. and Yamada, T.: Development of a turbulent closure model for geophysical fluid problems, Rev. Geophys., 20, 851–875, https://doi.org/10.1029/RG020i004p00851, 1982.

865   Milinski, S., Bader, J., Haak, H., Siongco, A. C., and Jungclaus, J. H.: High atmospheric horizontal resolution eliminates the wind-driven
          coastal warm bias in the southeastern tropical Atlantic, Geophys. Res. Lett., 43, 10455–10462, https://doi.org/10.1002/2016GL070530,
          2016GL070530, 2016.

        Muilwijk, M., Ilicak, M., Cornish, S. B., Danilov, S., Gelderloos, R., Gerdes, R., Haid, V., Haine, T. W. N., Johnson, H. L., Kostov,
          Y., Kovács, T., Lique, C., Marson, J. M., Myers, P. G., Scott, J., Smedsrud, L. H., Talandier, C., and Wang, Q.: Arctic Ocean Re-
870   sponse to Greenland Sea Wind Anomalies in a Suite of Model Simulations, Journal of Geophysical Research: Oceans, 124, 6286–6322,
          https://doi.org/10.1029/2019JC015101, 2019.

        Müller, W. A., Jungclaus, J. H., Mauritsen, T., Baehr, J., Bittner, M., Budich, R., Bunzel, F., Esch, M., Ghosh, R., Haak, H., Ilyina, T.,
          Kleine, T., Kornblueh, L., Li, H., Modali, K., Notz, D., Pohlmann, H., Roeckner, E., Stemmler, I., Tian, F., and Marotzke, J.: A higher-
          resolution version of the Max Planck Institute Earth System Model (MPI-ESM 1.2-HR), J. Adv. Model. Earth Syst., 10, 1383–1413,
875   https://doi.org/10.1029/2017MS001217, 2018.

        Naughten, K., Meissner, K. J., Galton-Fenzi, B. K., England, M. H., Timmermann, R., Hellmer, H. H., Hattermann, T., and Debernard, J. B.:
          Intercomparison of Antarctic ice-shelf, ocean, and sea-ice interactions simulated by MetROMS-iceshelf and FESOM 1.4, Geosci. Model.
          Dev., 11, 1257–1292, https://doi.org/10.5194/gmd-11-1257-2018, 2018.

        Nielsen, S. B., Jochum, M., Eden, C., and Nuterman, R.: An energetically consistent vertical mixing parameterization in CCSM4, Ocean
880   Model., 127, 46–54, https://doi.org/10.1016/j.ocemod.2018.03.002, 2018.

        Nielsen, S. B., Jochum, M., Pedro, J. B., Eden, C., and Nuterman, R.: Two-Timescale Carbon Cycly Response to an AMOC Collapse,
          Paleoceanography and Paleoclimatology, 34 (4), 511–523, https://doi.org/10.1029/2018PA003481, 2019.

        Notz, D., Haumann, F. A., Haak, H., Jungclaus, J. H., and Marotzke, J.: Arctic sea-ice evolution as modeled by Max Planck Institute for
          Meteorology's Earth system model, J. Adv. Model. Earth Syst., 5, 173–194, https://doi.org/10.1002/jame.20016, 2013.

885   Olbers, D. and Eden, C.: A Global Model for the Diapycnal Diffusivity Induced by Internal Gravity Waves, J. Phys. Oceanogr., 43, 1759–
          1779, https://doi.org/10.1175/JPO-D-12-0207.1, 2013.

        Orsi, A. H., Nowlin Jr., W. D., and Whitworth III, T.: On the circulation and stratification of the Weddell Gyre, Deep-Sea Res., 40, 169–203,
          https://doi.org/10.1016/0967-0637(93)90060-G, 1993.

        Pacanowski, R. C. and Philander, S. G. H.: Parameterization of Vertical Mixing in Numerical Models of Tropical Oceans, J. Phys. Oceanogr.,
890   11, 1443–1451, https://doi.org/10.1175/1520-0485(1981)011<1443:POVMIN>2.0.CO;2, 1981.

        Pickart, R. S., Spall, M. A., Ribergaard, M. H., Moore, G. W. K., and Milliff, R. F.: Deep convection in the Irminger Sea forced by the
          Greenland tip jet, Nature, 424, 152–156, https://doi.org/10.1038/nature01729, 2003.

        Pollmann, F., Eden, C., and Olbers, D.: Evaluating the Global Internal Wave Model IDEMIX Using Finestructure Methods, J. Phys.
          Oceanogr., 47, 2267–2289, https://doi.org/10.1175/JPO-D-16-0204.1, 2017.

895   Putrasahan, D. A., Lohmann, K., von Storch, J. S., Jungclaus, J. H., Haak, H., and Gutjahr, O.: Surface flux drivers for the slowdown
          of the Atlantic Meridional Overturning Circulation in a high-resolution global coupled climate model, J. Adv. Model. Earth Syst., 11,
          1349–1363, https://doi.org/10.1029/2018MS001447, 2019.

        Rainville, L. and Winsor, P.: Mixing across the Arctic Ocean: Microstructure observations during the Beringia 2005 Expedition, Geophys.
          Res. Lett., 35, L08606, https://doi.org/10.1029/2008GL033532, 2008.

900   Rainville, L. and Woodgate, R.: Observations of internal wave generation in the seasonally ice-free Arctic, Geophys. Res. Lett., 36, L23604,
          https://doi.org/10.1029/2009GL041291, 2009.

Randall, D. A., Wood, R. A., Bony, S., Colman, R., Fichefet, T., Fyfe, J., Kattsov, V., Pitman, A., Shukla, J., Srinivasan, J., Stouffer, R. J., Sumi, A., and Taylor, K. E.: Climate Change 2007: The Physical Science Basis. Contribution of Workung Group I to the Fourth Assessment Report of the Intergovernmental Panel on Climate Change, chap. Climate Models and Their Evaluation, Cambridge University

905   Press, Cambrigdge, United Kingdom and New York, NY, USA, 2007.

Redi, M. H.: Oceanic Isopycnal Mixing by Coordinate Rotation, Journal of Physical Oceanography, 12, 1154–1158, https://doi.org/10.1175/1520-0485(1982)012<1154:OIMBCR>2.0.CO;2, 1982.

Reid, J. L.: On the contribution of the Mediterranean Sea outflow to the Norwegian-Greenland Sea, Deep-Sea Res., 26A, 1199–1223, https://doi.org/10.1016/0198-0149(79)90064-5, 1979.

910   Rimac, A., von Storch, J.-S., Eden, C., and Haak, H.: The influence of high-resolution wind stress field on the power input to near-inertial motions in the ocean, Geophys. Res. Lett., 40, 4882–4886, https://doi.org/10.1002/grl.50929, 2013.

Rippeth, T. P., Lincoln, B. J., Lenn, Y.-D., Green, J. A. M., Sundfjord, A., and Bacon, S.: Tide-mediated warming of Arctic halocline by Atlantic heat fluxes over rough topography, Nat. Geosci., 8, 191–194, https://doi.org/10.1038/ngeo2350, 2015.

Rippeth, T. P., Vlasenko, V., Stashchuk, N., Scanell, B. D., Green, J. A. M., Lincoln, B. J., and Bacon, S.: Tidal conversion and mixing

915   poleward of the critical latitude (an Arctic case study), Geophys. Res. Lett., 44, 12 349–12 357, https://doi.org/10.1002/2017GL075310, 2017.

Robertson, R. and Dong, C.: An evaluation of the performance of vertical mixing parameterizations for tidal mixing in the Regional Ocean Model System (ROMS), Geosci. Lett., 6, 1–18, https://doi.org/10.1186/s40562-019-0146-y, 2019.

Rossby, T. and Flagg, C. N.: Direct measurments of volume flux in the Faroe-Shetland Channel and over the Iceland-Faroe Ridge, Geophys.

920   Res. Lett., 39, L07 602, https://doi.org/10.1029/2012GL051269, 2012.

Rudels, B., Jones, E. P., Anderson, L. G., and Kattner, G.: The polar oceans and their role in shaping the global environment, vol. 85 of *Geophysics Monogr. Ser.*, chap. On the intermediate depth waters of the Arctic Ocean, pp. 33–46, American Geophysical Union, Washington, D. C., 1994.

Rudels, B., Friedrich, H. J., and Quadfasel, D.: The Arctic Circumpolar Boundary Current, Deep Sea Res. II, 46, 1023–1062,

925   https://doi.org/10.1016/S0967-0645(99)00015-6, 1999.

Rudels, B., Korhonen, M., Schauer, U., Pisarev, S., Raabe, B., and Wisotzki, A.: Circulation and transformation of Atlantic water in the Eurasian Basin and the contribution of the Fram Strait inflow branch to the Arctic Ocean heat budget, Progress in Oceanography, 132, 128–152, https://doi.org/10.1016/j.pocean.2014.04.003, 2015.

Sabine, C. L., Freely, R. A., Gruber, N., Key, R. M., Lee, K., and Bullister, J. L.: The oceanic sink for anthropogenic CO_2, Science, 305

930   (5682), 367–371, https://doi.org/10.1126/science.1097403, 2004.

Sallée, J.-B., Shuckburgh, E., Bruneau, N., Meijers, A. J. S., Bracegirdle, T. J., and Wang, Z.: Assessment of Southern Ocean mixed-layer depths in CMIP5 models: Historical bias and forcing response, J. Geophys. Res. Oceans, 118, 1845–1862, https://doi.org/10.1002/jgrc.20157, 2013.

Sarmiento, J., Gruber, N., Brzezinksi, M., and Dunne, J.: High-latitude controls of thermocline nutrients and low latitude biological produc-

935   tivity, Nature, 427, 56–60, https://doi.org/10.1038/nature02127, 2004.

Sayol, J.-M., Dijkstra, H., and Katsman, C.: Seasonal and regional variations of sinking in the subpolar North Atlantic from a high-resolution ocean model, Ocean Sci., 15, 1033–1053, https://doi.org/10.5194/os-15-1033-2019, 2019.

Schweiger, A., Lindsay, R., Zhang, J., Steele, M., Stern, H., and Kwok, R.: Uncertainty in modelled Arctic sea ice volume, J. Geophys. Res. Oceans, 116, D06, https://doi.org/10.1029/2011JC007084, 2011.

940   Sein, D. V., Koldunov, N. V., Danilov, S., Sidorenko, D., Wekerle, C., Cabos, W., Rackow, T., Scholz, P., Semmler, T., Wang, Q., and Jung, T.: The relative influence of atmospheric and oceanic model resolution on the circulation of the North Atlantic Ocean in a coupled climate model, J. Adv. Model. Earth Syst., 10, 2026–2041, https://doi.org/10.1029/2018MS001327, 2018.

Shu, Q., Wang, Q., Su, J., Li, X., and Fangli, Q.: Assessment of the Atlantic water layer in the Arctic Ocean in CMIP5 climate models, Clim. Dyn., 53(9), 5279–5291, https://doi.org/10.1007/s00382-019-04870-6, 2019.

945   Simmons, H. L., Jayne, S. R., St. Laurant, L. C., and Weaver, A. J.: Tidally driven mixing in a numerical model of the ocean general circulation, Ocean Modelling, 6, 245–263, https://doi.org/10.1016/S1463-5003(03)00011-8, 2004.

Sloyan, B. and Rintoul, S.: Circulation, renewel, and modification of Antarctic mode and intermediate water, J. Phys. Oceanogr., 31, 1005–1030, https://doi.org/10.1175/1520-0485(2001)031<1005:CRAMOA>2.0.CO;2, 2001.

Stevens, B., Giorgetta, M., Esch, M., Mauritsen, T., Crueger, T., Rast, S., Salzmann, M., Schmidt, H., Bader, J., Block, K., Brokopf, R.,
950   Fast, I., Kinne, S., Kornblueh, L., Lohmann, U., Pincus, R., Reichler, T., and Roeckner, E.: Atmospheric component of the MPI-M Earth System Model: ECHAM6, J. Adv. Model. Earth Syst., 5, 146–172, https://doi.org/10.1002/jame.20015, 2013.

Stössel, A., Notz, D., Haumann, F. A., Haak, H., Jungclaus, J., and Mikolajewicz, U.: Controlling high-latitude Southern Ocean convection in climate models, Ocean Model., 86, 58–75, https://doi.org/10.1016/j.ocemod.2014.11.008, 2015.

Timmermann, R. and Beckmann, A.: Parameterization of vertical mixing in the Weddell Sea, Ocean Model., 6, 83–100,
955   https://doi.org/10.1016/S1463-5003(02)00061-6, 2004.

Våge, K., Pickart, R., Sarafanov, A., Knutsen, Ø., Mercier, H., Lherminier, P., van Aken, H. M., Meincke, J., Quadfasel, D., and Bacon, S.: The Irminger Gyre: circulation, convection, and interannual veriability, Deep-Sea Res. I, 58, 590–614, https://doi.org/10.1016/j.dsr.2011.03.001, 2011.

Valcke, S.: The OASIS3 coupler: a European climate modelling community software, Geosci. Model. Dev., 6, 373–388,
960   https://doi.org/10.5194/gmd-6-373-2013, 2013.

Van Roekel, L., Adcroft, A. J., Danabasoglu, G., Griffies, S. M., Kauffman, B., Large, W., Levy, M., Reichl, B. G., Ringler, T., and Schmidt, M.: The KPP Boundary Layer Scheme for the Ocean: Revisiting Its Formulation and Benchmarking One-Dimensional Simulations Relative to LES, Adv. Model. Earth Syst., 10, 2647–2685, https://doi.org/10.1029/2018MS001336, 2018.

von Appen, W.-J., Schauer, U., Hattermann, T., and Beszczynska-Möller, A.: Seasonal cycle of mesoscale instability of the West Spitsbergen
965   Current, J. Phys. Oceanogr., 46, 1231–1254, https://doi.org/10.1175/JPO-D-15-0184.1, 2016.

Wang, Q., Danilov, S., Sidorenko, D., Timmermann, R., Wekerle, C., Wang, X., Jung, T., and Schröter, J.: The Finite Element Sea Ice-Ocean Model FESOM v.1.4: formulation of an ocean general circulation model, Geosci. Model. Dev., 7, 663–693, https://doi.org/10.5194/gmd-7-663-2014, 2014.

Wang, Q., Wekerle, C., Danilov, S., Wang, X., and Jung, T.: A 4.5 km resolution Arctic Ocean simulation with the global multi-resolution
970   model FESOM1.4, Geosci. Model Dev., 11, 1229–1255, https://doi.org/10.5194/gmd-11-1229-2018, 2018.

Wekerle, C., Wang, Q., von Appen, W.-J., Danilov, S., Schourup-Kristensen, V., and Jung, T.: Eddy-resolving simulation of the Atlantic Water circulation in the Fram Strait with focus on the seasonal cycle, J. Geophys. Res. Oceans, 122, 8385–8405, https://doi.org/10.1002/2017JC012974, 2017.

Wolff, J. O., Maier-Reimer, E., and Legutke, S.: The Hamburg Ocean Primitive Equation Model HOPE, Tech. Rep. 13, German Climate
975   Computer Center (DKRZ), 1997.

Yu, L.-S., Bosse, A., Fer, I., Orvik, K. A., Bruvik, E. M., Hessevik, I., and Kvalsund, K.: The Lofoten Basin eddy: Three years of evolution as observed by Seagliders, J. Geophys. Res. Oceans, 122, 6814–6834, https://doi.org/10.1002/2017JC012982, 2017.

Zhang, J. and Rothrock, D. A.: Modeling Global Sea Ice with a Thickness and Enthalpy Distribution Model in Generalized Curvilinear Coordinates, Mon. Weather Rev., 131, 845–861, https://doi.org/10.1175/1520-0493(2003)131<0845:MGSIWA>2.0.CO;2, 2003.

980   Zhang, J. and Steele, M.: Effect of vertical mixing on the Atlantic Water layer circulation in the Arctic Ocean, Geophys. Res. Oceans, 112, C04S04, https://doi.org/10.1029/2006JC003732, 2007.

Zhao, M., Timmermanns, M.-L., Cole, S., Krishfield, R., Proshutinsky, A., and Toole, J.: Characterizing the eddy field in the Arctic Ocean halocline, J. Geophys. Res. Oceans., 119, 8800–8817, https://doi.org/10.1002/2014JC010488, 2014.

Table 1. Overview of the 100 year long control simulations conducted with MPI-ESM1.2-HR. All simulations use a T127 (about 100 km) resolution in the atmosphere and a resolution of $0.4\,°$ (about 40 km) on a tripolar grid (TP04) in the ocean. The number of vertical levels are 95 in the atmosphere and 40 in the ocean, respectively. All models were analysed for the model years 80–100.

Experiment	Ocean mixing scheme	Description	Reference
HR_{pp}	PP	reference simulation	(Pacanowski and Philander, 1981)
HR_{kpp}	KPP	uses PP scheme below mixed layer	(Large et al., 1994; Griffies et al., 2015)
HR_{tke}	TKE	background diffusivity $K = \sqrt{2}E_{min}/N$ with $E_{min} = 10^{-6}\,\mathrm{m^2 s^{-2}}$	(Gaspar et al., 1990)
HR_{ide}	TKE + IDEMIX	$E_{min} = 0\,\mathrm{m^2 s^{-2}}$; prognostic simulation of internal gravity waves	(Eden et al., 2014)

Table 2. Time-averaged volume transport ($1\,\mathrm{Sv} = 10^6\,\mathrm{m^3\,s^{-1}}$) of Denmark Strait Overflow Water (DSOW), Faroe Bank Channel (FBC) and Faroe-Shetland Channel (FSC) overflow from simulations with MPI-ESM1.2-HR. Hansen et al. (2017) note that measurements by Rossby and Flagg (2012) and Childers et al. (2014) include a closed circulation on the Faroe Shelf (0.6 Sv) and flow on the Scottish Shelf, which are not included in measurements by Berx et al. (2013) and Hansen et al. (2015). A standard deviation based on annual averages is given for the simulations.

Observations/Experiment	DSOW	FBC	FSC
Jochumsen et al. (2017)	-3.2 ± 0.5	-	-
Jochumsen et al. (2012)	-3.4	-	-
Hansen et al. (2016)	-	2.2	-
Berx et al. (2013); Hansen et al. (2015)	-	-	2.7
Rossby and Flagg (2012)	-	-	0.9
Childers et al. (2014)	-	-	1.5
$\mathrm{HR_{pp}}$	-1.8 ± 0.2	1.8 ± 0.1	3.2 ± 0.4
$\mathrm{HR_{kpp}}$	-2.1 ± 0.4	1.8 ± 0.2	3.3 ± 0.3
$\mathrm{HR_{tke}}$	-2.2 ± 0.3	1.9 ± 0.1	3.5 ± 0.2
$\mathrm{HR_{ide}}$	-2.1 ± 0.3	1.7 ± 0.1	3.3 ± 0.3

Table 3. Time-averaged volume transport ($1\,\mathrm{Sv} = 10^6\,\mathrm{m}^3\,\mathrm{s}^{-1}$) of the Antarctic Circumpolar Current (ACC) through Drake Passage from observations and simulations with MPI-ESM1.2-HR.

Experiment	Mean	Standard deviation
Donohue et al. (2016)	173.3±10.7	-
HR_{pp}	161.41	2.14
HR_{kpp}	191.97	2.99
HR_{tke}	174.31	2.63
HR_{ide}	163.54	4.39
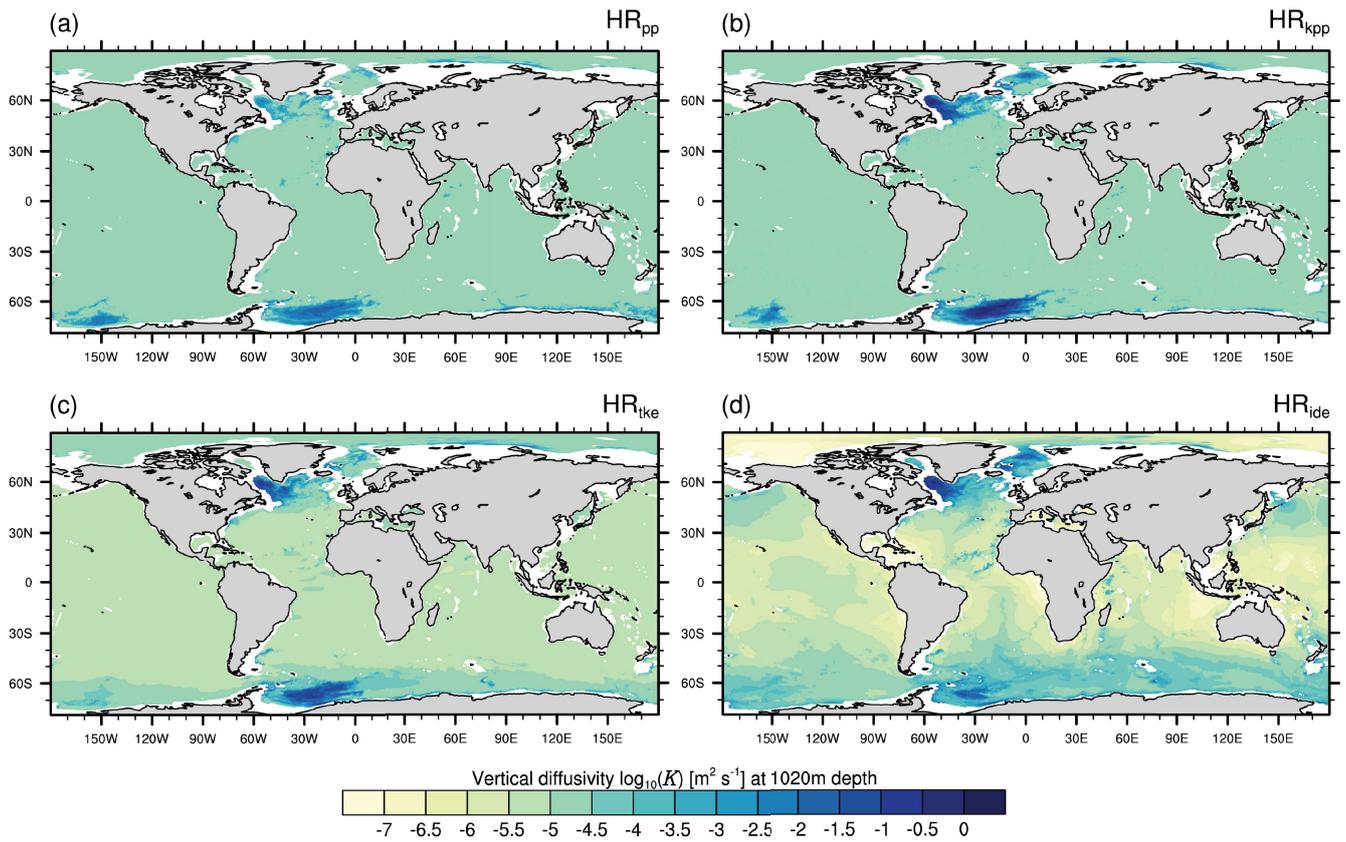
Figure 1. Time-averaged vertical diffusivity $\log_{10}(K)$ $(\mathrm{m^2\,s^{-1}})$ at a depth of $1020\,\mathrm{m}$ in the MPI-ESM1.2-HR simulations for (a) HR_{pp}, (b) HR_{kpp}, (c) HR_{tke}, and (d) HR_{ide}.
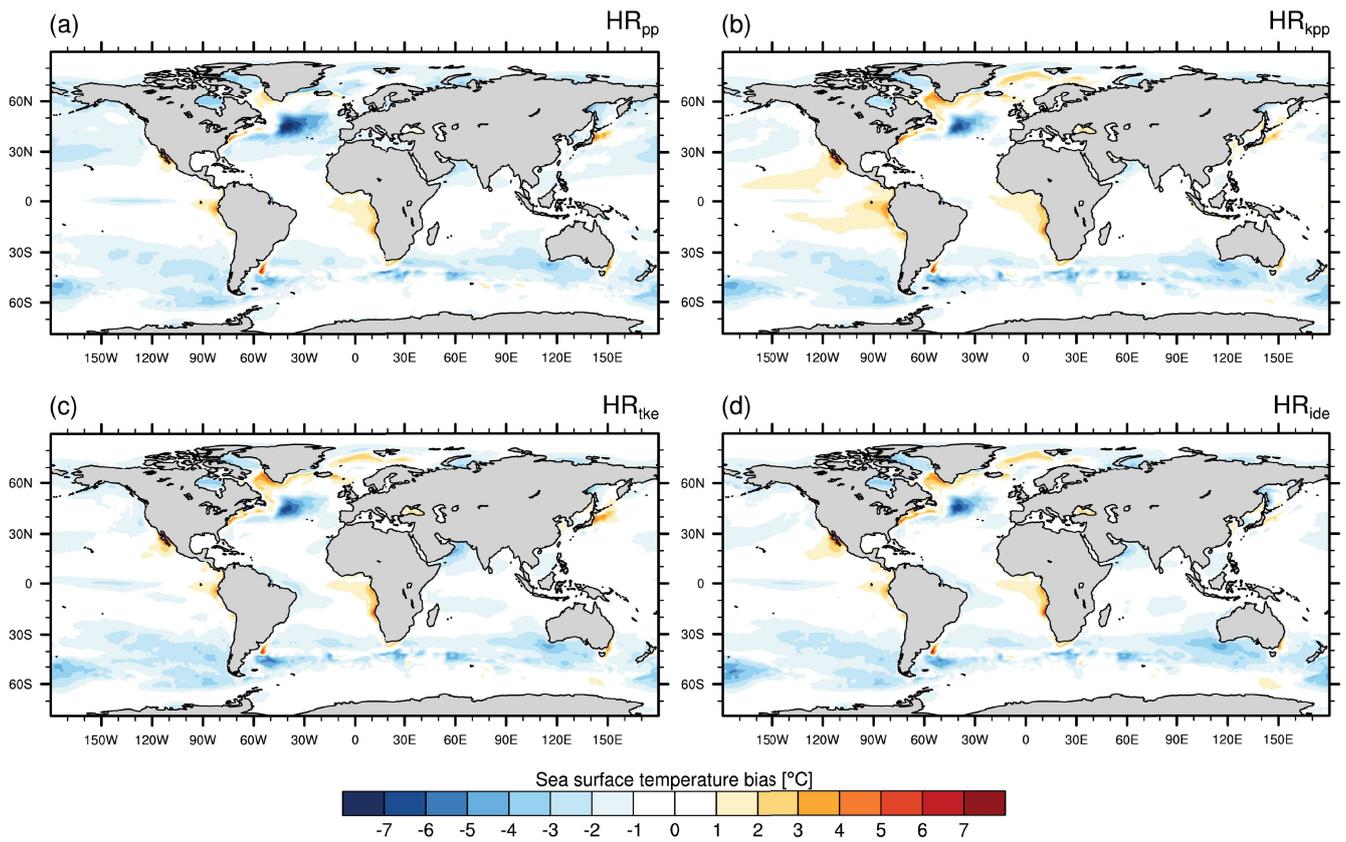
Figure 2. Time-averaged sea surface temperature bias of MPI-ESM1.2-HR minus EN4 (1945-1955) for (a) HR_{pp}, (b) HR_{kpp}, (c) HR_{tke}, and (d) HR_{ide}.
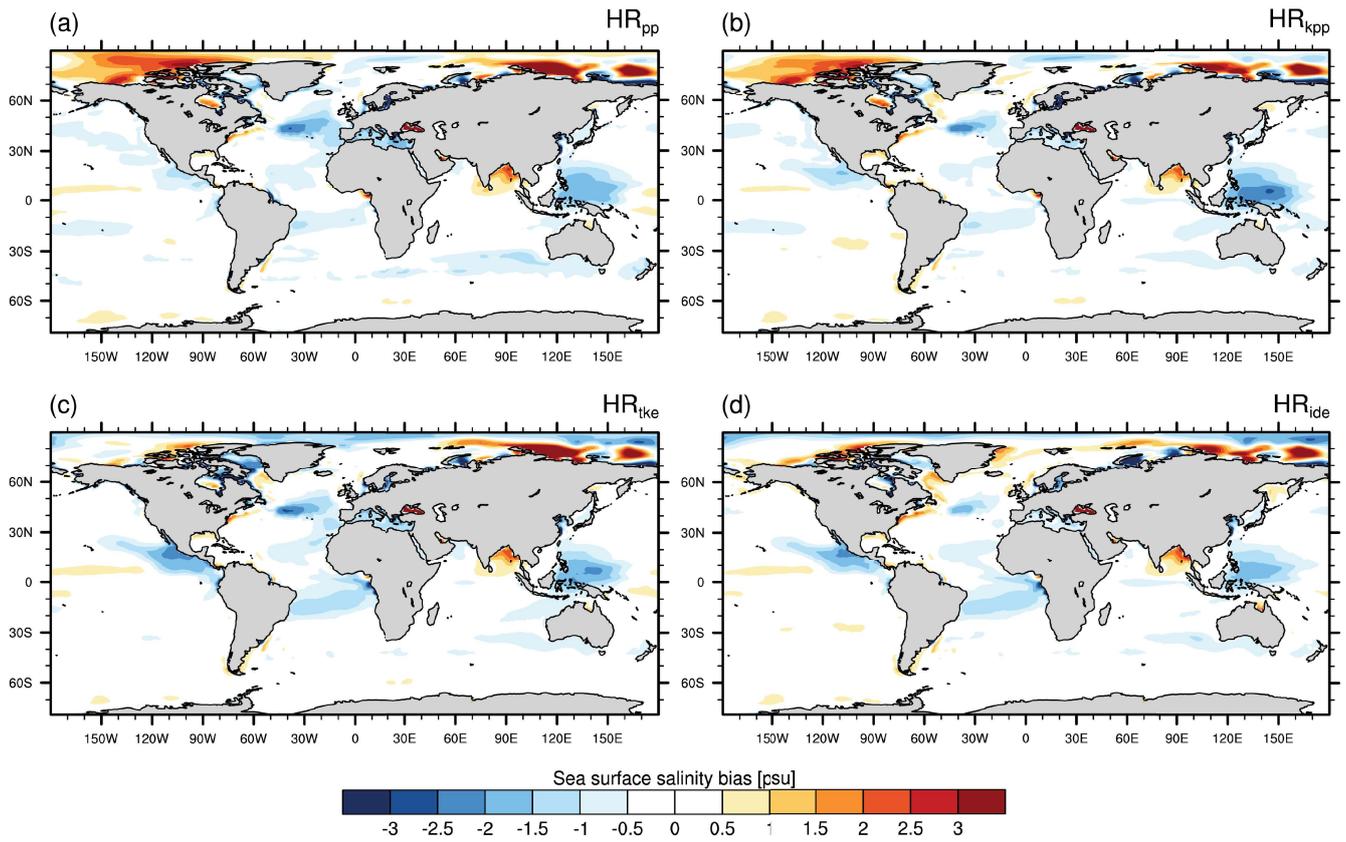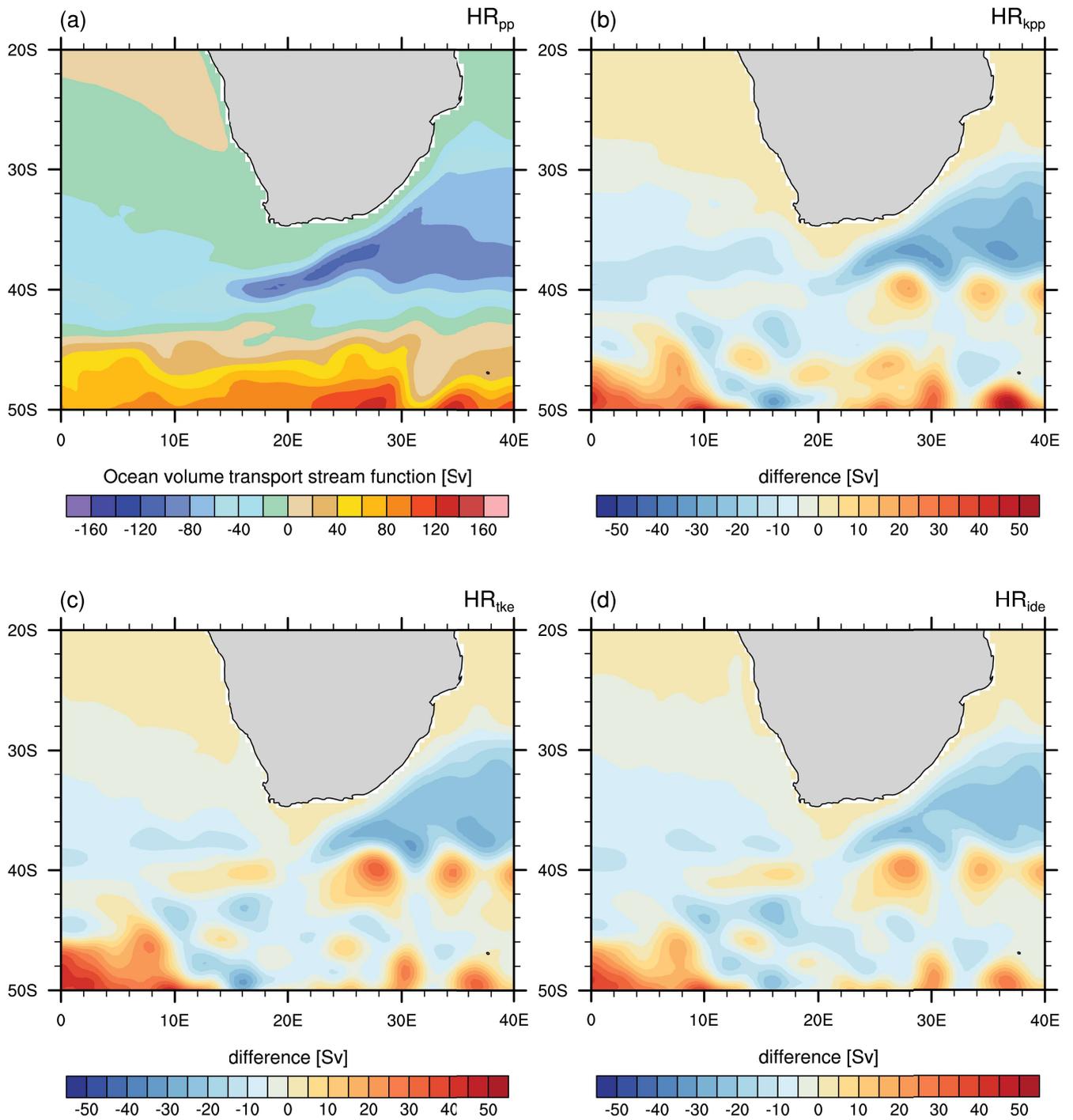
Figure 3. Time-averaged sea surface salinity bias of MPI-ESM1.2-HR minus EN4 (1945-1955) for (a) HR$_{pp}$, (b) HR$_{kpp}$, (c) HR$_{tke}$, and (d) HR$_{ide}$.
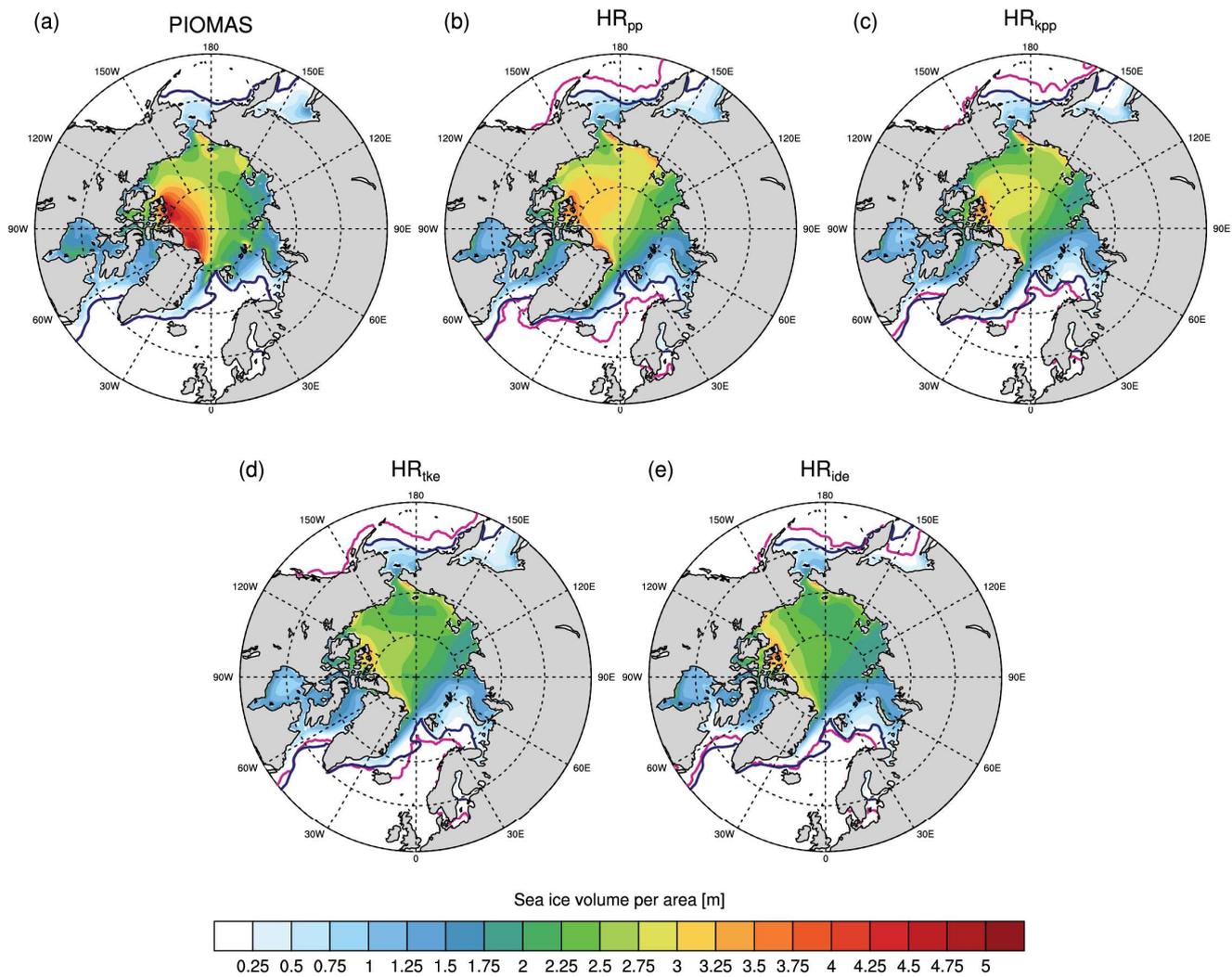
Figure 4. Time-averaged [..²⁴³]Arctic sea ice thickness in March for (a) PIOMAS reanalysis (March 1979–2005; Zhang and Rothrock, 2003; Schweiger et al., 2011), (b) HR$_{pp}$, (c) HR$_{kpp}$, (d) HR$_{tke}$, (e) HR$_{ide}$. The 15 % sea ice concentration of [..²⁴⁴]the EUMETSAT OSI SAF ([..²⁴⁵]averaged over March 1979–2005) [..²⁴⁶]is contoured in dark blue and those of [..²⁴⁷]the simulations in magenta.
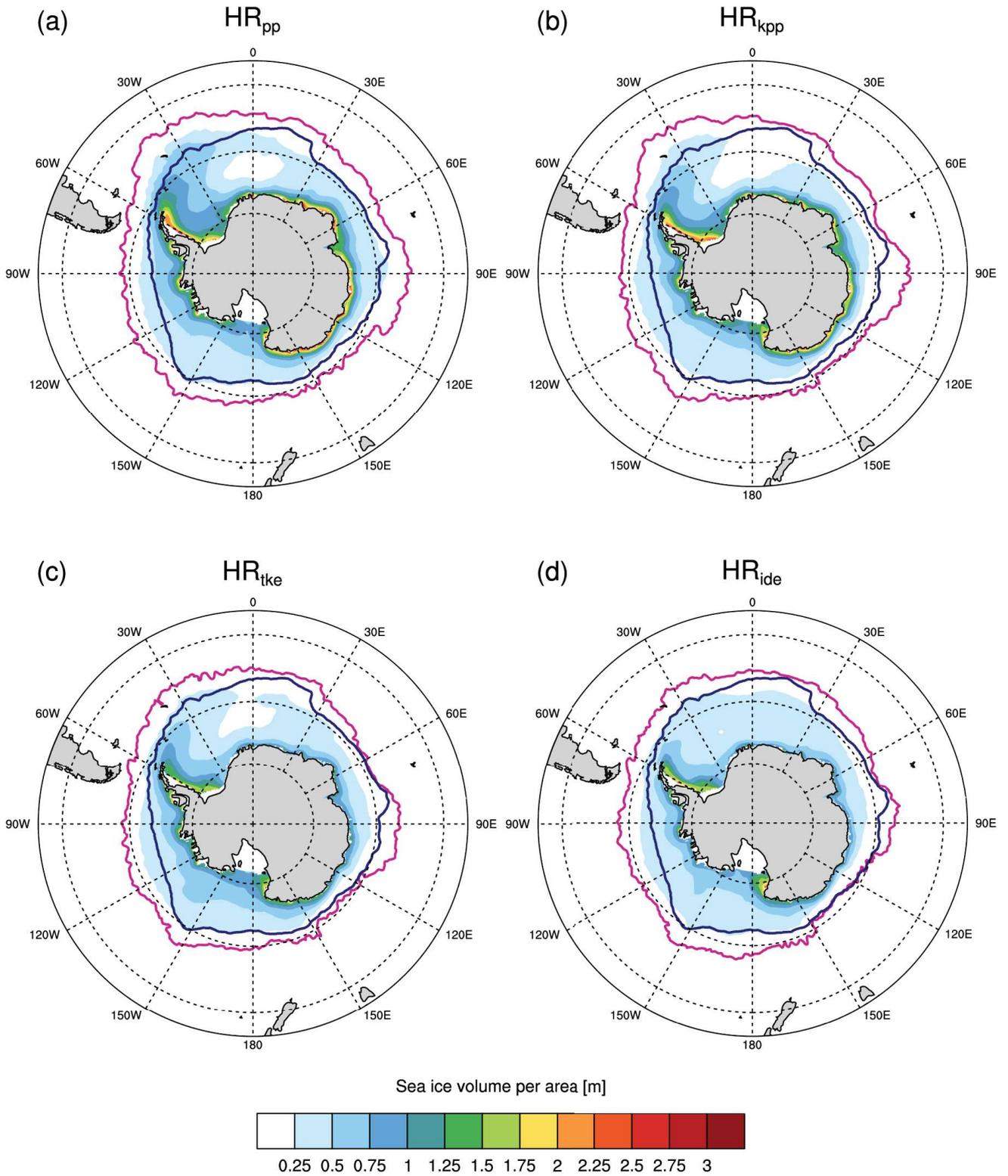
Figure 5. Time-averaged Arctic sea ice thickness in March for (a) HR_{pp}, (b) HR_{kpp}, (c) HR_{tke}, [..²⁴⁸](d) HR_{ide}. The 15 % sea ice concentration of the EUMETSAT OSI SAF (averaged over March 1979–2005) is contoured in dark blue and those of the simulations in magenta.
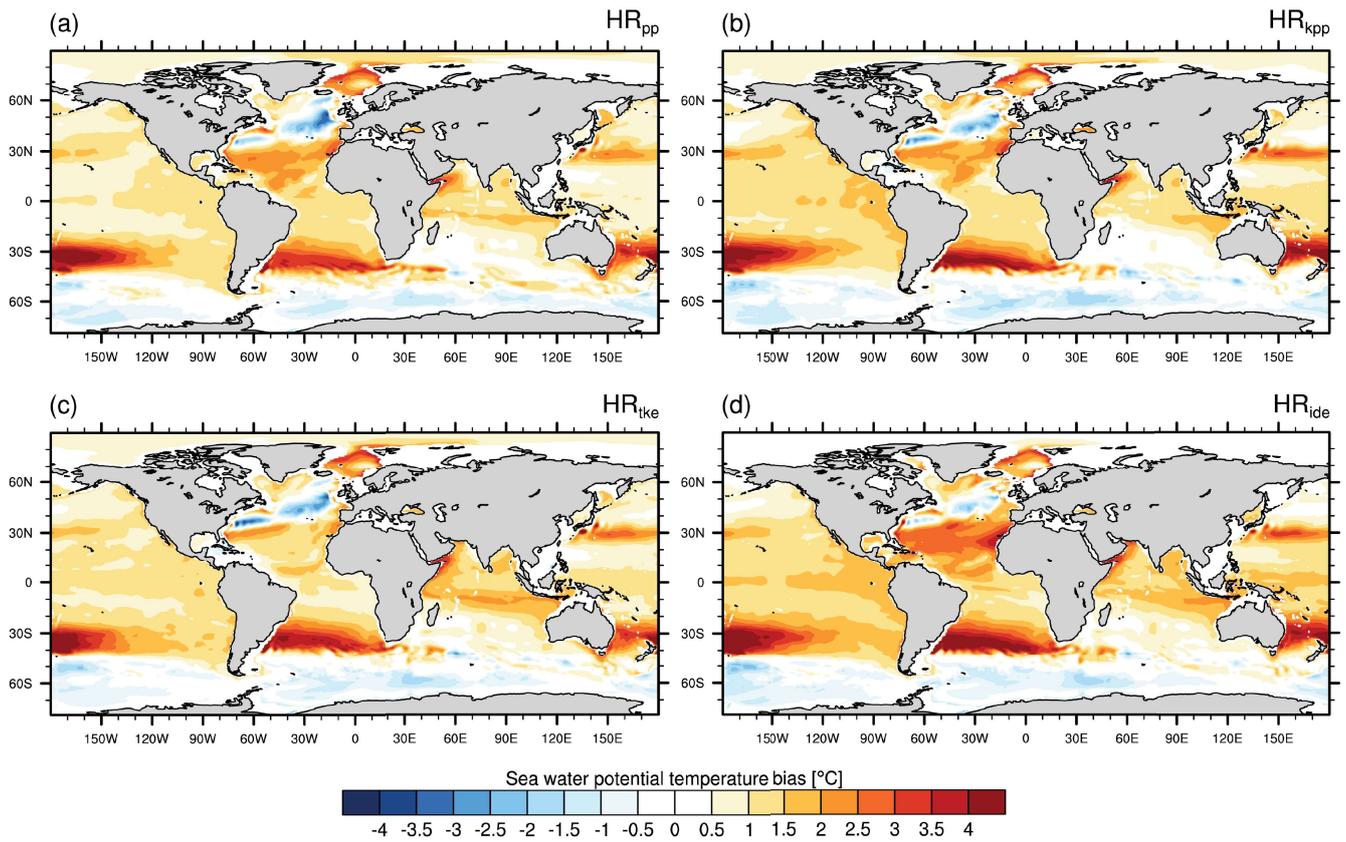
Figure 6. Time-averaged [..²⁴⁹]potential temperature bias of MPI-ESM1.2-HR minus EN4 (1945-1955) at a depth of 740 m for (a) HR$_{pp}$, (b) HR$_{kpp}$, (c) HR$_{tke}$, and (d) HR$_{ide}$.

Figure 7. [..²⁵⁰]Time-averaged volume transport in the Agulhas region south of Africa as simulated by MPI-ESM1.2 [..²⁵¹]([..²⁵²]a) [..²⁵³]HR$_{pp}$ and [..²⁵⁴]the difference ([..²⁵⁵]experiment minus HR$_{pp}$[..²⁵⁶]) for (b) HR$_{kpp}$, (c) HR$_{tke}$, and (d) HR$_{ide}$.
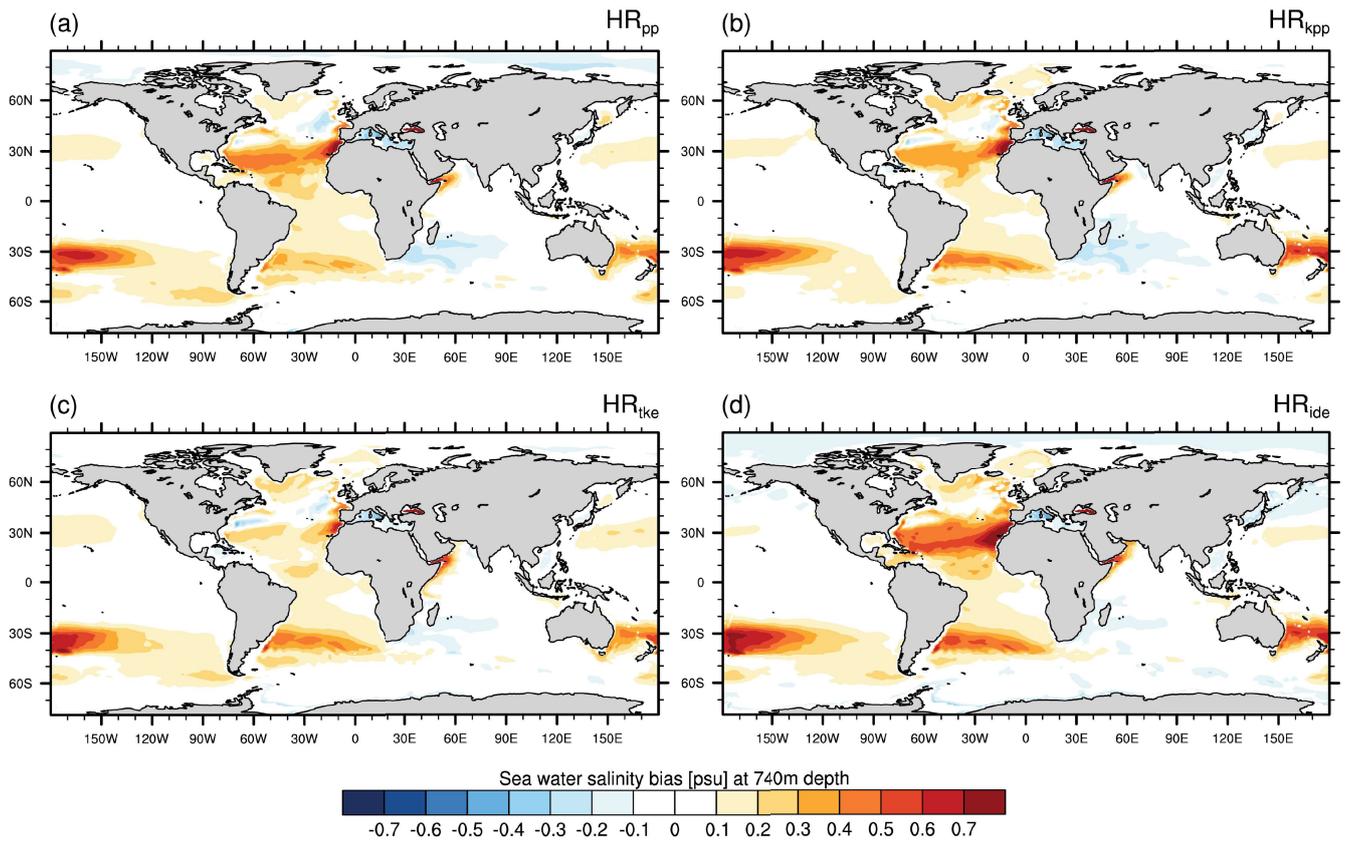
Figure 8. Time-averaged [..257]salinity bias of MPI-ESM1.2-HR minus EN4 (1945-1955) at a depth of [..258]740 m [..259]for (a) HRpp, (b) HRkpp, (c) HRtke, and (d) HRide.[..260]
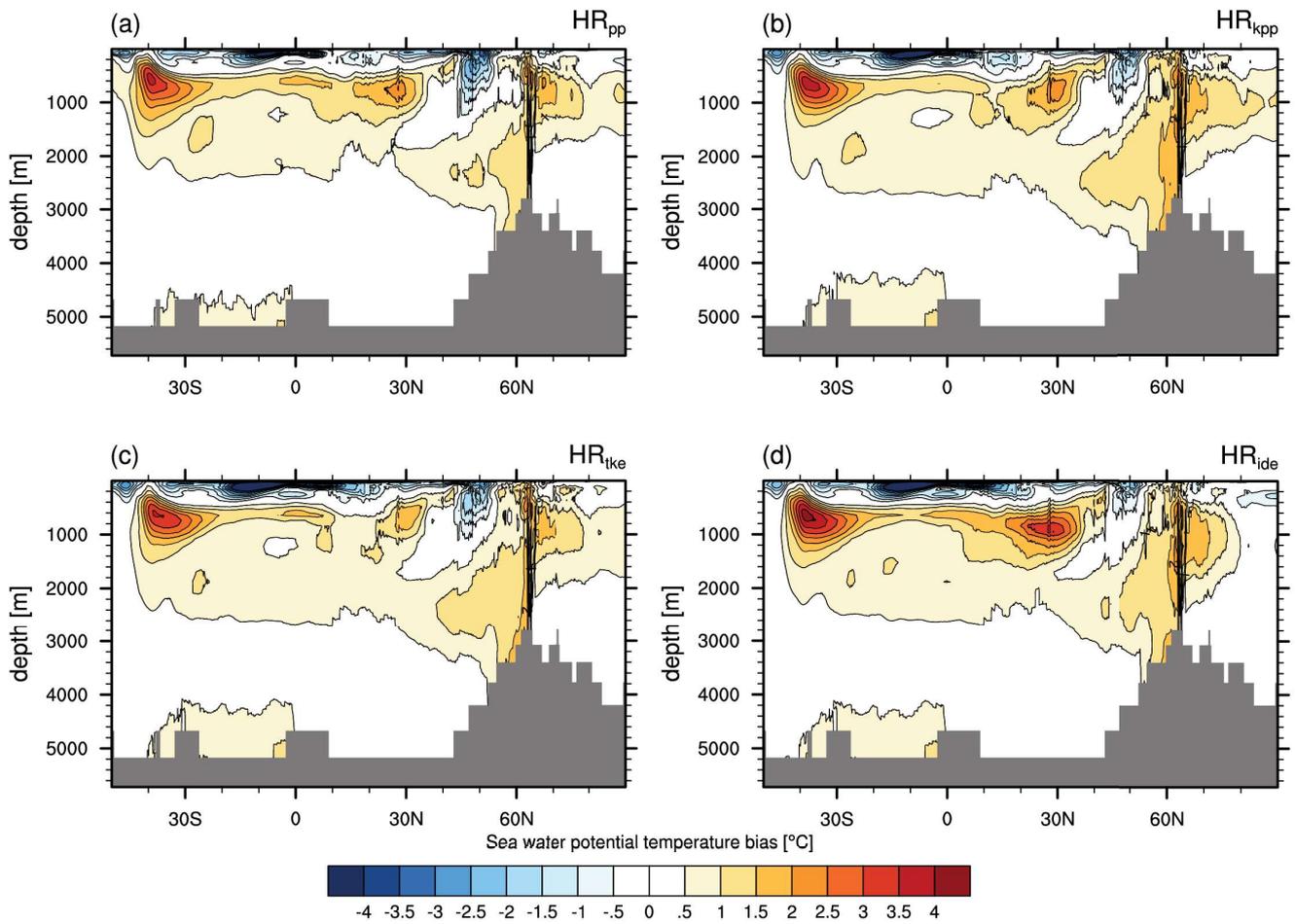
Figure 9. [..²⁶¹]Zonal-mean potential temperature bias of MPI-ESM1.2-HR minus EN4 (1945-1955) [..²⁶²]in the Atlantic and Arctic Ocean [..²⁶³]for (a) HR_{pp}, (b) HR_{kpp}, (c) HR_{tke}, and (d) HR_{ide}.
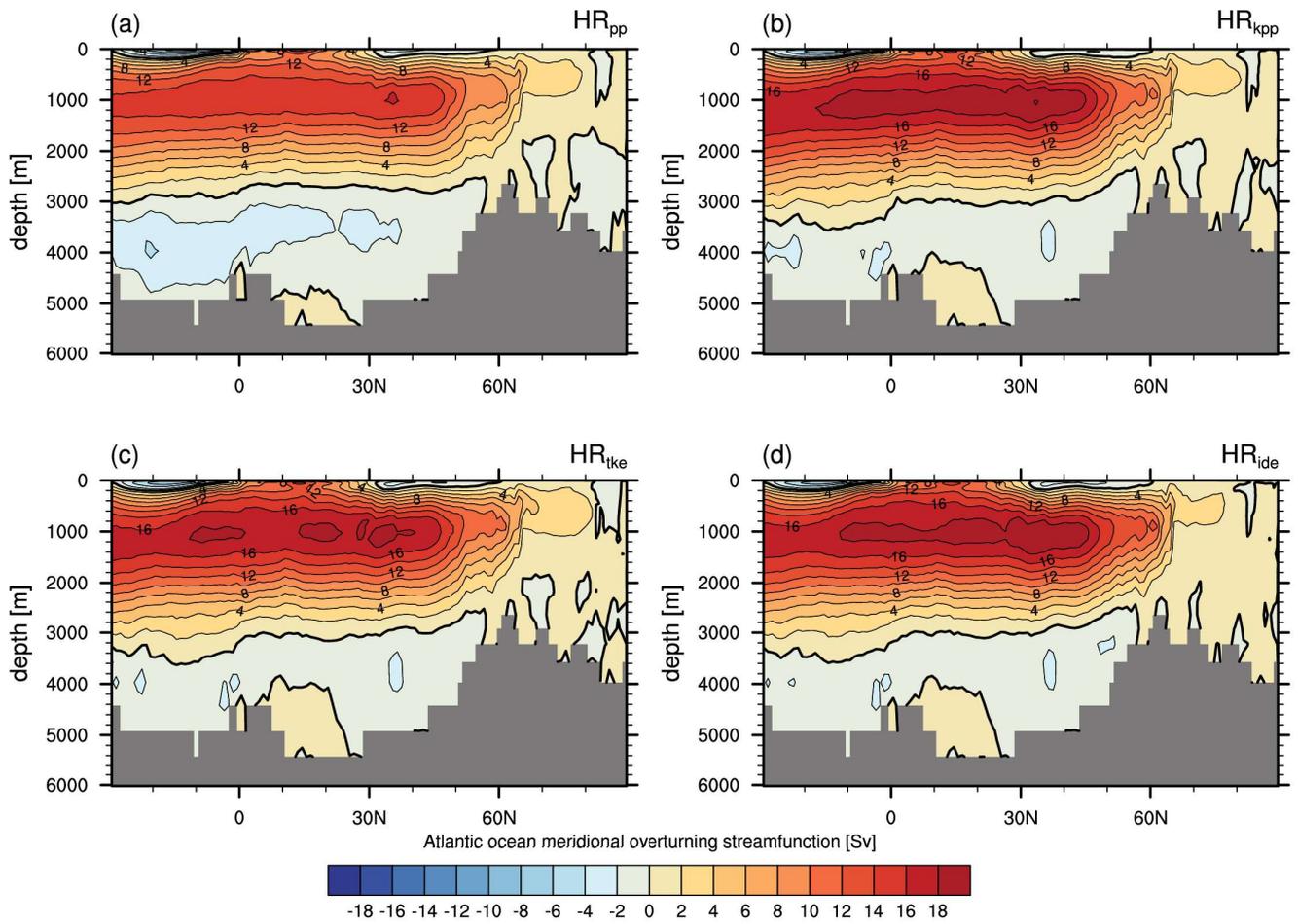
Figure 10. [..²⁶⁴]Eulerian stream function ([..²⁶⁵]$Sv = 10^6 \, m^3 \, s^{-1}$) [..²⁶⁶]of [..²⁶⁷]the [..²⁶⁸]AMOC in depth space simulated by MPI-ESM1.2 (a) HR_{pp}, (b) HR_{kpp}, (c) HR_{tke}, and (d) HR_{ide}.[..²⁶⁹]
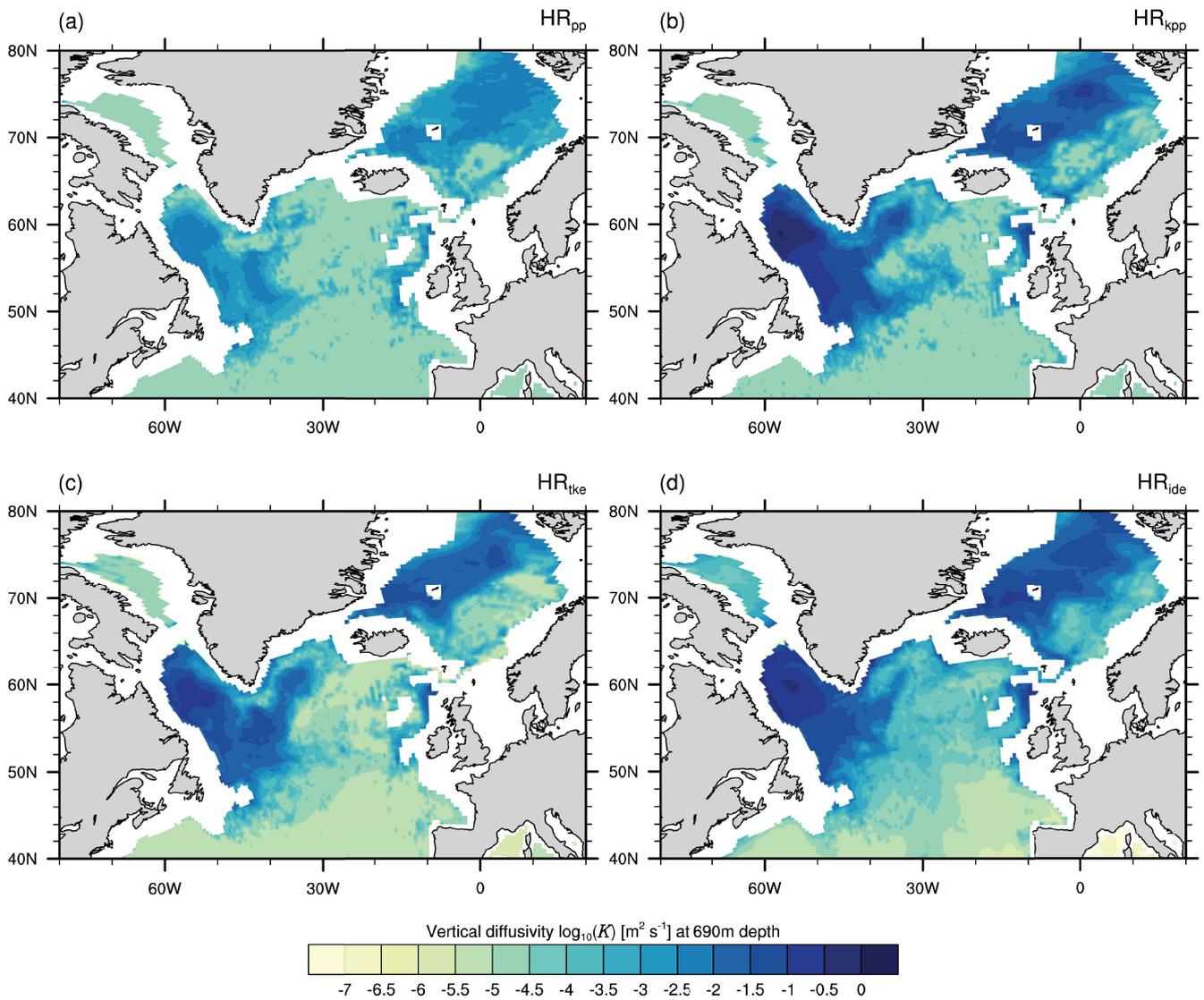
Figure 11. Time-averaged vertical diffusivity $\log_{10}(K)$ (m^2 s^{-1}) at a depth of 690 m in the subpolar North Atlantic simulated by MPI-ESM1.2 (a) HR$_{pp}$, (b) HR$_{kpp}$, (c) HR$_{tke}$, and (d) HR$_{ide}$.
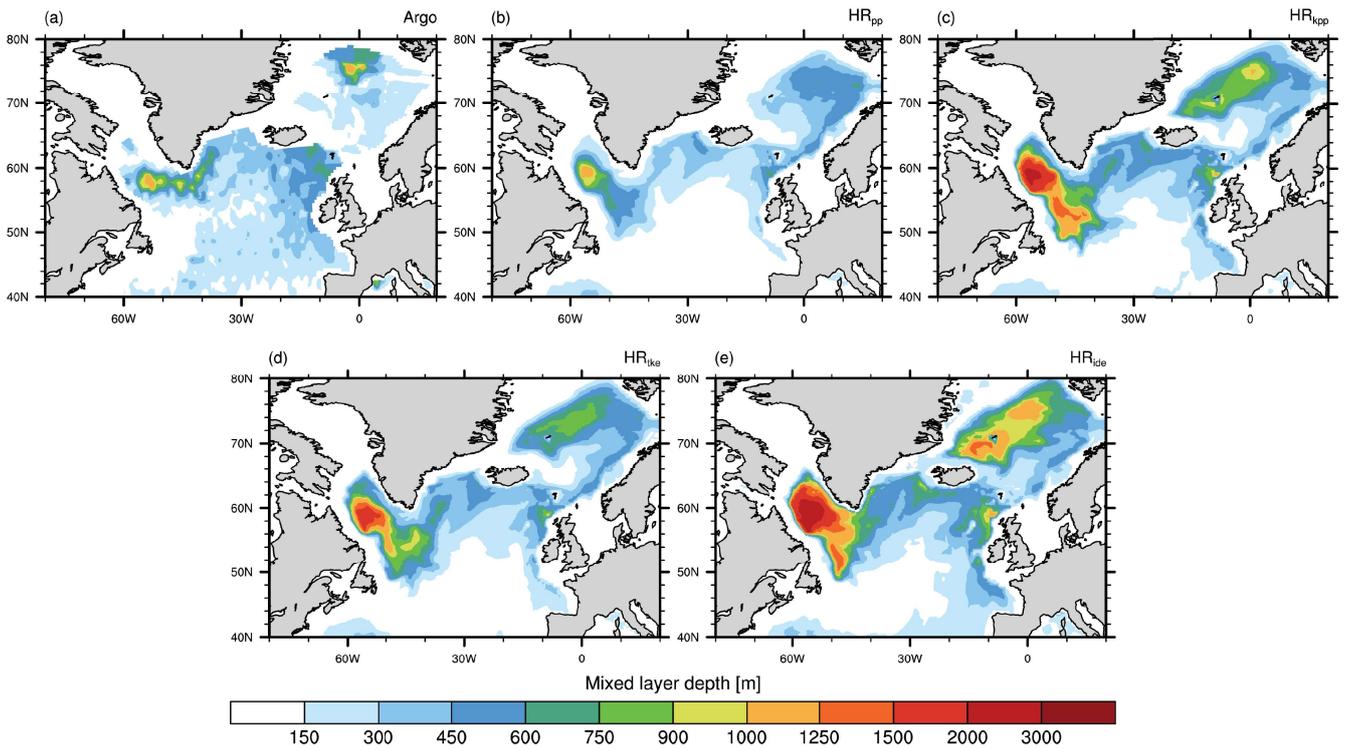
Figure 12. Time-averaged mixed layer depths (m) in March calculated by the density threshold method ($[..^{270}]\sigma_t = 0.03\,\mathrm{kg\,m^{-3}}$) from (a) $1° \times 1°$ Argo float data (Holte et al., 2017) (mean March from 2000 to 2018) $[..^{271}]$ and $[..^{272}]$ from MPI-ESM1.2 (b) $\mathrm{HR_{pp}}$, (c) $\mathrm{HR_{kpp}}$, (d) $\mathrm{HR_{tke}}$, and (e) $\mathrm{HR_{ide}}$.
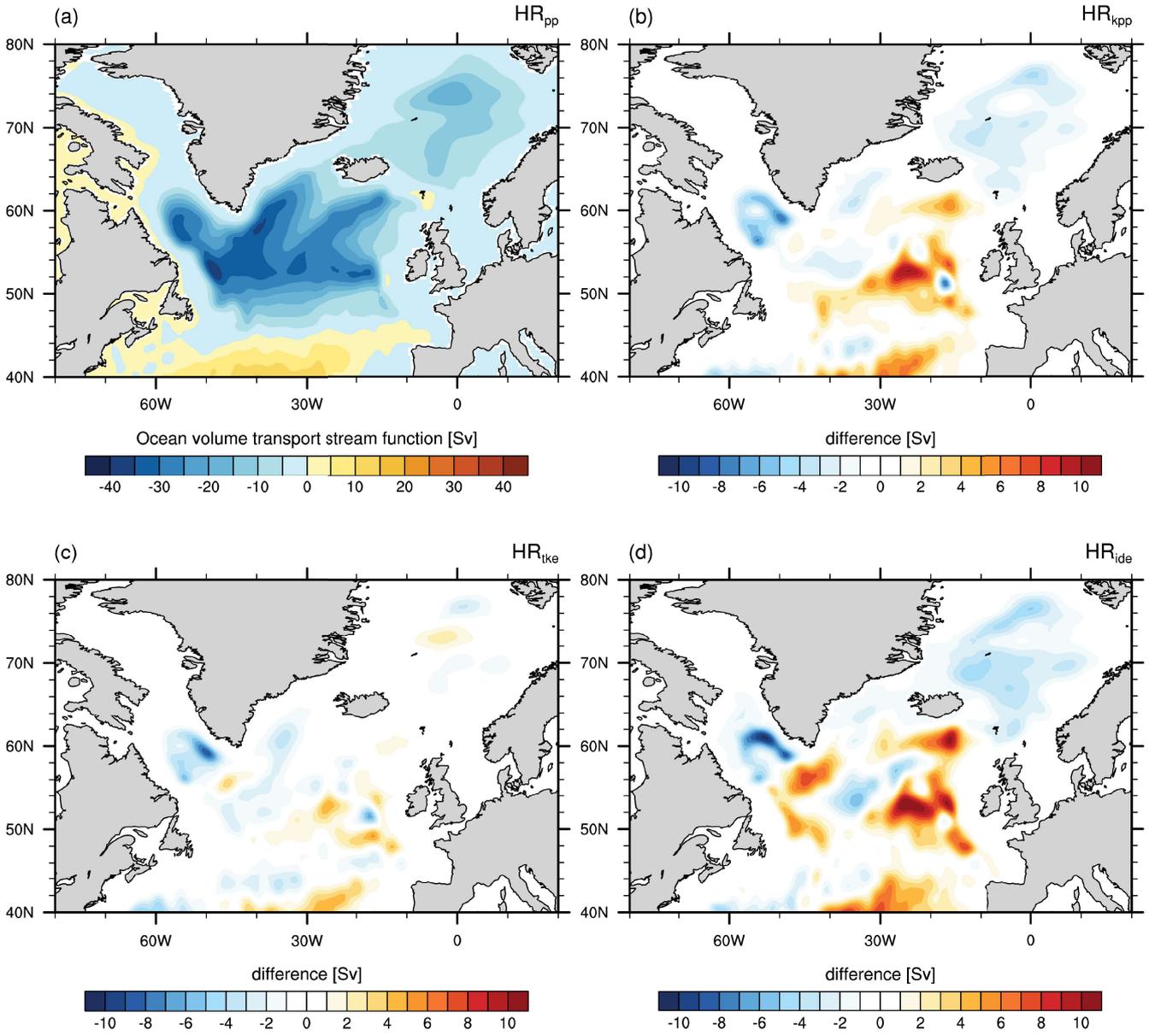
Figure 13. Time-averaged barotropic volume transport stream function (Sv) in the North Atlantic as simulated by MPI-ESM1.2 (a) HR_{pp}, and the differences "experiment - HR_{pp}" for (b) HR_{kpp}, (c) HR_{tke}, and (d) HR_{ide}.
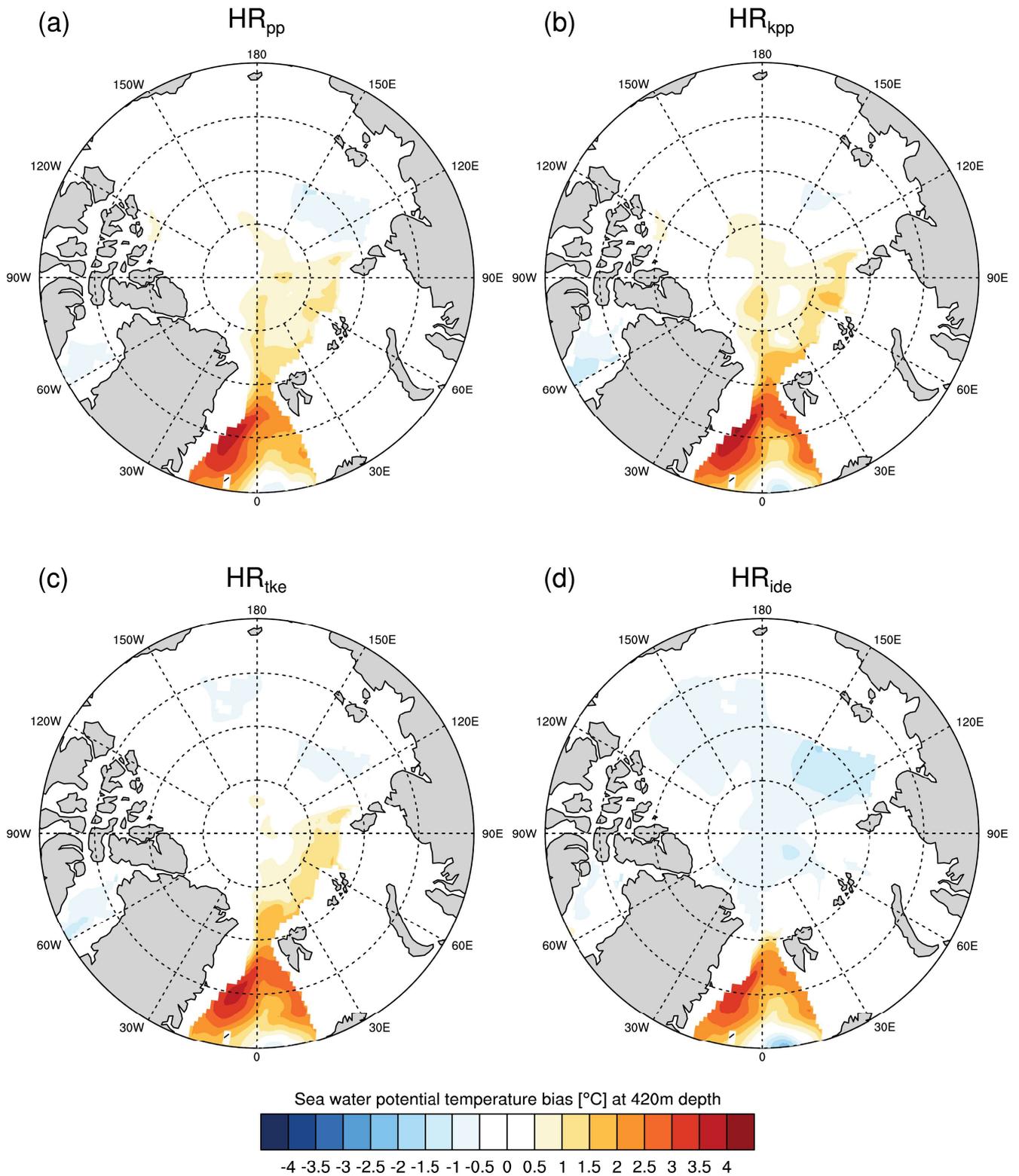
(a) HR$_{pp}$
(b) HR$_{kpp}$
(c) HR$_{tke}$
(d) HR$_{ide}$

Sea water potential temperature bias [°C] at 420m depth

-4 -3.5 -3 -2.5 -2 -1.5 -1 -0.5 0 0.5 1 1.5 2 2.5 3 3.5 4

Figure 14. [..^{273}]Time-averaged potential temperature bias of MPI-ESM1.2-HR minus EN4 ([..^{274}]1945-1955) at a depth of [..^{275}]420 m in [..^{276}]the Arctic Ocean and at Fram Strait for (a) HR$_{pp}$, (b) HR$_{kpp}$, (c) HR$_{tke}$, and (d) HR$_{ide}$.
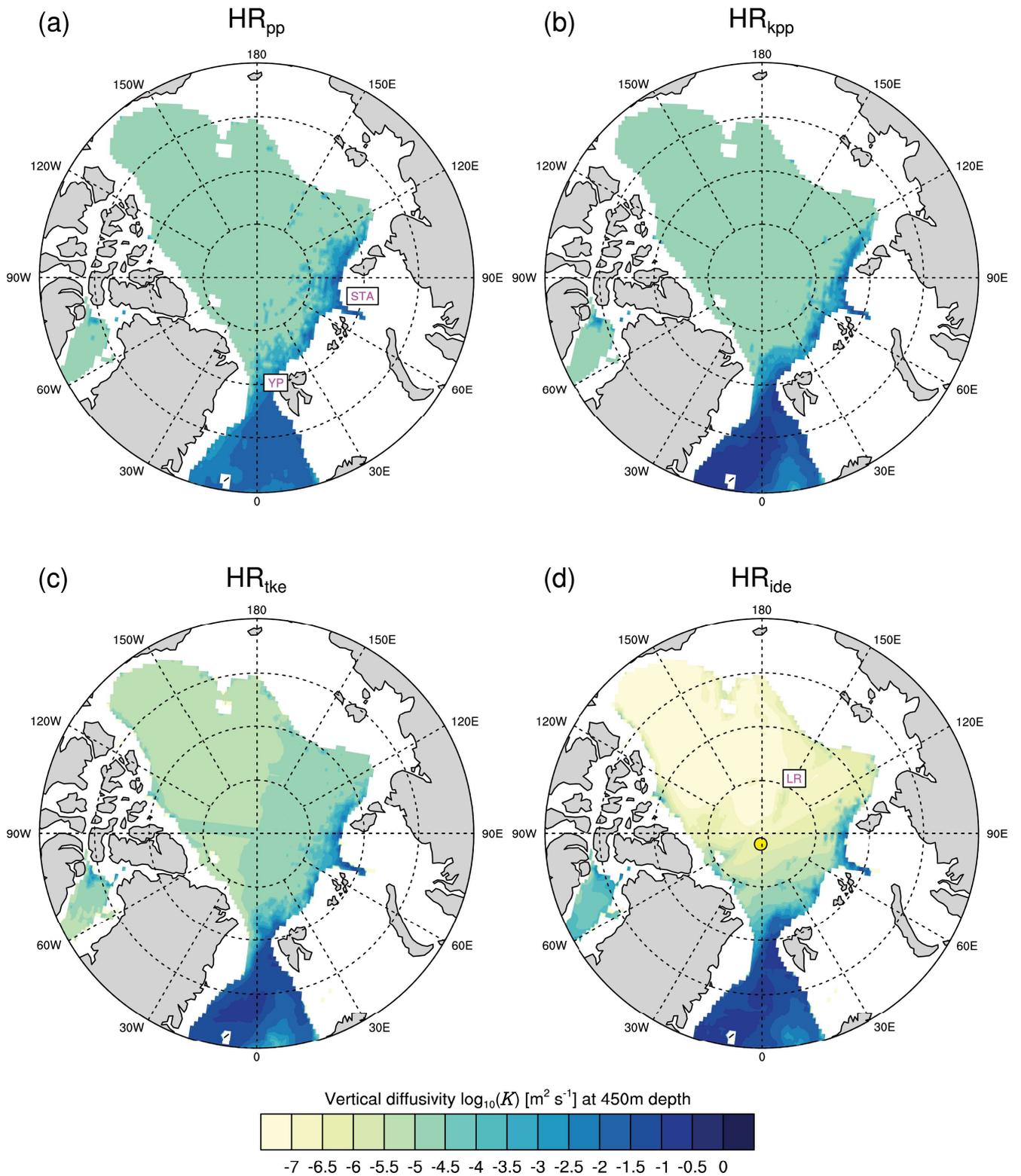
Figure 15. Time-averaged [..²⁷⁷]vertical diffusivity $\log_{10}(K)$ ([..²⁷**57**$\mathrm{m^2\,s^{-1}}$) [..²⁷⁹]at a [..²⁸⁰]depth of [..²⁸¹][..²⁸²]450 m in the [..²⁸³]Arctic Ocean and at Fram Strait simulated by MPI-ESM1.2 (a) $\mathrm{HR_{pp}}$, (b) $\mathrm{HR_{kpp}}$, (c) $\mathrm{HR_{tke}}$, and (d) $\mathrm{HR_{ide}}$. YP: Yermak Plateau, STA: St. Anna Trough, LR: Lomonosov Ridge. The yellow point marks the approximate position ($7°\mathrm{W}$, $89°\mathrm{N}$) of the Barneo ice camp in the
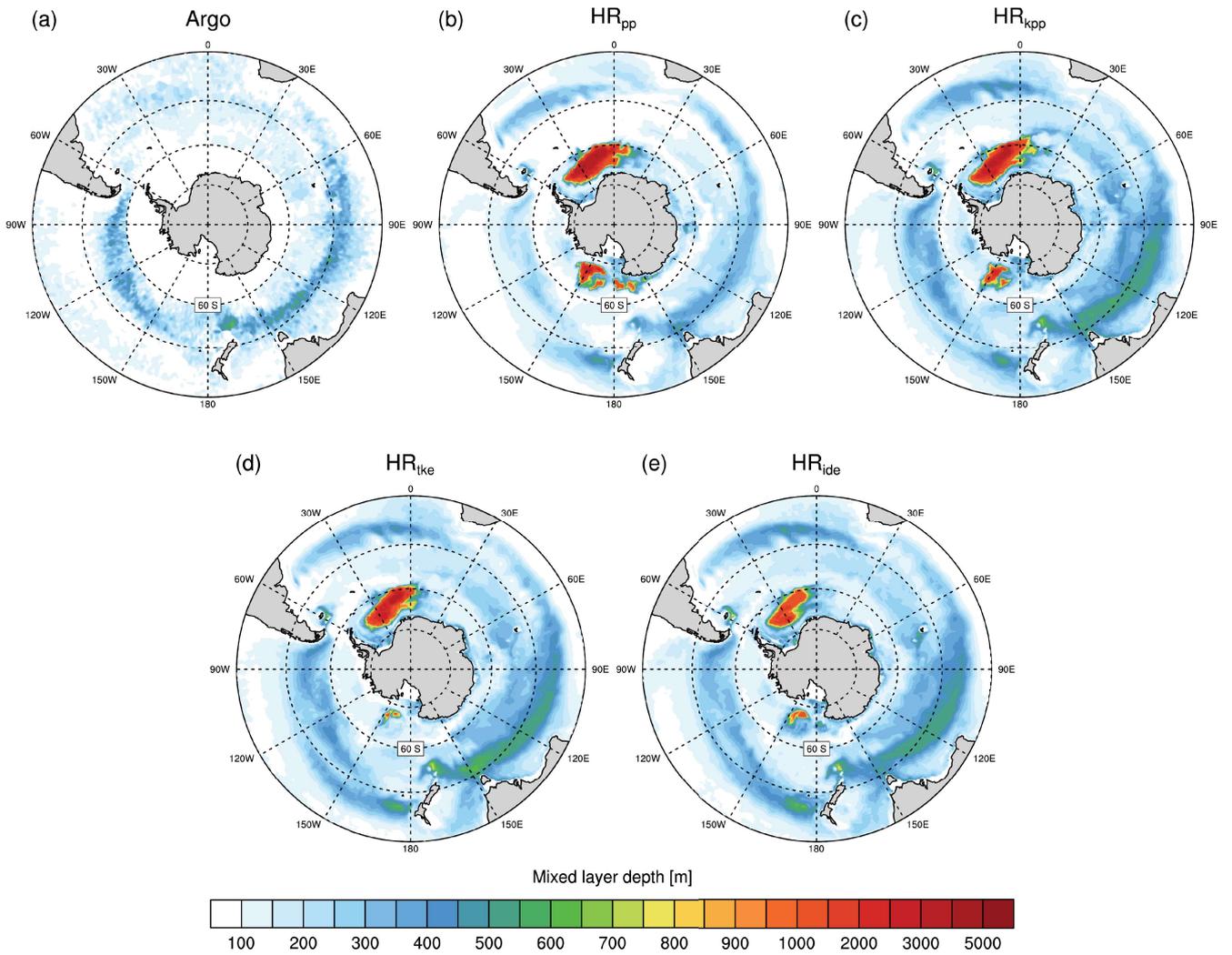
Figure 16. Time-averaged mixed layer depths (m) in September calculated (a) from $1° \times 1°$ Argo float data (Holte et al., 2017) (mean September from 2000 to 2018) by the density threshold method ($\sigma_t = 0.03 \, \mathrm{kg \, m^{-3}}$) and from MPI-ESM1.2 (b) HR_{pp}, (c) HR_{kpp}, (d) HR_{tke}, and (e) HR_{ide}. Note that there are no Argo data south of $60°S$.
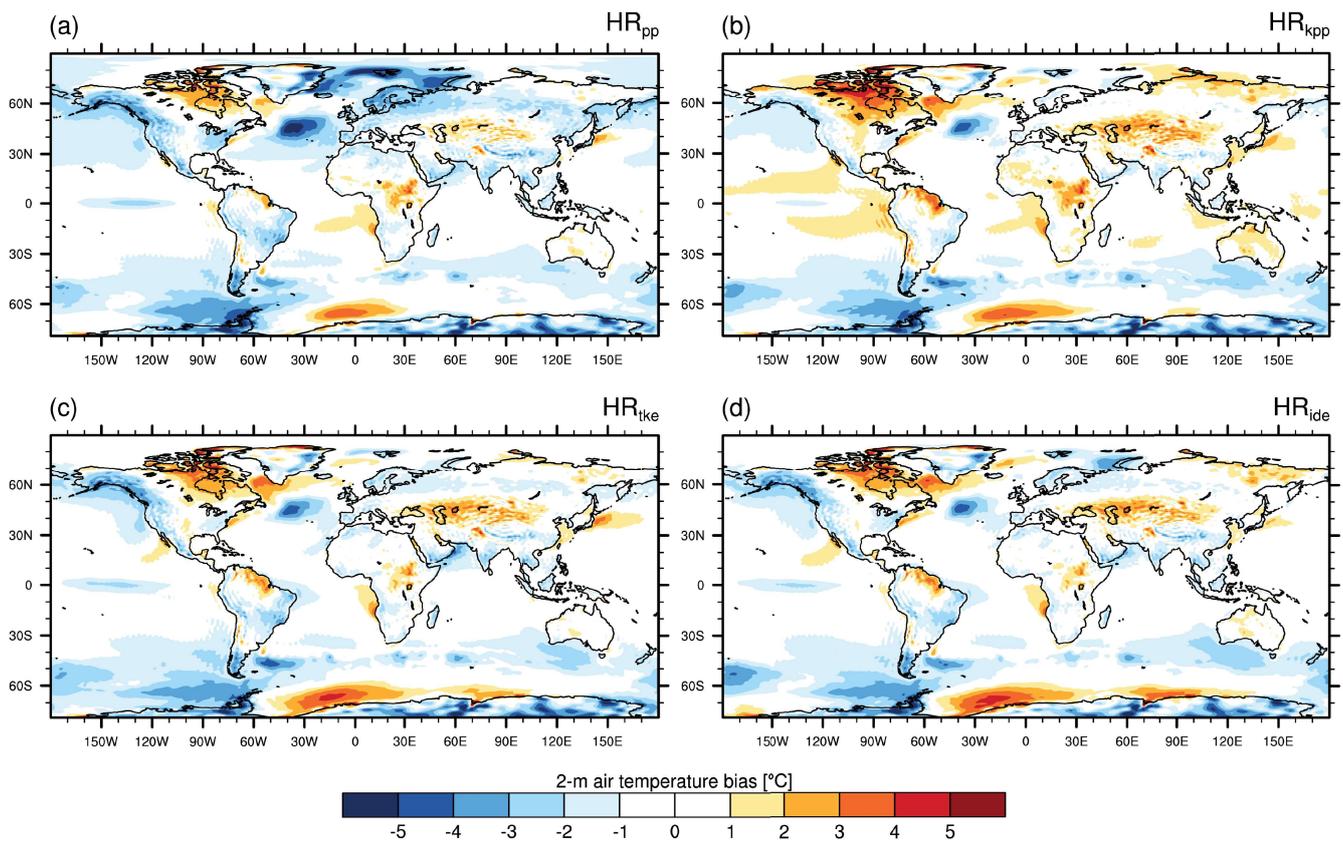
Figure 17. Time-averaged 2 m air temperature (SAT) bias (MPI-ESM1.2 minus EN4) for (a) HR$_{pp}$, (b) HR$_{kpp}$, (c) HR$_{tke}$, and (d) HR$_{ide}$.
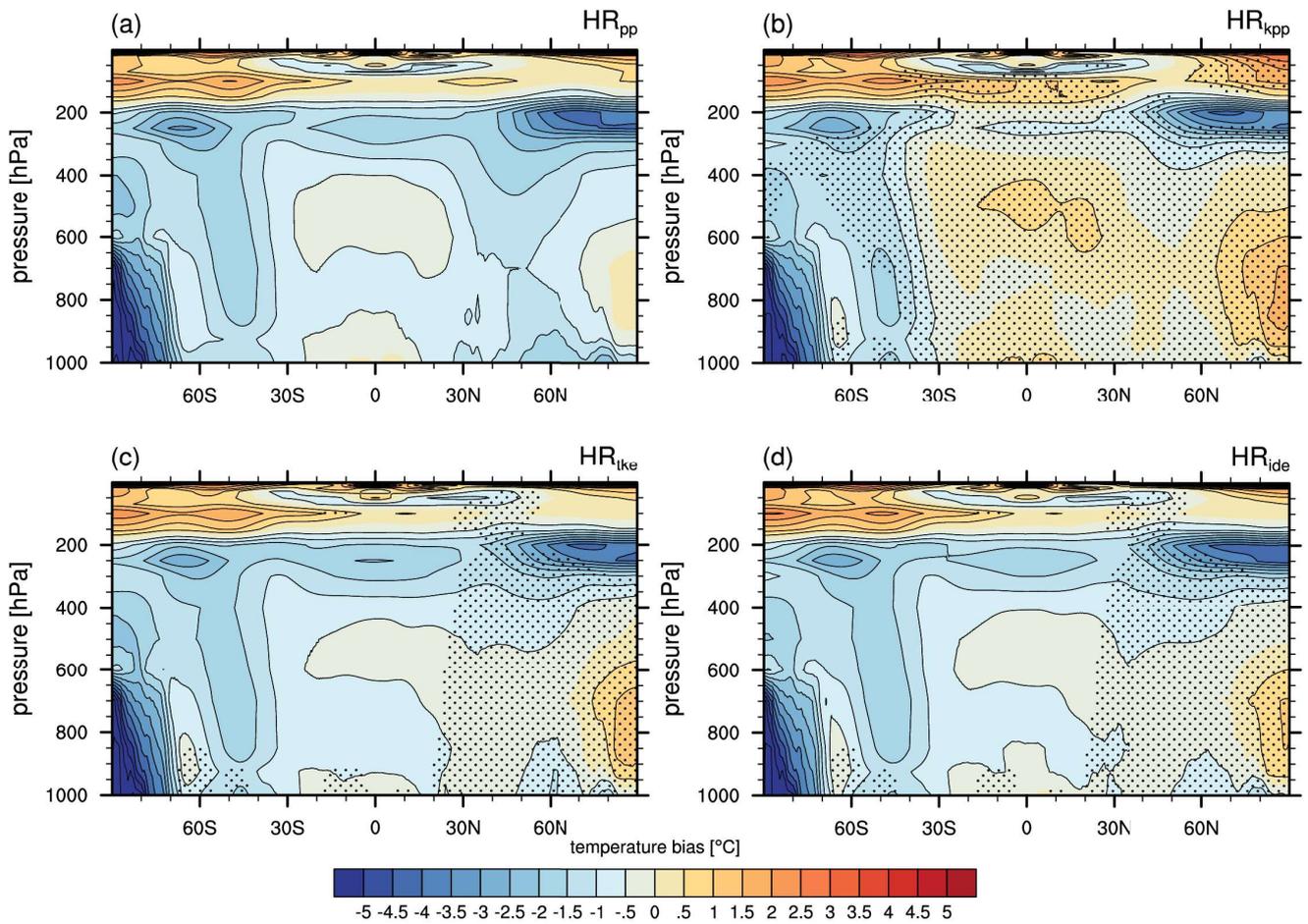
Figure 18. Time-averaged zonal air temperature bias (MPI-ESM1.2 minus EN4) for (a) HR$_{pp}$, (b) HR$_{kpp}$, (c) HR$_{tke}$, and (d) HR$_{ide}$. Stippling in (a-c) shows where the difference to HR$_{pp}$ is significant at $\alpha = 5\%$ based on adjusted p-values with the FDR method (Benjamini and Hochberg, 1995) using $\alpha_{FDR} = 5\%$ to account for multiplicity.

Figure 19. Time-averaged zonal wind speed bias (MPI-ESM1.2 minus EN4) for (a) HR_{pp}, (b) HR_{kpp}, (c) HR_{tke}, and (d) HR_{ide}. Stippling in (a-c) shows where the difference to HR_{pp} is significant at $\alpha = 5\%$ based on adjusted p-values with the FDR method (Benjamini and Hochberg, 1995) using $\alpha_{FDR} = 5\%$ to account for multiplicity.
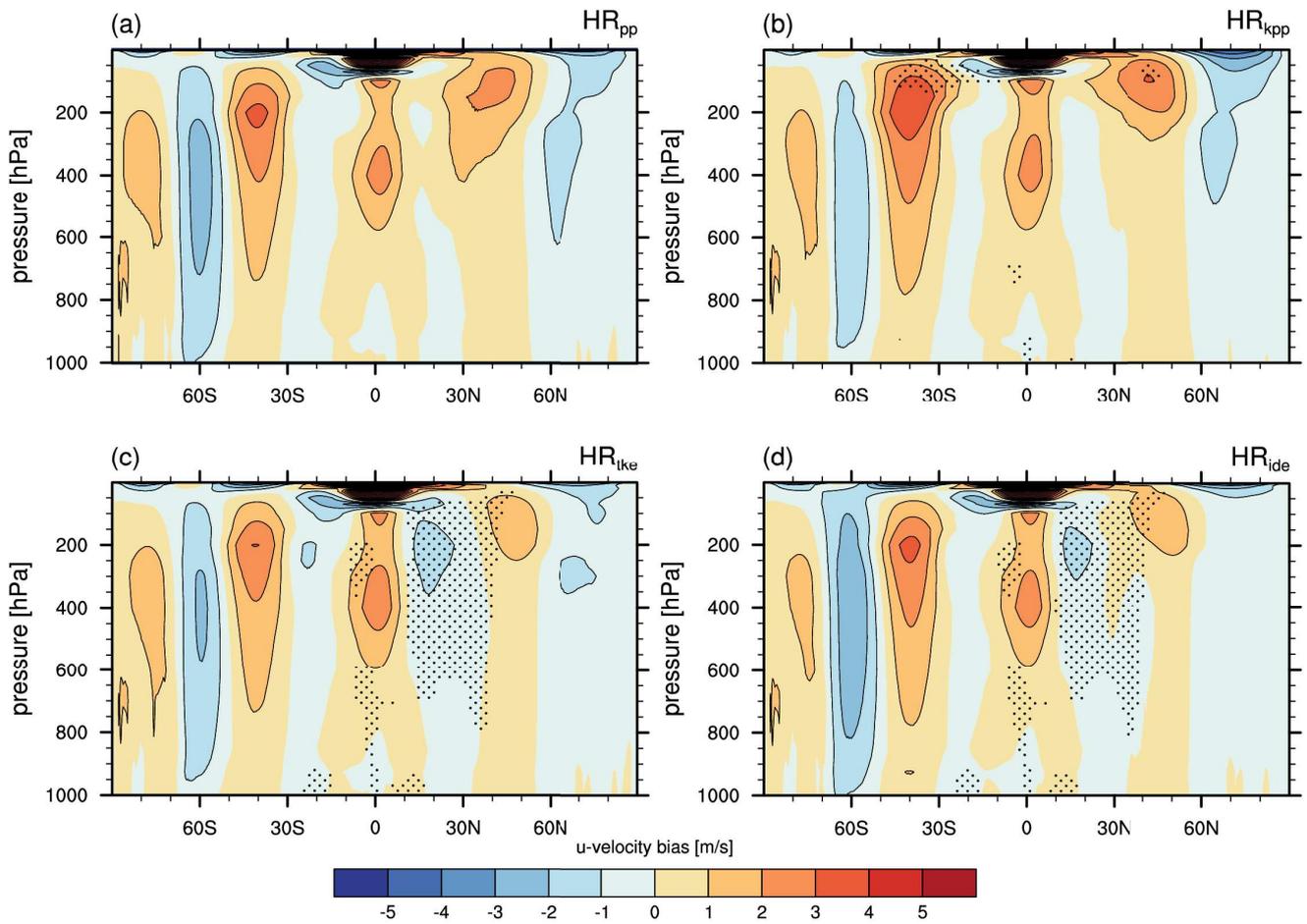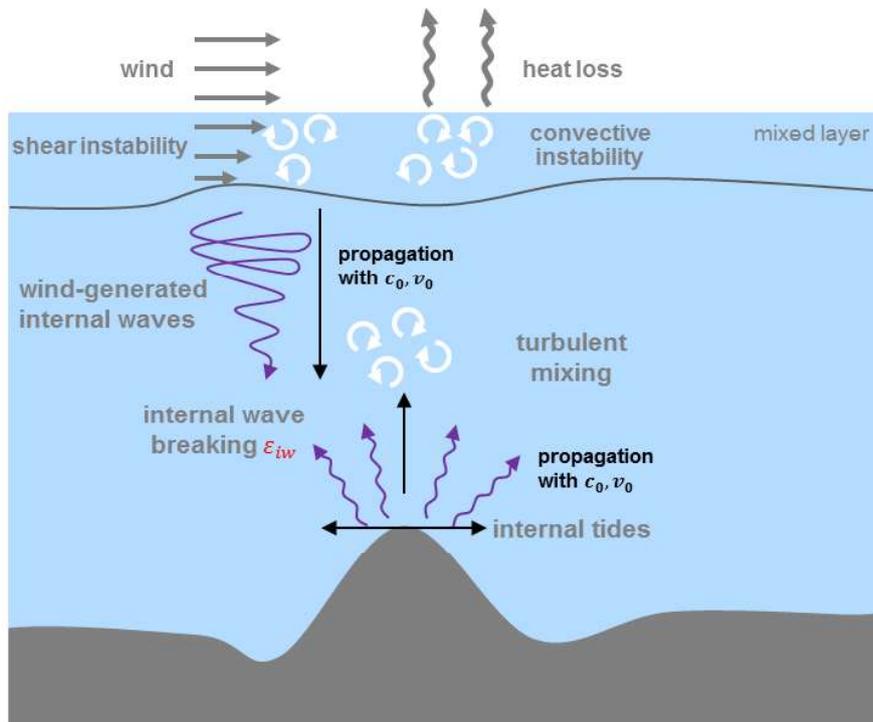
Figure A1. Schematic of the combined TKE+IDEMIX scheme used in HR$_{ide}$. Processes parameterised in TKE: away from strong currents, shear and buoyancy instability (convection) is largest near the surface (grey arrows), causing strong mixing in the mixed layer (white eddy symbols). Processes parameterized by IDEMIX: below the mixed layer, internal waves are either induced by fluctuating wind stress or by interactions of barotropic tides with orographic features (violet arrows). The internal waves are propagating into the interior ocean (black arrows), where they eventually break and dissipate (white eddy symbols).
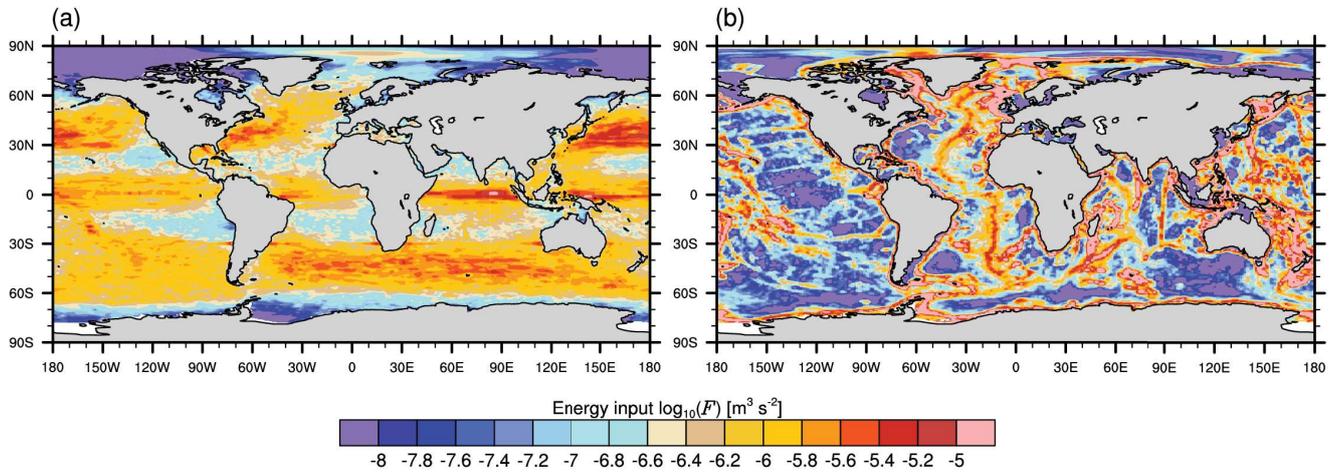
Energy input $\log_{10}(F)$ [m³ s⁻²]

Figure A2. Energy input $\log_{10}(F)$ $(\mathrm{m^3\,s^{-3}})$ at (a) the surface by near-inertial waves from Rimac et al. (2013) and (b) by tidal forcing at the ocean bottom from Jayne (2009).

Table A1. Resulting p-values from Welch's two-sided t-tests ($\alpha = 0.05$ and $n = 20$) for testing the differences in mean overflow volumes of Denmark Strait overflow (DSOW), in the Faroe-Shetland Channel (FSC), and in the Faroe Bank Channel (FBC).

	Experiment	$\mathrm{HR_{pp}}$	$\mathrm{HR_{kpp}}$	$\mathrm{HR_{tke}}$	$\mathrm{HR_{ide}}$
DSOW	$\mathrm{HR_{pp}}$	-	0.0*	0.0*	0.0*
	$\mathrm{HR_{kpp}}$	-	-	0.48	0.52
	$\mathrm{HR_{tke}}$	-	-	-	0.13
	$\mathrm{HR_{ide}}$	-	-	-	-
FSC	$\mathrm{HR_{pp}}$	-	0.23	0.0*	0.52
	$\mathrm{HR_{kpp}}$	-	-	0.02*	0.50
	$\mathrm{HR_{tke}}$	-	-	-	0.0*
	$\mathrm{HR_{ide}}$	-	-	-	-
FBC	$\mathrm{HR_{pp}}$	-	0.72	0.0*	0.0*
	$\mathrm{HR_{kpp}}$	-	-	0.0*	0.01*
	$\mathrm{HR_{tke}}$	-	-	-	0.0*
	$\mathrm{HR_{ide}}$	-	-	-	-

To achieve a power (1-β) of 80 % with $n = 20$ and $\alpha = 0.05$, the minimum effect size $d = |\mu_1 - \mu_2| / \sqrt{(sd_1^2 + sd_2^2)/2}$ is about 1.0. For instance, a pooled standard deviation of e.g. 0.1 Sv would correspond to a minimum mean difference of $|\mu_1 - \mu_2| = 0.1$ Sv.